



## Copyright Undertaking

This thesis is protected by copyright, with all rights reserved.

**By reading and using the thesis, the reader understands and agrees to the following terms:**

1. The reader will abide by the rules and legal ordinances governing copyright regarding the use of the thesis.
2. The reader will use the thesis for the purpose of research or private study only and not for distribution or further reproduction or any other purpose.
3. The reader agrees to indemnify and hold the University harmless from and against any loss, damage, cost, liability or expenses arising from copyright infringement or unauthorized usage.

### IMPORTANT

If you have reasons to believe that any materials in this thesis are deemed not suitable to be distributed in this form, or a copyright owner having difficulty with the material being included in our database, please contact [lbsys@polyu.edu.hk](mailto:lbsys@polyu.edu.hk) providing details. The Library will look into your claim and consider taking remedial action upon receipt of the written requests.

**HOMOJUNCTION AND HETEROSTRUCTURE  
ENGINEERING ON ZINC AND COPPER SULFIDES FOR  
ENHANCED PHOTOCATALYTIC HYDROGEN  
EVOLUTION FROM WATER**

**LIU WEI**

**PhD**

**The Hong Kong Polytechnic University**

**2019**

THE HONG KONG POLYTECHNIC UNIVERSITY  
DEPARTMENT OF APPLIED BIOLOGY & CHEMICAL  
TECHNOLOGY

**HOMOJUNCTION AND HETEROSTRUCTURE  
ENGINEERING ON ZINC AND COPPER SULFIDES FOR  
ENHANCED PHOTOCATALYTIC HYDROGEN  
EVOLUTION FROM WATER**

LIU WEI

A thesis submitted in  
partial fulfillment of the requirements for  
the degree of Doctor of Philosophy

December 2018

## **CERTIFICATE OF ORIGINALITY**

I hereby declare that this thesis is my own work and that, to the best of my knowledge, it reproduces no material previously published or written, nor material that has been accepted for the award of any other degree or diploma, except where due acknowledgement has been made in the text.

---

LIU Wei

December 2018

## Abstract

The development in semiconductor nanomaterials has brought many opportunities for efficient conversion of solar energy to clean and sustainable fuels for utilization and storage. Solution-based synthesis of earth-abundant metal sulfide nanomaterials is an ideal technique that offers the ease of preparation and the possibility of upscaling to meet industrial needs. This thesis focuses on the interface tuning of nanoscale zinc and copper sulfides as well as Au nanomaterials/copper sulfide, to give a fundamental understanding on the role of nanoscale interface in photocatalytic reaction.

Zinc sulfide (ZnS) nanocrystals with multiple parallel interfaces between wurtzite and sphalerite phases were prepared using a simple solvothermal method. The zinc atoms at these parallel interfaces have different electronic environments, creating abundant active sites on the surface. The ZnS nanocrystals were of good yield and high quality and exhibited a dramatic enhancement in H<sub>2</sub> gas evolution rate compared with that of normal ZnS. This rate was further increased by loading Pt nanoparticles on the ZnS surface. In a parallel electrocatalytic investigation, substantially lower overpotential for electrocatalytic hydrogen evolution was observed in the phase-junctions rich ZnS nanocrystals, probably attributed to the synergistic effect of easier proton adsorption and enhanced H<sub>2</sub> desorption on the active sites. Although the ZnS nanocrystals with multiple phase-junctions

exhibited drastically improved photocatalytic activity, the intrinsic wide bandgap limits the use of this material in visible-light driven photochemical reaction.

To further understand the impact of multiple phase-junctions, homo-interfaces were introduced to  $\text{Cu}_x\text{S}$  (where  $1 \leq x \leq 2$ ) as a *p*-type semiconductor photocatalyst. The crystal phases of  $\text{Cu}_x\text{S}$  can be tuned by varying the Cu/S stoichiometry using an ethylenediamine-mediated hydrothermal method, yielding  $\text{CuS}$ ,  $\text{Cu}_{1.75}\text{S}$ ,  $\text{Cu}_{1.8}\text{S}$  and  $\text{Cu}_2\text{S}$  nanocrystals. By fine-tuning the ratio of ethylenediamine, multiple phase-junctions were introduced to  $\text{Cu}_x\text{S}$  nanocrystals to modify the surface states, which promote the  $\text{H}_2$  gas evolution from water. The multiple interfaces give an optimal optical and photocatalytic performance when the  $\text{Cu}_x\text{S}$  nanocrystal is comprising of  $\text{Cu}_{1.75}\text{S}$  and  $\text{Cu}_{1.8}\text{S}$ , with *ca.* 230% enhancement in  $\text{H}_2$  gas evolution rate compared with single phase  $\text{Cu}_{1.8}\text{S}$ . An active surface arising from multiple interfaces within phase-junctions is believed to lower down the energy barrier of the  $\text{Cu}_x\text{S}$  nanocrystals, and improves the photocatalytic performance for  $\text{H}_2$  gas evolution.

To push up the photocatalytic performance of copper sulfide, plasmonic Au nanoparticles were embedded into hollow copper sulfide. In this study, different types of yolk-shell structures based on hollow copper sulfide encapsulating Au nanoparticles of various shapes were designed, prepared and characterized with the aims to enhance the light absorption, to improve the charge carrier separation

and transfer, and subsequently to enhance the photochemical activity. The results of photocatalytic hydrogen generation indicated that copper sulfide nanocages embedded with multi-spike Au nanoparticles performed better than pure copper sulfide nanoparticles or other Au-copper sulfide yolk/shell nanoparticles. This enhancement in catalytic activity highlights the size and shape effects of the Au nanomaterials, which have strong influence on the surface plasmonic resonance property. Multi-spike Au cores exhibit stronger plasmonic effect with increased pathways for exciton transport, which consequently generate an improved photocatalytic activity in the Au-copper sulfide nanoparticles.

To maximize the surface plasmon effect on photocatalysis, Au nanorod-copper sulfide nanocages with multiple interfacial contacts were prepared. This Au-copper sulfide hetero-nanostructure enhances the light-harvesting of copper sulfide over the visible region with hot electrons injected from Au. The supramolecular structured materials performed much better in photocatalytic hydrogen evolution than hollow copper sulfide nanocages alone and Au-copper sulfide mixture without interfacial contacts. This superior photocatalytic property could come from the plasmonic effect of the Au nanorod as the hot electron generator and the photoactive copper sulfide as the electron acceptor. This study introduced a unique hetero-structure of noble metal with semiconductor nanomaterial, and offers an alternative structural design of plasmonic metal-semiconductor nano-catalysts in photochemical reactions.

## **Acknowledgement**

I would like to express my sincere gratitude to everyone who was involved in my PhD study in The Hong Kong Polytechnic University.

Firstly, I am greatly grateful to the invaluable guidance, comments, and support from my chief supervisor Prof. Kwok-yin Wong and co-supervisor Dr. Lawrence Yoon Suk Lee. I am privileged to have the opportunity to work with them over the past three years.

Also, the work in this thesis would not have been possible without the assistance of many other people. Acknowledgement also goes to all the past and current members in Prof. Wong's and Dr. Lee's research groups, especially Dr. Enna Ha, Dr. Luyang Wang, Dr. Guangchao Zheng, Dr. Chui-Shan Tsang, Dr. Weiran Zheng, Dr. Lok-Yan So, Dr. Ho-Wing Man and Ms. Xiandi Zhang.

I would also like to thank Dr. Wai-Ming Kwok who provided much help in my work, and all the technical staff who ever helped me throughout my PhD study.

Finally, my deepest appreciation and sincere gratitude are delivered to my parents and friends, for their love and support.

## Table of Content

<b>Certificate of Originality.....</b>	<b>I</b>
<b>Abstract.....</b>	<b>II</b>
<b>Acknowledgement.....</b>	<b>V</b>
<b>Table of Content.....</b>	<b>VI</b>
<b>List of Abbreviations.....</b>	<b>XII</b>
<b>Chapter 1 Introduction.....</b>	<b>1</b>
1.1. Background.....	2
1.2. Basic principles of photocatalytic hydrogen evolution from water.....	4
1.3. Strategies to develop photocatalysts.....	11
1.3.1. Natural mineral photocatalysts.....	11
1.3.2. Solid solution photocatalysts.....	15
1.3.3. Dye-sensitized photocatalysts.....	16
1.4. Strategies for increasing photocatalytic efficiency.....	20
1.4.1. Semiconductor hybridization.....	20
1.4.2. Z-scheme system.....	25
1.4.3. Element doping.....	26
1.4.4. Cocatalyst loading.....	29
1.4.3.1. Metal cocatalysts.....	30
1.4.3.2. Semiconductor cocatalysts.....	34

1.4.5. Surface and interface engineering.....	37
1.4.6. Plasmonic effect.....	40
1.5. Aims and objectives.....	44
<b>Chapter 2 Experimental section and characterization techniques.....</b>	<b>47</b>
2.1. Materials.....	48
2.2. Synthesis.....	48
2.2.1. ZnS nanocrystal with parallel phase-junctions for photocatalytic water reduction to hydrogen.....	48
2.2.1.1. ZnS(ethylenediamine) <sub>0.5</sub> as precursor.....	48
2.2.1.2. ZnS nanocrystal with parallel phase-junctions.....	49
2.2.2. Cu <sub>x</sub> S nanocrystal with phase-junctions for photocatalytic water reduction to hydrogen.....	49
2.2.2.1. Copper sulfide-ethylenediamine as precursor.....	49
2.2.2.2. Cu <sub>x</sub> S nanocrystal with phase-junctions.....	50
2.2.3. Au nanomaterials embedded Cu <sub>1.8</sub> S hollow nanocage for photocatalytic water reduction to hydrogen.....	51
2.2.3.1. Au nanomaterials.....	51
2.2.3.2. Cu <sub>1.8</sub> S hollow nanocage.....	52
2.2.3.3. Au nanosphere embedded Cu <sub>1.8</sub> S hollow nanocage.....	53
2.2.3.4. Au nanorod embedded Cu <sub>1.8</sub> S hollow nanocage.....	54
2.2.3.5. Au nanostar embedded Cu <sub>1.8</sub> S hollow nanocage.....	54
2.2.4. Cu <sub>1.8</sub> S nanocage decorated Au nanorod for photocatalytic water reduction to hydrogen.....	55

2.2.4.1. Cu <sub>2</sub> O nanocube decorated Au nanorod.....	54
2.2.4.2. Cu <sub>1.8</sub> S nanocage decorated Au nanorod.....	55
2.3. Characterization techniques.....	55
2.3.1. Transmission electron microscopy.....	55
2.3.2. Powder X-ray diffraction.....	57
2.3.3. Ultraviolet-visible spectroscopy.....	59
2.3.4. Scanning electron microscopy.....	60
2.3.5. Raman scattering spectroscopy.....	61
2.3.6. X-ray photoelectron spectroscopy.....	62
2.3.7. Electrochemical polarization.....	64
<b>Chapter 3 ZnS nanoparticles with multiple parallel phase-junctions as highly active photocatalyst for water reduction to hydrogen.....</b>	<b>69</b>
3.1. Introduction.....	70
3.2. Results and discussion.....	71
3.2.1. Precursor ZnS(en) <sub>0.5</sub> .....	71
3.2.1.1. Powder X-ray diffraction.....	71
3.2.1.2. Structure analysis.....	73
3.2.2. ZnS nanocrystal.....	76
3.2.2.1. Transmission electron microscopy.....	76
3.2.2.2. Powder X-ray diffraction.....	81
3.2.2.3. Raman Spectroscopy.....	84
3.2.2.4. X-ray photoelectron spectroscopy.....	86
3.2.2.5. Ultraviolet-visible spectroscopy and energy-gap calculation.....	88

3.2.2.6. Photocatalytic hydrogen evolution.....	90
3.2.2.7. Electrochemical polarization curve.....	92
3.3. Concluding remarks.....	99
<b>Chapter 4 Ethylenediamine-modulated Synthesis of Copper Sulfides and Their Photocatalytic Activities for Water Reduction to Hydrogen.....</b>	<b>100</b>
4.1. Introduction .....	101
4.2. Results and discussion.....	104
4.2.1. Cu <sub>x</sub> S (x=1, 1.75, 1.80, 2) nanocrystals.....	104
4.2.1.1. Powder X-ray diffraction.....	104
4.2.1.2. Transmission electron microscopy.....	107
4.2.1.3. Energy dispersive X-ray spectroscopy.....	111
4.2.1.4. Ultraviolet–visible spectroscopy and energy-gap calculation...	114
4.2.1.5. Photocatalytic hydrogen evolution.....	116
4.2.2 Cu <sub>x</sub> S nanoparticles with multiple phase-junctions.....	118
4.2.2.1. Powder X-ray diffraction.....	118
4.2.2.2. Transmission electron microscopy.....	122
4.2.2.3. Energy dispersive X-ray spectroscopy.....	125
4.2.2.4. Ultraviolet–visible spectroscopy and energy-gap calculation...	128
4.2.2.5. Photocatalytic hydrogen evolution.....	131
4.3. Concluding remarks.....	134
<b>Chapter 5 Au Morphology-dependent Plasmon-enhanced Photocatalytic Water Reduction to Hydrogen by Au/Copper Sulfide Yolk-Shell Nanostructure.....</b>	<b>135</b>

5.1. Introduction.....	136
5.2. Results and discussion.....	139
5.2.1. Au nanomaterials.....	139
5.2.1.1. Transmission electron microscopy.....	139
5.2.1.2. UV-visible spectroscopy.....	141
5.2.2. Precursor Au/Cu <sub>2</sub> O nanostructure.....	143
5.2.2.1. X-ray diffraction.....	143
5.2.2.2. Transmission electron microscopy.....	147
5.2.2.3. Ultraviolet-visible spectroscopy.....	150
5.2.3. Au/Cu <sub>1.8</sub> S yolk-shell nanostructure.....	152
5.2.3.1. Powder X-ray diffraction.....	152
5.2.3.2. Transmission electron microscopy.....	154
5.2.3.3. Ultraviolet-visible spectroscopy.....	157
5.2.3.4. Photocatalytic hydrogen evolution.....	159
5.3. Concluding remarks.....	164
<b>Chapter 6 Au Nanorod as Antenna on Copper Sulfide Nanocage for Plasmon-enhanced Photocatalytic Water Reduction to Hydrogen.....</b>	<b>165</b>
6.1. Introduction.....	166
6.2. Results and discussion.....	168
6.2.1. X-ray diffraction.....	168
6.2.2. Transmission electron microscopy.....	172
6.2.3. Energy-dispersive X-ray spectroscopy.....	175
6.2.4. Ultraviolet-visible spectroscopy.....	179

6.2.5. Photocatalytic hydrogen evolution.....	182
6.3. Concluding remarks.....	188
<b>Chapter 7 Conclusions and Future Research Directions.....</b>	<b>189</b>
<b>References .....</b>	<b>195</b>

## List of Abbreviations

CB	Conduction band
DRS	Diffuse reflectance spectra
EDX	Energy-dispersive X-ray
EPR	Electron paramagnetic resonance
FFT	Fast Fourier Transformation
FRET	Förster resonance energy transfer
GC	Gas chromatography
HER	Hydrogen evolution reaction
HNG	Hollow nanocage
LSPR	Localized surface plasmon resonance
NHE	Normal hydrogen electrode
NC	Nanocube
NIR	Near infrared
NP	Nanosphere
NR	Nanorod
NS	Nanostar

PIRET	Plasmon-induced resonance energy transfer
SDS	Sodium dodecyl sulfate
SEM	Scanning electron microscopy
SPR	Surface plasmon resonance
SRR	Surface reverse reaction
STH	Solar-to-hydrogen
TCD	Thermal conductivity detector
TEM	Transmission electron microscopy
UV-vis	Ultraviolet-visible
VB	Valence band
XPS	X-ray photoelectron spectroscopy
XRD	X-ray diffraction

## **Chapter 1**

### **Introduction**

## 1.1 Background

Scientific work and studies on photocatalysis have grown since titanium dioxide ( $\text{TiO}_2$ ) was firstly reported on the photo-degradation of organic dyes in 1938.<sup>1</sup> It was discovered that the  $\text{TiO}_2$  surface produces active oxygen species by UV absorption, which is responsible for organic dyes photodegradation, while  $\text{TiO}_2$  remains unchanged after the reaction. In 1956, further investigation on the photochemical reaction of  $\text{TiO}_2$  was carried out by dispersing  $\text{TiO}_2$  powder in various organic solvents including alcohol and hydrocarbons.<sup>2</sup> It was found that the organic solvents were oxidized and  $\text{H}_2\text{O}_2$  was generated under ambient conditions. At that time, the photocatalytic activity of  $\text{TiO}_2$  as a typical photocatalyst did not attract much attention from people in either catalysis or photochemistry fields, neither in academic community nor industrial sector. It was only in the 1970s that the semiconductor photocatalyst first received wide attention when  $\text{H}_2$  release from  $\text{H}_2\text{O}$  using  $\text{TiO}_2$  photoelectrode was reported.<sup>3</sup> Since then, numerous works have been reported on improving the efficiency of hydrogen generation from water, so as to alleviate the pressing demands for clean and sustainable fuels across the world.

The last century has seen the increasing global development and population growth, further accelerating the world energy consumption. It is believed that the depletion of crude oil in the future will become a serious problem; crude oil prices would increase sharply, and not only economic but also social problems would rise. In order to tackle this shortage of conventional energy resources, several

promising approaches were suggested to utilize solar energy for solar-to-fuel application. One is using photovoltaic-electrolysis system with a heterojunction of GaInP/GaAs/GaInNAsSb triple-junctions, a high solar-to-hydrogen (STH) efficiency of 30% was achieved.<sup>4</sup> The advantage of the triple-junctions is that each component contributes to the photo-voltage required for water electrolysis and smaller bandgap materials can absorb enough solar energy in visible and near-infrared region of the solar spectrum. Another Z-scheme photoelectrochemical device for direct water-splitting was developed in 1984 on the basis of a Rh-modified InP electrode, achieved a STH efficiency of 13%.<sup>5</sup> A recent work using planar Pt/n-p Si photocathodes reached a striking photocurrent of *ca.* 30 mA cm<sup>-2</sup> and a STH efficiency of 10%.<sup>6</sup> Besides those photoelectrochemical devices, photocatalysts are widely studied because of their simple, scalable, and inexpensive advantages although the efficiency for water splitting is still low, leaving much room for improvement. One of the widely studied examples is Pt decorated TiO<sub>2</sub> that has been reported to be able to catalyze overall water splitting, although suffered from low STH efficiency.<sup>7</sup> However, the narrow light absorption range of TiO<sub>2</sub> and the scarcity of Pt hamper their use in photocatalysis. Over the past three decades, cost-effective and earth-abundant photocatalysts that can drive overall water splitting reaction using visible light have been much explored. Examples of extensively studied systems include CdS<sup>8</sup>, BiVO<sub>4</sub><sup>9</sup> and WO<sub>3</sub><sup>10</sup>. Recently, a powder photocatalyst NiO/NaTaO<sub>3</sub>:La was developed to efficiently drive water splitting reaction under solar irradiation.<sup>11</sup> This work firstly showed that powder photocatalysts can

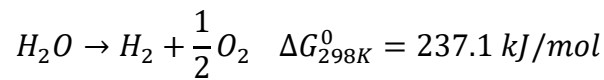
enable highly efficient solar water splitting, with an impressive quantum yield of 56% at 270 nm. Following this work, visible-light active semiconductor oxynitrides such as  $\text{Rh}_{2-x}\text{Cr}_x\text{O}_3/\text{GaN}:\text{ZnO}^{12}$  and Z-scheme systems such as  $\text{Ru}/\text{SrTiO}_3:\text{Rh}-\text{BiVO}_4^{13}$  and  $\text{CdS}/\text{carbon dot}/\text{BiVO}_4^{14}$  have also been reported to possess active photocatalytic properties for water splitting. Besides metal oxides and nitrides, metal sulfide photocatalysts composed of multiple components such as  $\text{AgInS}_2-\text{CuInS}_2-\text{ZnS}^{15}$ ,  $\text{Cu}_2\text{ZnSnS}_4-\text{MoS}_2/\text{reduced graphene oxides}^{16}$ , were proved highly active for solar  $\text{H}_2$  gas evolution from water. However, STH efficiency of most powder photocatalysts is far below 10%, which is the threshold for commercial application.<sup>17, 18</sup>

## **1.2 Basic principles of photocatalytic hydrogen evolution from water**

Photocatalysis in a semiconductor originates from the electron excitation across the band gap from valence band (VB) to conduction band (CB). If an external photon has an energy that exceeds the energy gap between VB maximum and CB minimum in a semiconductor, an electron in the VB is excited onto the CB, and meanwhile, a hole is created in the VB. The recombination of exciton (electron-hole pairs) results in the loss of energy by heat, produces no chemical effect. However, if the electron-hole pairs separate and transfer to the semiconductor surface before recombination, they can be used to drive various redox reactions of reactant species such as  $\text{H}^+/\text{H}_3\text{O}^+$ ,  $\text{CO}_2$ , and metallic ions on the semiconductor surface. These redox reactions are the basic pathways of photocatalytic reactions such as hydrogen evolution,  $\text{CO}_2$  conversion, and pollutants degradation. Figure

1.1 illustrates the photocatalytic H<sub>2</sub> evolution reaction (HER), showing the steps after the semiconductor being irradiated: (1) photogeneration of electron-hole pairs, (2) separation of electron-hole pairs, (3) recombination of charge carriers, (4) transfer and transport of electrons/holes to water or other reactants.

Notably, the steps from (1), (2) and (4) are involved in the molecular H<sub>2</sub> evolution from the semiconductor photocatalyst. The overall reaction for hydrogen evolution from water is:



The input energy to drive water splitting reaction should satisfy a minimum thermodynamic potential of 1.23 volts, as illustrated in Figure 1.2. Without external bias, the CB minimum of semiconductor should be more negative than the H<sup>+</sup>/H<sub>2</sub> reduction potential and the VB maximum should be more positive than O<sub>2</sub>/H<sub>2</sub>O oxidation potential due to thermodynamic and kinetic losses. The H<sup>+</sup>/H<sub>3</sub>O<sup>+</sup> from water reacts with photogenerated electrons to generate H<sub>2</sub>, whereas the holes can be consumed by the oxidation reaction with external electron donor (D).

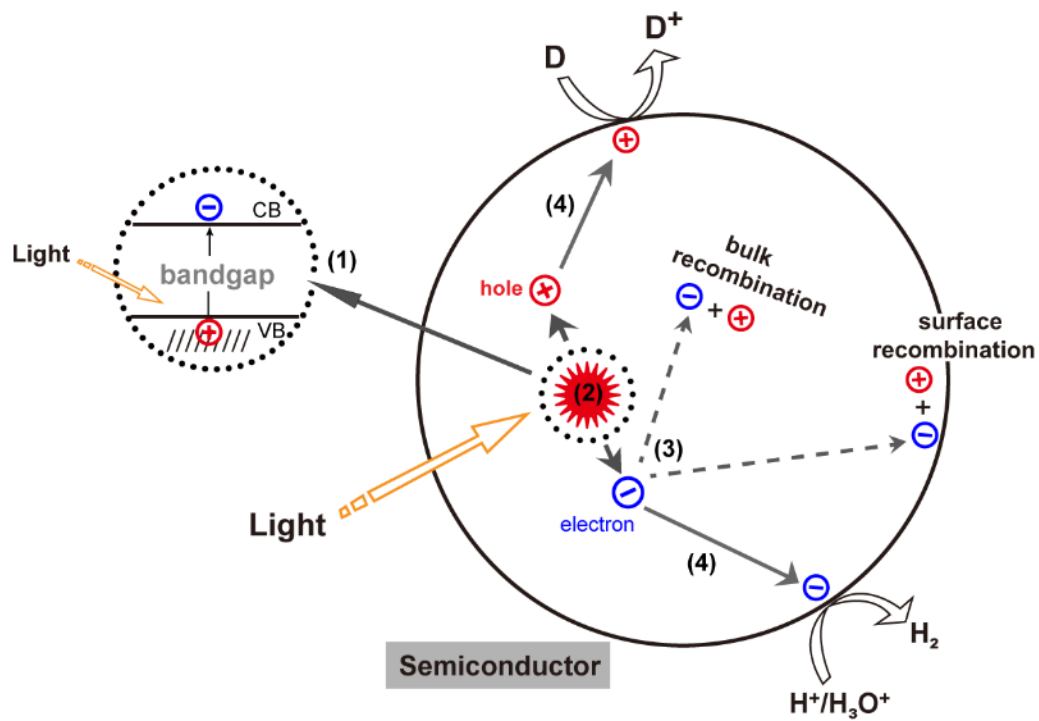


**Figure 1.1** Steps in irradiated semiconductor for photocatalytic hydrogen evolution reaction. D and D<sup>+</sup> refer to external electron donor and oxidized electron donor, respectively.

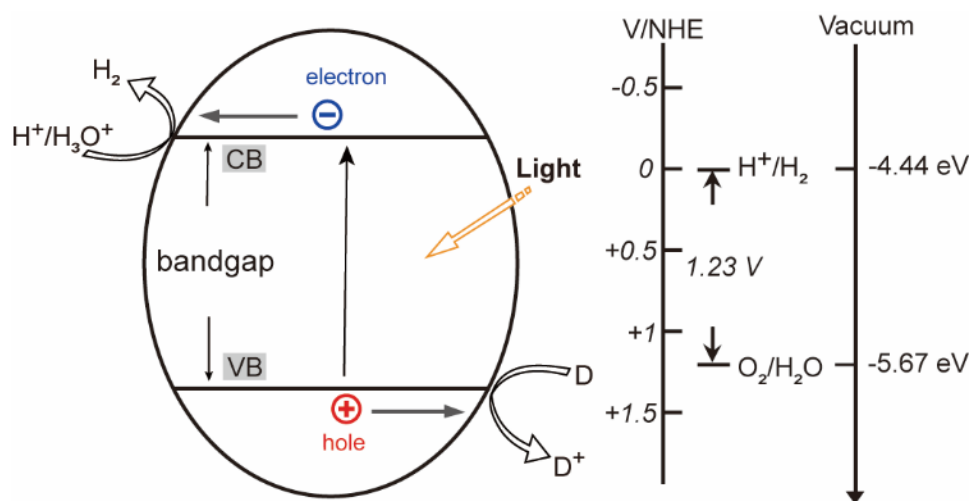


**Figure 1.2** Fundamental principle of semiconductor-based photocatalyst for hydrogen evolution from water. D and D<sup>+</sup> refer to electron donor and oxidized electron donor, respectively.

The efficiency of solar energy conversion is largely determined by the amount of excited charge carriers on the surface of a semiconductor in photocatalytic half reaction. Thus, any process that decreases the number of excited electrons and holes should be suppressed for the higher efficiency of the redox reactions at semiconductor surface, while all processes that facilitate the generation of electron-hole pairs should be promoted. Several factors in promoting charge-generation need to be considered for materials design and selection for photocatalysis. Firstly, the ideal bandgap of photocatalyst for water splitting should be 1.9-2.3 eV<sup>19</sup> with suitable band positions to maximize photons harvesting. Secondly, light reflection/scattering effect on photocatalysts should be minimized to facilitate light absorption. Thirdly, semiconductor photocatalysts should be capable of efficiently generating excitons when interacting with external photons, and meantime, with the minimum energy loss by electron-hole recombination. An efficient charge separation, faster and thus greater than the charge recombination, is highly desirable for a photocatalyst.

Electron-hole pair recombination leads to fewer excitons by generating photons. Both surface and bulk recombination are usually called deactivation process, which is detrimental to photocatalytic reaction. A high rate of electron-hole separation and charge transport, as well as a low rate of electron-hole recombination at semiconductor bulk or surface, are key factors in promoting reduction reactions. Creating a built-in electrical field and using semiconductor

materials of high photoconductivity are proven to improve the charge separation and transport for reaction in semiconductor photocatalyst system.

Surface reverse reaction (SRR) is generally linked with the photochemical reaction of evolving  $H_2$  and  $O_2$  molecules on the photocatalyst surface. SRR can lead to water regeneration by the reaction of  $O_2$  with photogenerated electrons from the photocatalyst surface and the cocatalyst, as shown in Figure 1.3. SRR can weaken the photocatalyst activity by consuming the evolved  $H_2$  from the photocatalytic process, thus, the water splitting reaction does not proceed efficiently. To date, there are two methods developed to minimize the SRR. One is using sacrificial agents in the reaction system and the other is to introduce separated photoactive sites for  $H_2$  and  $O_2$  evolution on the semiconductor surface. The sacrificial agents as an electron/hole scavenger in the solution can offer an additional driving force for the redox reaction to minimize the  $H_2O$  formation by SRR. Besides, surface separation of photogenerated charge carriers is resulted from separated  $H_2$  and  $O_2$  evolution reaction sites for photocatalysis, which is proven to be greatly influenced by the chemical surface states of the photocatalyst.

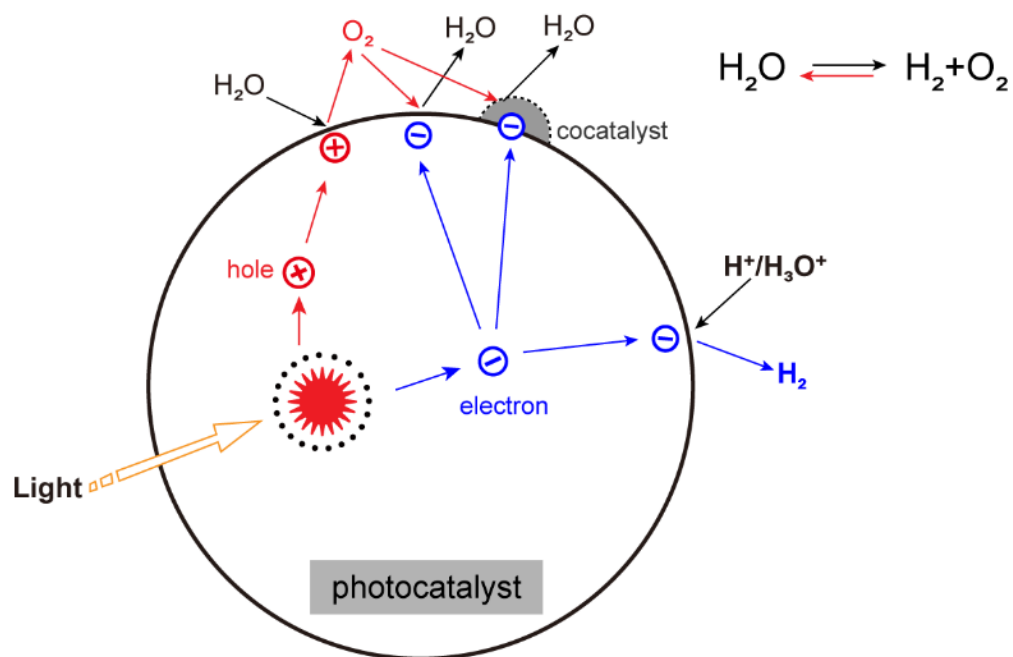


**Figure 1.3** Surface reverse reaction of evolving  $\text{H}_2$  and  $\text{O}_2$  molecules, and formation of  $\text{H}_2\text{O}$  on the semiconductor photocatalyst surface.

In summary, a suitable band gap for efficient light absorption and effective charge separation of photogenerated electrons and holes are critical for improving semiconductor photocatalytic activity. With increasing demand for high performance solar-driven semiconductor photocatalysts, cost-effective, environment-friendly photocatalysts composed of earth-abundant elements are much desirable for economically viable solar energy conversion systems.

### **1.3 Strategies for developing photocatalysts**

#### 1.3.1 Natural mineral photocatalysts

Semiconductor minerals are a widely distributed category of minerals in nature. There are hundreds of semiconductor minerals on Earth, most of which are common minerals close to the Earth's surface, such as oxides [zincite (ZnO), rutile (TiO<sub>2</sub>)] and sulfides [sphalerite (ZnS), chalcocite (Cu<sub>2</sub>S), covellite (CuS)]. The energy band structure, crystal defects, and other physical properties of natural semiconductor minerals were systematically studied in 1975 for the first time.<sup>20, 21</sup> The energy positions of CB and VB edges for about fifty semiconducting metal oxide and metal sulfide minerals were investigated. The bandgaps of some abundant natural semiconductor minerals and their corresponding maximal wavelength for generating photo-excitons are listed in Table 1.1. Impurities and defects, such as doping elements, interstitial ions or atoms, and lattice vacancies, can alter electronic structures of semiconductor minerals. The energy gap of a natural semiconductor mineral is usually narrower

than its synthetic counterpart, which makes the natural semiconductors to work as photocatalysts to drive chemical reactions.

**Table 1.1** Energy gap of semiconducting minerals and the corresponding maximal wavelength for generating photoexcitons.<sup>22</sup>

Metal oxides				Metal sulfides			
Minerals	Formula	$E_g/eV$	$\lambda/nm$	Minerals	Formula	$E_g/eV$	$\lambda/nm$
Romarchite	SnO	4.2	296	Sphalerite	ZnS	3.6	345
Manganosite	MnO	3.6	345	Alabandite	MnS	3.0	413
Bunsenite	NiO	3.5	355	Berndtite	SnS <sub>2</sub>	2.1	592
Cassiterite	SnO <sub>2</sub>	3.5	355	Stibnite	Sb <sub>2</sub> S <sub>3</sub>	1.7	723
Zincite	ZnO	3.2	388	Tungstenite	WS <sub>2</sub>	1.35	918
Anatase	TiO <sub>2</sub>	3.2	388	Molybdenite	MoS <sub>2</sub>	1.17	1062
Senarmontite	Sb <sub>2</sub> O <sub>3</sub>	3.0	413	Chalcocite	Cu <sub>2</sub> S	1.1	1130
Bismite	Bi <sub>2</sub> O <sub>3</sub>	2.8	443	Herzenbergite	SnS	1.01	1231
Wuestite	FeO	2.4	518	Pyrite	FeS <sub>2</sub>	0.95	1305
Cuprite	Cu <sub>2</sub> O	2.2	565	Argentite	Ag <sub>2</sub> S	0.92	1351
Tenorite	CuO	1.7	731	Hauerite	MnS <sub>2</sub>	0.50	2486
Pyrolusite	MnO <sub>2</sub>	0.25	4972	Polydymite	NiS	0.40	3108
Magnetite	Fe <sub>3</sub> O <sub>4</sub>	0.1	12431	Pyrrhotite	FeS	0.1	12431

Among natural metal oxides, TiO<sub>2</sub> is one of the most widely used catalysts for solar-to-fuel reactions owing to its relatively low-cost, nontoxicity and remarkable photocatalytic activity. It is known that TiO<sub>2</sub> has three different crystal structures: rutile (R), anatase (A), and brookite (B). Among them, anatase, rutile, and the mixture of anatase and rutile phase (e.g., Degussa P25) TiO<sub>2</sub> have been extensively used for photocatalytic applications such as hydrogen

generation<sup>23</sup> and CO<sub>2</sub> conversion.<sup>24</sup> The photocatalytic properties of A- and R-TiO<sub>2</sub> has attracted intense research interests for many years. R-TiO<sub>2</sub> is the most widely used and favored over A-TiO<sub>2</sub> for its chemical stability. A general agreement has been made on the bandgaps of R- and A-TiO<sub>2</sub> to be at *ca.* 3.0 and 3.2 eV, respectively.<sup>25</sup> Therefore, R-TiO<sub>2</sub> can absorb sunlight at longer wavelength in solar spectrum than A-TiO<sub>2</sub>. However, A-TiO<sub>2</sub> was proved to be more active for photocatalysis because of its active surface chemistry.<sup>26</sup> In 1996, the band position of TiO<sub>2</sub> was first measured by electrochemical impedance spectroscopy. The flat band potential of A-TiO<sub>2</sub> was measured to be 0.2 eV above (or more negative) that of rutile TiO<sub>2</sub>,<sup>27</sup> which may be responsible for the better photocatalytic activity in hydrogen evolution reaction. The photocatalytic H<sub>2</sub> generation performance of TiO<sub>2</sub> is impressively efficient under UV irradiation, with a high quantum yield reaching 50%.<sup>28</sup> However, only the UV light (*ca.* 4% of the total solar energy) in solar spectrum can be utilized by TiO<sub>2</sub>, due to the intrinsically wide band gap.

Aside from TiO<sub>2</sub>, metal sulfides present another important class of semiconductor material for photocatalytic applications. The interest in these materials comes from their wide light response range, non-toxicity, natural abundance, and cost-effectiveness. Among them, a simple binary metal sulfide, the copper sulfides family, has been widely investigated and developed for photocatalytic applications. Also, some ternary and quaternary copper sulfide derivatives by introducing transition metal elements as well as formation of

heterojunctions with other metal sulfides or oxides are reported to perform photocatalytic HER. Generally,  $\text{Cu}_{2-x}\text{S}$  ( $0 \leq x \leq 1$ ) is a simple class of *p*-type semiconductors arising from Cu vacancies in the lattice. For single crystal unit, Cu occupies interstitial sites of the lattice and the deviation from stoichiometric Cu to S leads to the formation of different crystal structures. Various precursors (metal and sulfide sources) and crystal structural modifications by heteroatom introduction may enable the tunability in the composition and crystal structure of  $\text{Cu}_{2-x}\text{S}$ . Typically, binary copper sulfides such as  $\text{Cu}_7\text{S}_4$  ( $\text{Cu}_{1.75}\text{S}$ ),<sup>29</sup> and  $\text{Cu}_9\text{S}_5$  (or  $\text{Cu}_{1.8}\text{S}$ )<sup>30</sup> have great photon harvesting and active surfaces, which are related to their photoactivities for HER. Besides binary copper sulfides, ternary, and quaternary sulfides for photocatalytic applications have also received wide interests. For example,  $\text{CuInS}_2$  and  $\text{CuIn}_5\text{S}_8$  were reported to show superior visible-light photocatalytic HER activities, compared with other derivatives of off-stoichiometric ratios.<sup>31</sup> With a higher CB level,  $\text{CuGa}_3\text{S}_5$  showed a good HER performance and altered photoactivity using different co-catalysts such as Pt, Ir etc.<sup>32</sup> In quaternary sulfides, Cu-Ga-In-S are well studied. The impact of Ga/In ratio was also investigated on the photoactivity of  $\text{CuGa}_2\text{In}_3\text{S}_8$ , and the Ga/In ratio of 0.67 showed a higher activity among the others.<sup>33</sup> The introduction of Ga to replace a part of In led to band gap adjustment by upshifting the CB position thus rendering a stronger driving force for catalyzing the water reduction reaction. Moreover, the class of  $\text{Cu}_2\text{XSnS}_4$  (X= Zn, Fe, Mn, and Co) semiconductor materials have been discovered to have a better photon harvesting capability due

to the narrow bandgaps (*ca.* 1.5-1.8 eV) and reported to be active in evolving H<sub>2</sub> gas from water.<sup>34, 35</sup>

### 1.3.2 Solid solution photocatalysts

Semiconductor solid solution is a single-phase alloy comprising different semiconductors with the matching structure and varied electronic properties. Solid solution semiconductor for photocatalysis is usually made of wide and narrow band gap semiconductor, providing a platform for tuning the electronic structure of semiconductor. Both the band position and band gap can be modulated by varying the composition ratios of the narrow and wide bandgap semiconductors in the solid solution. Typically, Cd<sub>x</sub>Zn<sub>1-x</sub>S (0.1 < x < 1) solid solutions, formed by combining the wide bandgap semiconductor ZnS (3.3-3.7 eV)<sup>36, 37</sup> and the narrow bandgap semiconductor CdS (2.2-2.6 eV),<sup>38</sup> have received much attention on the visible-light-driven catalytic applications. The Cd<sub>x</sub>Zn<sub>1-x</sub>S solid solution shows tunable bandgaps (2.4-3.7 eV)<sup>39</sup> and impressive visible-light photocatalytic activity for H<sub>2</sub> generation from water using polysulfides as sacrificial agent.<sup>40</sup> One example reported that a Cd<sub>1-x</sub>Zn<sub>x</sub>S solid solution semiconductor synthesized by thermal sulfidation of the mixed oxide precursors exhibited a superior photochemical activity to the conventional counterparts.<sup>41</sup> It was shown that by adjusting the ratio of Cd and Zn in the Cd<sub>1-x</sub>Zn<sub>x</sub>S (Cd<sub>0.8</sub>Zn<sub>0.2</sub>S), a high quantum yield of 10.23% (420 nm) for cocatalyst-free H<sub>2</sub> generation from water was realized.

The development of novel photocatalytic system based on ZnS and MInS<sub>2</sub> (M = Cu, Ag) solid solutions allows the energy structures to be adjusted by the composition alterations. The CB and VB edges ZnS–AgInS<sub>2</sub> [(AgIn)<sub>0.11</sub>Zn<sub>0.78</sub>S] shifted monotonically with a changing ratio of AgInS<sub>2</sub> to ZnS in the solid solution, which showed high visible-light photocatalytic activities for H<sub>2</sub> evolution.<sup>42</sup> Two platinized solid solutions (AgIn)<sub>0.11</sub>Zn<sub>0.78</sub>S (E<sub>g</sub> = 2.33 eV) and (CuIn)<sub>0.09</sub>Zn<sub>1.82</sub>S<sub>2</sub> (E<sub>g</sub> = 2.35 eV) have reached the apparent quantum yields of 20% and 12.5% at 420 nm, respectively.<sup>42, 43</sup> Moreover, a quaternary solid solution ZnS–CuInS<sub>2</sub>–AgInS<sub>2</sub> (Cu<sub>0.25</sub>Ag<sub>0.25</sub>In<sub>0.5</sub>ZnS<sub>2</sub>) was developed and showed a wider light-response range and enhancement in photocatalytic H<sub>2</sub> gas evolution than the ZnS–MInS<sub>2</sub> (M = Cu or Ag) solid solutions. It is believed that a narrower band gap (E<sub>g</sub> = 1.77 eV) formed by the hybridization of the Cu 3d and Ag 4d orbitals in the VB of the quaternary solid solution contributed to a stronger visible light absorption.<sup>15, 44</sup>

### 1.3.3 Dye-sensitized photocatalysts

Dye sensitization presents another powerful approach to enable solar energy conversion applications such as visible-light photochemical and/or photocatalytic reactions on wide band gap semiconductors.<sup>45</sup> The first work on a dye-sensitized semiconductor (trimeric ruthenium bipyridine complex-TiO<sub>2</sub>) for solar energy conversion was reported in 1991 that a power-conversion efficiency of 7.9% was achieved.<sup>46</sup> Since then, great efforts were made to develop novel dye-sensitized semiconductor systems for a higher solar-to-fuel activity. The

basic principle of dye-sensitized semiconductor for visible-light photocatalytic HER from water is illustrated in Figure 1.4. Typically, photoelectrons from the excited dye molecules adsorbed onto a semiconductor are injected into the CB of the semiconductor. The electrons are used for water reduction to generate molecular H<sub>2</sub>. The photogenerated holes left on dye molecules are subsequently consumed or regenerated by electrons from external electron donors.<sup>47</sup>

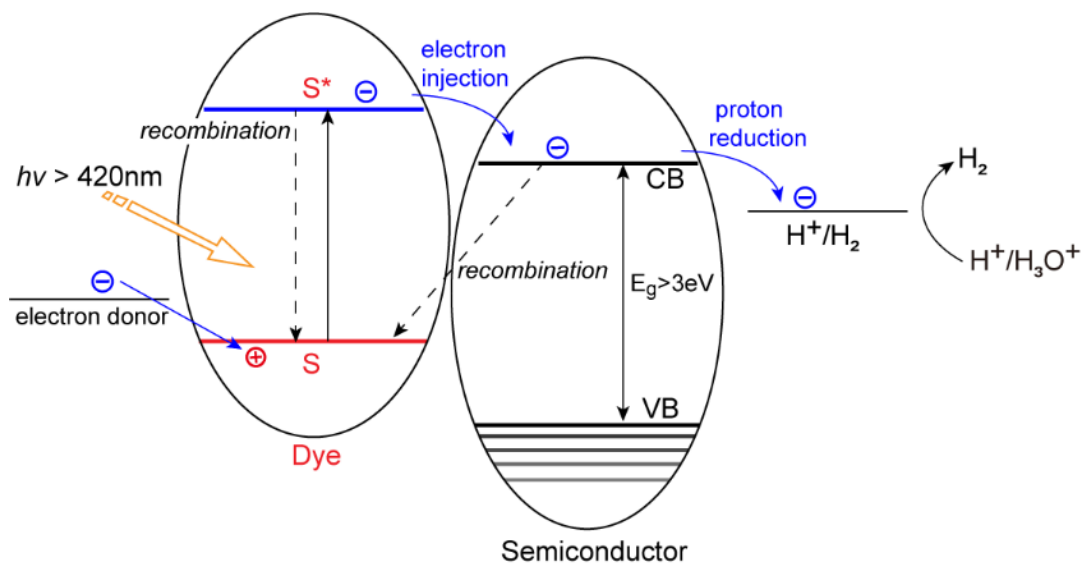


**Figure 1.4** Electron flow (solid lines) and possible recombination pathways (dotted lines) in dye-sensitized semiconductor photocatalytic systems.  $S^*$  and  $S$  refer to excited and ground state of dye, respectively.

Metal-free dyes compared with transition-metal complexes, such as Ir or Ru complexes, are more cost-effective and thus extensively studied for semiconductor sensitization. Among the dyes, coumarin dyes, melocyanine dyes, xanthene dyes, and porphine dyes have been reported to work effectively with semiconductor photocatalyst for HER. For example, a commercially available 8-hydroxyquinoline showed an excellent ability to sensitize anatase  $\text{TiO}_2$  to generate hydrogen by visible light.<sup>48</sup> A porphine derivative tetrakis-(4-carboxyphenyl) porphine (TPPC) sensitized Pt/ $\text{TiO}_2$  also exhibited an improved activity for  $\text{H}_2$  gas evolution from water, using ethylenediaminetetraacetic acid (EDTA) as electron donor.<sup>49</sup> The enhanced activity by dye sensitization could be ascribed to several factors such as the combined light adsorption of dye and semiconductor, different electron densities in excited states, and redox potentials in dye-semiconductor.

Particularly, Ti-based photocatalysts sensitized by Eosin Y such as Eosin Y-Rh/ $\text{TiO}_2$ <sup>50</sup> and Pt/ $\text{Na}_2\text{Ti}_2\text{O}_4(\text{OH})_2$ ,<sup>51</sup> were systemically studied for visible-light HER, showed outstanding performance and long-term activity, with average quantum yields over 10%. The Eosin Y-Pt sensitized  $\text{Na}_2\text{Ti}_2\text{O}_4(\text{OH})_2$  nanotubes achieved a higher quantum yield of 17.36% in HER although the structure was destroyed after long-term reaction. Amazingly,  $\text{Fe}^{3+}$  coupled  $\text{TiO}_2$  with Eosin Y-sensitization, without expensive metal, exhibited a high efficiency of light harvesting and visible-light photocatalytic activity, with maximum apparent quantum yield as high as 19.1% from aqueous medium.<sup>52</sup> While platinized

amorphous materials such as Pt/SiO<sub>2</sub> and Pt-multiwall carbon nanotube (Pt/MWCNT) sensitized by Eosin Y were reported for efficient photocatalytic HER, reaching remarkable quantum yields up to 10.4% and 12.14%, respectively.<sup>53,54</sup>

## **1.4 Strategies for increasing photocatalytic efficiency**

### 1.4.1 Semiconductor hybridization

Semiconductor hybridization is proven for increasing photocatalytic activity by promoting the charge separation. The hybridized semiconductors consist of two different semiconductors in direct contact forming a heterojunction. The hybridization can be categorized into three different types in terms of the band positions of the semiconductors in contact, as shown in Figure 1.5. Heterojunction type I shows a lowered VB of semiconductor B than that of semiconductor A, and a higher CB of semiconductor B than the CB of semiconductor A. The excited electrons can flow from CB(B) to CB(A), while the holes are driven diffusion from VB(B) to VB(A) by thermal equilibrium, otherwise, consumed by external electron donor. Thus, excited electrons are rapidly transferred onto semiconductor A for follow-up reactions, contributing to the charge carrier separation. Type II heterojunction is featured with a staggered energy structure and optimum band positions in the contacted semiconductors. Photoexcited electrons are transferred from CB(B) to CB(A), while the holes are driven diffusion from VB(A) to VB(B). Thus, photogenerated electrons and holes

are spatially separated, significantly reducing their recombination and thus prolonging the exciton lifetimes. In type III heterojunction, the band positions of the two semiconductors are even further set off. In most cases, the CB(A) is close to VB(B). Semiconductor system with such an energy band structure is also called Z-scheme system.

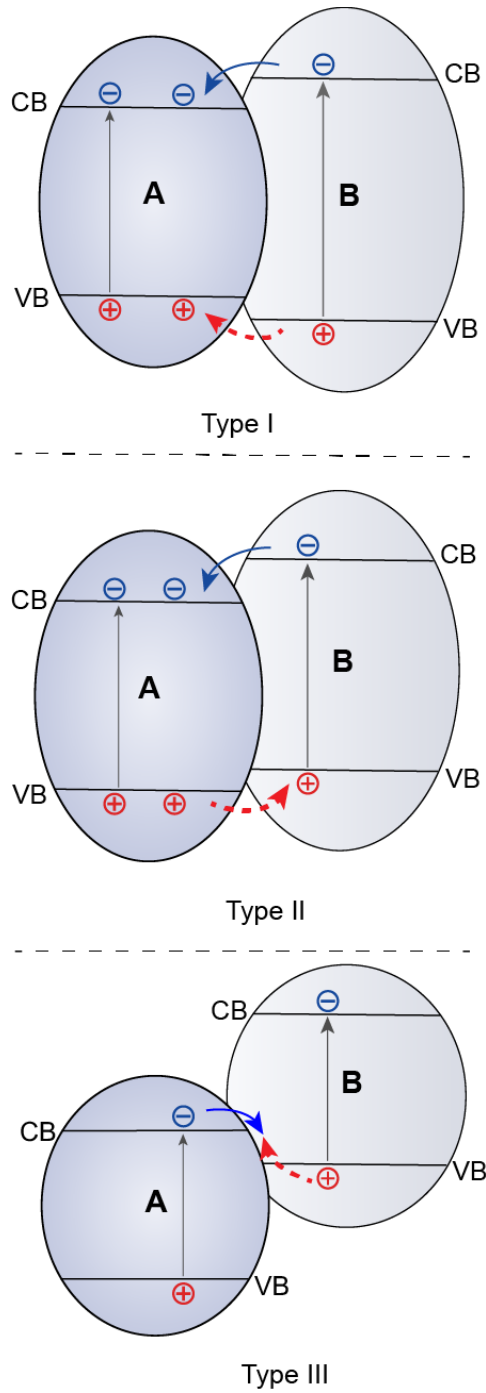


**Figure 1.5** Three types of semiconductor heterojunctions with different band position alignments.

These hybridized systems were proved to be superior to the individual component materials by the enhanced electron-hole separation capability. A hybridized oxide photocatalytic system of  $\text{TiO}_2/\text{SnO}_2$  showed the enhanced photocatalytic performance for  $\text{H}_2$  generation compared with single  $\text{TiO}_2$  by *ca.* 20 times.<sup>55</sup> Another case of combining  $\text{WO}_3$  with  $\text{TiON}$  into the  $\text{WO}_3\text{-TiO}_{2-x}\text{N}_x$  hybrid photocatalyst showed a higher visible-light HER activity than either  $\text{WO}_3$  or  $\text{TiO}_{2-x}\text{N}_x$  alone,<sup>56</sup> ascribed to the efficient separation of photogenerated electrons and holes by the staggered energy structure. With a similar charge transfer mechanism,  $\text{NaNbO}_3$  combined with a wide-bandgap semiconductor  $\text{In}_2\text{O}_3$  (2.8-3.3 eV)<sup>57-59</sup> was found effective to enhance both visible light HER activity and UV-induced pure water splitting performance over single  $\text{NaNbO}_3$ .<sup>60</sup> Another visible-light driven composite catalyst using multi-wall carbon nanotubes (MWCNTs) decorated on the  $\text{TiO}_2$  surface demonstrated the efficient electron-hole separation and HER performance, by the efficient transfer and transport of electrons from the visible-light excited MWCNTs to the contacted  $\text{TiO}_2$ .<sup>61</sup>

Heterojunctions constructed by coupling metal sulfides with other semiconductors particularly have received much interests for enhanced HER activity, arising from an intimate contact for interelectron transfer between two components. For example,  $\text{CuS}$  dots were deposited on  $\text{ZnS}$  NP by an in-situ cation exchange approach, forming typical type II heterojunctions that promote direct interfacial charge transfer.<sup>62</sup> By the improved charge separation and

transfer, combinations of sulfide semiconductors with staggered energy structure such as CuS/CdS<sup>63</sup> and CuS/Cd<sub>0.3</sub>Zn<sub>0.7</sub>S<sup>64</sup> photocatalysts were reported to have enhanced photocatalytic HER activity. To further improve photoelectron flow within each part, a three-component composite photocatalyst ZnS/CuS/CdS was developed, in which CuS served as the co-catalyst that trapped photoexcited electrons to drive holes reduction reaction.<sup>65</sup> In the case of CdS/Cu<sub>2</sub>S core-shell heterostructure, hydrogen evolution reaction was performed by Cu<sub>2</sub>S.<sup>66</sup> However, the photogenerated electrons from the excited CdS to Cu<sub>2</sub>S led to the reduction to Cu(0), which can retard the photogenerated electrons-holes recombination by forming a heterojunction. A further developed quaternary copper sulfide system Cu<sub>2</sub>XSnS<sub>4</sub> (X=Zn, Fe) was combined with Au into cases such as Au/Cu<sub>2</sub>ZnSnS<sub>4</sub>, Au/Cu<sub>2</sub>FeSnS<sub>4</sub> core-shell nanostructures.<sup>34, 35</sup> With Au NPs embedded, a significantly improved H<sub>2</sub> evolution activity was realized and ascribed to the localized surface plasmon resonance (LSPR) effect of Au NPs.

The intercalated incorporation of a guest semiconductor into interlayers of a lamellar host semiconductor presents to be a favorable method for the improvement of photocatalytic activity. In this hybridized structure, the recombination of photogenerated charge carriers is effectively suppressed by rapid charge transfer from the guest to the host semiconductor.<sup>67, 68</sup> So far, several transition metal oxide with lamellar structures have been proven as favorable intercalation hosts in photocatalysts.<sup>69-71</sup> For example, nanosized oxides (Fe<sub>2</sub>O<sub>3</sub> or TiO<sub>2</sub>) were reported intercalation into several layered metal oxides (i.e.,

$\text{HNb}(\text{Ta})\text{WO}_6$ , or  $\text{HLaNb}_2\text{O}_7$ )<sup>72, 73</sup>, the semiconductor system showed higher both UV and visible-light photocatalytic activities for HER. This is attributed to an effective separation of the photogenerated electrons and holes by electron transfer from guest semiconductor to the host semiconductor layers. In addition, a novel semiconductor composite photocatalyst from mesoporous zirconium titanium phosphate  $\text{Zr}_x\text{Ti}_y\text{P}$  (ZTP) combined with CdS was reported to work efficiently for visible-light HER.<sup>74</sup> Interestingly, the CB of ZTP can be modulated by changing the Zr/Ti ratio, achieving an optimal energy band match between the ZTP host and the CdS guest, which give rise to highly-efficient charge separation and  $\text{H}_2$  generation reactions. The highest quantum yield for this composite photocatalytic system (molar ratio Zr/Ti =1:3) reached 27.2% at 420 nm, one of the highest values among the advanced photocatalysts for HER application.

#### 1.4.2 Z-scheme system

The photosynthetic Z-scheme system in green plants includes two photosystems respective for molecular  $\text{H}_2$  and  $\text{O}_2$  evolution from water splitting reaction.<sup>75, 76</sup> It is reasonable to develop an artificial heterogenous Z-scheme photochemical system for overall water splitting reaction, since it is the most natural model for solar light harvesting and utilization. Typical Z-scheme photocatalytic system (type III) shown in Figure 1.5 comprises two contacted semiconductors with a largely set-off energy alignment. The excited electrons from CB (A) can recombine with the holes from VB(B), yielding higher redox capabilities of the

electrons from A and holes from B and strong driving forces to efficiently drive photocatalytic reactions.<sup>76</sup> An artificial all-solid-state Z-scheme photocatalytic system, Ru/SrTiO<sub>3</sub> doped with Rh-BiVO<sub>4</sub>, was applied for photocatalytic water splitting.<sup>13</sup> This system exhibited a much improved photocatalytic HER rate from pure water by four times higher than that of single Ru/SrTiO<sub>3</sub> doped with Rh. Interestingly, when an electron mediator, reduced graphene oxide, was introduced between the two components, a further 30% enhancement in HER performance was reached, demonstrating the importance of promoted charge flow within the Z-scheme photocatalytic system.<sup>77</sup> These work have inspired the design and fabrication of new and efficient artificial Z-Scheme systems for photocatalytic reduction reactions, such as H<sub>2</sub> generation from water and CO<sub>2</sub> conversion into hydrocarbons.

#### 1.4.3 Element doping

Limited by the wide bandgap, a number of pristine semiconductors, such as TiO<sub>2</sub>, ZnO, and ZnS, can absorb only UV light (4% total solar energy) in a solar spectrum for photochemical reactions. Various methods have been adopted to increase the solar energy harvesting and thus to promote the HER performance. So far, numerous works on improving photocatalysis by metal and/or nonmetal element-doped semiconductor catalysts have been reported. Some of them showed that the absorption range of semiconductors can be extended to visible-light region ( $\lambda \geq 420$  nm). This can be explained by the electronic transition of electrons from donor levels of dopant element to the CB of semiconductor (from

metal dopant energy level above VB to CB in Figure 1.6a). Different kinds of metal elements, such as transition metal elements (Ni, Fe, Cr, Mn, Sn, and V)<sup>78-82</sup> and rare earth elements (Ce, Sm and Eu),<sup>83</sup> have been selected as dopants for preparing visible-light responsive photocatalysts. However, there are some cases that excessive metal doping increases the number of recombination sites resulting in decreased photocatalytic activities.<sup>84, 85</sup> Besides, doping with non-metallic elements such as B, N, S, and C provides another way to prepare visible-light active semiconductor photocatalysts.<sup>86-90</sup> A pioneering work proposed that the light absorption range of N-doped TiO<sub>2</sub> can be extended to the visible light range because the energy gap of TiO<sub>2</sub> was narrowed down by the hybridization of N p states and O 2p states, leading to an improved photocatalytic activity.<sup>91</sup> Recent works presented both theoretical and experimental evidence that the N 2p states located above the VB and the visible light absorption is associated with the electronic transitions from N 2p states to CB in TiO<sub>2</sub>,<sup>92, 93</sup> as shown in Figure 1.6c. Unlike metal element dopant, non-metal dopants usually work as a substitute for lattice oxygen and are less likely to introduce recombination sites of photogenerated electron-hole pairs.<sup>94</sup>

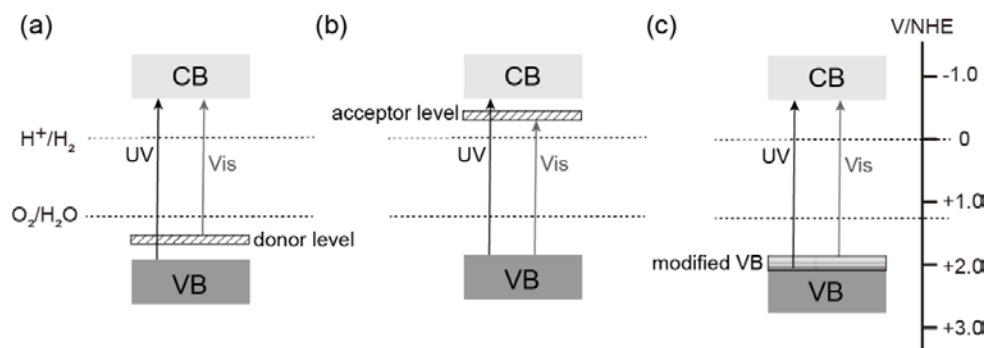


**Figure 1.6** (a) Donor level, (b) acceptor level formed by metal element doping and (c) modified energy structure formation by doping non-metal elements.

Metal/non-metal elements co-doped semiconductors present another dimension of photocatalysts aiming at improving photocatalytic activity.<sup>89, 95-98</sup> However, there are only a few studies on such systems for visible-light HER from water. Multiple metal/non-metal elements as the charge-compensated donor-acceptor pairs such as (Mo, C), (Cr, C), (Nb, N), and (N, V) were doped in combination into TiO<sub>2</sub>. In particular, TiO<sub>2</sub> doped by (Mo, C) showed a higher enhancement on photocatalytic HER among others.<sup>97</sup> This improvement can be ascribed to a reduced bandgap (<2.5 eV) for ideal visible-light region, without changing the CB position. The other wide-bandgap semiconductor ZnS showed to achieve visible-light-driven HER when Pb and halogens were used as dopant.<sup>99</sup> The introduction of Pb enabled the visible-light absorption, whereas the halogen doping was shown to suppress the recombination of photogenerated charge carriers. Another interesting example is Zn-doped In(OH)<sub>3</sub> with sulfur substitution, which exhibited much improved visible-light HER activity, ascribed to a synergistic role of Zn<sup>2+</sup>/S<sup>2-</sup> co-doping.<sup>100</sup> It was pointed out that Zn<sup>2+</sup> can level up the CB by hybridizing the In 5s5p and Zn 4s4p orbitals while the substitution of S<sup>2-</sup> narrowed down the bandgap by hybridizing S3p orbitals with O 2p orbitals in the VB. Such dual effect provided a strong driving force for HER from water.

#### 1.4.4 Cocatalyst loading

Most semiconductor photocatalysts cannot generate a large amount of H<sub>2</sub> from water without using cocatalyst, even with the assistance of electron donor. One

reason could be the rapid recombination of electron–hole pairs prior to migrating out for reactions. The other reason is the low rate of surface reaction which inefficiently consume the charge carrier. Suitable cocatalysts loaded on the semiconductor photocatalyst are reported to promote the photocatalytic process. Cocatalysts can work as the active reaction sites to catalyze reactions by lowering activation energies, to promote separation of electron-hole pairs , and transport the charge carriers by a built-in electric field at the junctions or interfaces of cocatalyst-host catalyst. Cocatalysts such as noble metals (Pt, Au, Pd etc.) and semiconductor (MoS<sub>2</sub>, RuO<sub>2</sub> etc.) are widely used as electron traps and effective proton reductions sites, thus significantly push up photocatalytic process.

#### 1.4.4.1 Metal cocatalysts

Transition metals, especially noble metal materials, are often used as effective cocatalysts for promoting photocatalytic reactions. A typical model of photogenerated exciton transfer process from photocatalyst to different cocatalysts is described in Figure 1.7. The lower Fermi level of noble metal than that of the semiconductor photocatalyst makes Pt a good cocatalyst, enabling photogenerated electrons migrated to the host photocatalyst surface to be trapped by Pt for reduction reaction.<sup>101</sup> Meanwhile, the holes are driven diffusion by thermal equilibrium to the photocatalyst surface or cocatalyst surface (e.g., IrO<sub>2</sub> and RuO<sub>2</sub>) for oxidation reaction. This results in an efficient and effective separation of the photogenerated electrons and holes. Overall, a greater photocatalytic activity for overall water splitting is highlighted by a combination

of promoted charge separation, reduced electron-hole recombination and inhibited reverse reactions.

To date, the highest visible-light photocatalytic HER rate by water splitting is achieved by Pt modified photocatalysts such as oxides, (oxy)sulfides, and (oxy)nitrides, realizing great enhancement in photochemical performance. Other noble metals like Au, Ag, Pd, Ru and Rh have also been documented as efficient cocatalysts.<sup>13, 102-104</sup> Among them, Au nanoparticles with fine morphology were found to work effectively by creating active sites for H<sub>2</sub> evolution and enhancing charge separation.<sup>105</sup> It is found that the reverse reaction of H<sub>2</sub> and O<sub>2</sub> into H<sub>2</sub>O on Au cocatalyst was negligible compared with that on Pt. This contributed to improved photocatalytic performances of several materials such as titanate (SrTiO<sub>3</sub>), niobate (KNbO<sub>3</sub>), and tantalate (NaTaO<sub>3</sub>) for overall water splitting. An unusual case was reported that only Ru on a TaON photocatalyst can promote much on HER rate but other metal cocatalysts such as Pt, Ir, and Rh.<sup>106</sup> It was proposed that the electronic structure of the Ru/TaON interface effectively promoted electron transfer from TaON to Ru for surface proton reaction. A systematic work on M/TiO<sub>2</sub> (M=Pt, Ru, Rh, Au, Ir, Cu, and Ni) was carried out on HER with low carbon monoxide selectivity from the photochemical reforming of glucose.<sup>107</sup> The loaded Rh was found to greatly increase the HER rate, attributed to the Schottky barrier built at the interface of Rh and TiO<sub>2</sub> for efficient electrons-trapping, thereby preventing the photogenerated charges recombination. This work suggests an avenue for selecting metal cocatalysts

considering the different electronic interactions with semiconductor photocatalyst surface. It was revealed that the lower Schottky barrier height at the metal/semiconductor junctions, the more efficiently electrons flow from excited semiconductor to metal, thus having a greater photochemical activity for H<sub>2</sub> gas generation.<sup>108</sup> For example, a Pt and Ru coloaded Y<sub>2</sub>Ta<sub>2</sub>O<sub>5</sub>N<sub>2</sub> demonstrated a superior activity for H<sub>2</sub> gas evolution over others using either Ru or Pt alone, arising from a synergistic effect of binary noble metal cocatalysts.<sup>109</sup> This binary metal coloaded can further retard the process of electron-hole recombination thus improve the charge separation efficiency.

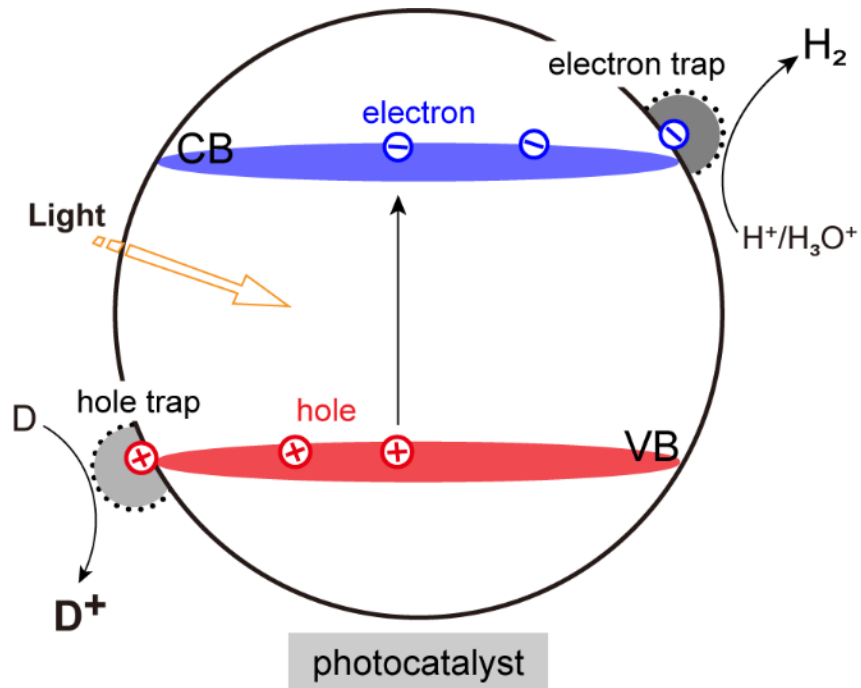


**Figure 1.7** Processes of charge transfer from a photocatalyst to cocatalyst for surface reduction and oxidation reaction, taking Pt and  $RuO_2$  as examples of cocatalysts, respectively. D is the electron donor and  $D^+$  is the oxidized electron donor by the photogenerated holes.

#### 1.4.4.2 Semiconductor cocatalysts

Transition-metal oxide semiconductors with low cost and nontoxicity are reported to be efficient cocatalysts for photocatalytic water splitting reaction. For example, the photocatalytic performance of  $\text{SrTiO}_3$  was much enhanced by a cocatalyst  $\text{NiO}$ , which did not cause the reverse water splitting reaction of  $\text{H}_2$  and  $\text{O}_2$  to form  $\text{H}_2\text{O}$ , unlike  $\text{Pt}$ .<sup>110</sup> Interestingly, a low amount of  $\text{NiO}$  loading on wide-bandgap oxide photocatalysts such as  $\text{Nb}_2\text{O}_5$  and  $\text{Ta}_2\text{O}_5$  made them active in photocatalytic HER from water.<sup>111, 112</sup> In addition, an activation pretreatment, a reduction and then oxidation, is often needed to produce highly active  $\text{NiO}$ -loaded photocatalysts. A double-layered  $\text{NiO}/\text{Ni}$  structure resulting from the pretreatment can be favorable to electrons flow from the photocatalyst to the  $\text{Ni}$  layer and consequently onto the  $\text{NiO}$  layer as the  $\text{H}_2$  evolution sites. Another case of using pretreated  $\text{NiO}$ -modified  $\text{ZnNb}_2\text{O}_6$  showed an improved photocatalytic activity in  $\text{H}_2$  reduction and  $\text{O}_2$  oxidation from water.<sup>113</sup> These work revealed that efficient charge transfer and the suppressed reverse reaction can contribute to the water splitting reaction on  $\text{NiO}$ .

$\text{RuO}_2$  has been widely used as a cocatalyst capable of trapping holes to drive oxidation reaction and facilitating water splitting process. For example, an inactive  $\beta\text{-Ge}_3\text{N}_4$  photocatalyst was found to become UV-photo catalytically when loaded with  $\text{RuO}_2$ .<sup>114, 115</sup> Furthermore, the  $\text{RuO}_2$  loaded on  $g\text{-C}_3\text{N}_4$  surface can boost water splitting by an improved  $\text{O}_2$  evolution activity and meanwhile stabilizes the  $g\text{-C}_3\text{N}_4$  against oxidative decomposition.<sup>116</sup> A synergistic effect in

enhancing catalytic activity of  $\text{TiO}_2$  was achieved by co-depositing  $\text{RuO}_2$  and Pt, which is ascribed to building an Ohmic contact between Pt and  $\text{TiO}_2$  and a Schottky barrier between  $\text{RuO}_2$  and  $\text{TiO}_2$ .<sup>117, 118</sup> This can direct electrons flow to the Pt while the holes were trapped by  $\text{RuO}_2$ , causing an efficient charge separation and promoted photocatalytic reaction. Furthermore,  $\text{RuO}_2$  nanoclusters dispersed on  $\text{GaN}_{1-x}\text{ZnO}_x$  surface were found superior to both Ru (IV) species and particulate  $\text{RuO}_2$  for boosting up the photocatalytic  $\text{H}_2$  and  $\text{O}_2$  gas evolution by overall water splitting.<sup>119</sup>

Besides noble metals and metal oxide semiconductors, metal sulfide semiconductors have also been developed into promising cocatalysts. A study on  $\text{MoS}_2/\text{CdS}$  found that the junctions between host photocatalyst CdS and cocatalyst  $\text{MoS}_2$  lead to a much higher photocatalytic HER activity than Pt/CdS using lactic acid as the sacrificial electron donor although Pt has superior property to  $\text{MoS}_2$  for  $\text{H}_2$  activation.<sup>120</sup> The  $\text{MoS}_2/\text{CdS}$  heterojunction is found to be responsible for the higher photocatalytic HER activity than the CdS/ $\text{MoS}_2$  mixture, confirming the facilitated electron transport by the intimate contact between CdS and cocatalyst  $\text{MoS}_2$ . Similar results were found on CdS modified by  $\text{WS}_2$  as the cocatalyst which showed significantly improved activity of  $\text{H}_2$  generation. Further work revealed that  $\text{MoS}_2$  can work more effectively for  $\text{H}_2$  generation on CdSe-nanoribbon photocatalyst than Pt.<sup>121</sup> Several other metal sulfides such as PbS,  $\text{Rh}_2\text{S}_3$ , and  $\text{Ru}_2\text{S}_3$  by a low loading are found to greatly

enhance the photocatalytic activity of CdS for H<sub>2</sub> gas generation when loaded in a small amount.<sup>122</sup>

Recently, transition metal phosphides (TMPs) have been emerged as another class of highly active materials for photocatalytic HER, making them potential cocatalysts for STH reaction due to the promoted charge separation at the TMP/semiconductor interface.<sup>123</sup> FeP nanoparticles was firstly reported to work as a cocatalyst with TiO<sub>2</sub> to enhance the photocatalytic HER activity from aqueous solution.<sup>124</sup> Another work reported that both Ni<sub>2</sub>P and Co<sub>2</sub>P can be used as efficient cocatalysts anchored on CdS nanorods for photocatalytic HER.<sup>125</sup> It is also interesting that the band gap of metal phosphides can be adjusted by lowering P content which limits the electron delocalization. Thus, metal phosphides with appropriate P content are considered to be a potential photocatalyst for photocatalytic HER. For example, a semi-metallic MoP<sub>2</sub> can work actively in water reduction to produce H<sub>2</sub> gas under visible light, using a cocatalyst Pt and sacrificial electron donor.<sup>126</sup> This work may present a platform to devise appropriate TMPs as a new class of cocatalysts for effective H<sub>2</sub> gas evolution through water splitting. These cases all highlight the importance of the charge separation and transport at the interface between semiconductor photocatalyst and semiconductor cocatalyst for improving photocatalytic HER performance.

#### 1.4.5 Surface and interface engineering

Great efforts have been taken on the semiconductor energy band engineering, in developing narrow-bandgap semiconductors and doping wide-bandgap semiconductor materials. In contrast, surface and interface engineering receives much less attention until recently wide-bandgap semiconductors such as TiO<sub>2</sub>, ZnS and Ga<sub>2</sub>O<sub>3</sub> with modified surface and interface were reported to show improved photocatalytic HER performances. Disordered surface was constructed on TiO<sub>2</sub> by hydrogenation that introduced a much-narrowed bandgap with an upshifted VB position of *ca.* 2 eV.<sup>127</sup> This much decreased the energy needed for exciton generation, thereby allowing the use of visible-NIR light in solar spectrum. However, visible light absorption was found to have little contribution to the photoactivity of the TiO<sub>2</sub> although there was dramatic improvement in photocatalytic activity. As a result, the HER rate of the platinized black TiO<sub>2</sub> decreased by *ca.* 100 times when visible-NIR light irradiation was used.

More recently, several interface engineering on the semiconductor by building the homojunctions between two crystal phases (in Figure 1.8) have been much reported to have impressive enhancement in photocatalytic HER. It is found that a type-II energy structure can be formed in addition to the homojunctions, enabling an effective and efficient separation of photogenerated electrons and holes at interfaces. For example, the established phase-junctions ( $\alpha$ - $\beta$  phases) in Ga<sub>2</sub>O<sub>3</sub> made this material active in photocatalytic overall water splitting, with *ca.* three and seven times higher activities than those of single  $\alpha$ - and  $\beta$ -Ga<sub>2</sub>O<sub>3</sub>,

respectively.<sup>128</sup> Similarly, ZnS with multiple wurtzite-sphalerite phase-junctions showed a boosted photocatalytic HER rate by *ca.* 70 times over that of ZnS without junctions.<sup>129</sup> Additionally, the multiple interfaces between phase-junctions are believed to work as the location for charge separation and the transfer tunnel that help promoting the charge kinetics, as a key factor for photocatalytic reactions. These works suggest a challenging but important research topic on surface and interface engineering in wide bandgap semiconductors for the drastically enhanced photoactivity in HER.

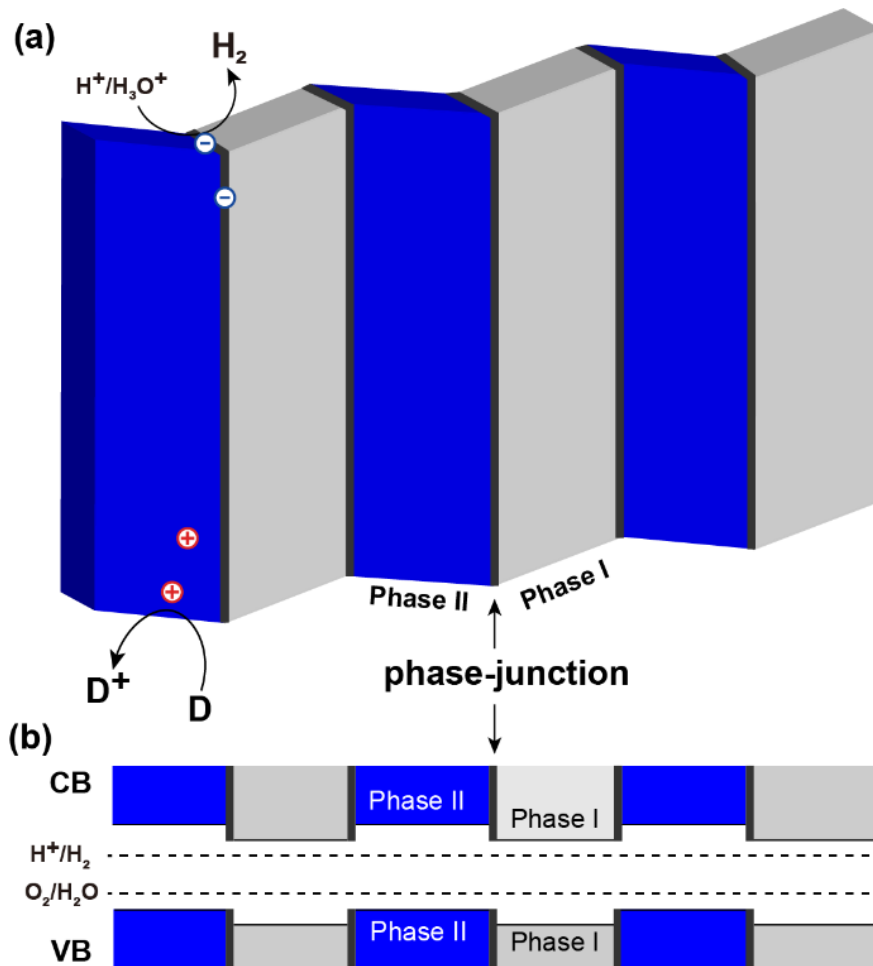


**Figure 1.8** (a) Interface engineering on a semiconductor photocatalyst by multiple junctions with alternating two crystal phases segments; (b) The alternating pattern of crystal phases with staggered energy structure.

#### 1.4.6 Plasmonic effect

Plasmons are from the collective oscillation of free charges confined to the surface of highly conductive materials. Materials that have surface plasmonic resonance (SPR) in the visible and NIR region are required to have a free charge-carrier concentration up to  $10^{21} \text{ cm}^{-3}$ .<sup>130</sup> To this point, metal nanoparticles, such as Au, Ag, Cu, and Al nanoparticles, are proven materials that have SPR by strong interaction with light.<sup>131</sup> Interestingly, the localized electric fields at the surface of nanoparticles can be generated by irradiating the light at the plasmon frequency of metal nanoparticles, which can be adjusted by altering the nanoparticle size and morphology. For example, the plasmon resonance of Au nanoparticle can be red-shifted from 517 to 575 nm by increasing the nanoparticle size from 22 to 99 nm.<sup>132</sup> Further, the localized SPR (LSPR) can be generated when the resonant excitation is focused into a nanoscale region, making significant enhancement in the electric field on the plasmonic metal, shown in Figure 1.9 (a).<sup>133, 134</sup> However, since the field intensity is maximal at the metal surface and decaying exponentially away from the surface, an increased curvature of metal nanocrystals can further enhance field intensity. Consequently, a sharper metal nanocrystal can bring a stronger field enhancement.<sup>135</sup> With the enhanced field close to a semiconductor by a plasmonic metal-semiconductor heterojunction, plasmonic energy can be transferred from a plasmonic metal to the semiconductor in contact. The other route for plasmon-enhanced photochemical reactions is known as hot electron injection, shown in Figure 1.9(b). Upon light excitation, a plasmon quantum can decay into a hot

electron/hole pair. The injection of hot electrons taking place at the metal/semiconductor junction transfer from the metal to semiconductor upon the excitation of the LSPR. However, a Schottky barrier can be established at the junction interface, where the reflux of electron from the metal to semiconductor can be blocked. The hot electrons, if with sufficiently high energy, can overcome the Schottky barrier to effectively inject into the CB of the semiconductor in contact. Also, the Schottky barrier can hinder the backflow of electrons from metal to semiconductor, making possible spatial separation of electrons and holes and hence reduced recombination, which can enhance the photocatalytic activity.

The correlation of hybrid nanostructures with the photocatalytic activity of HER was studied by comparing Janus and core-shell Au/TiO<sub>2</sub> nanostructures on the photocatalytic HER from water.<sup>136</sup> Both Au/TiO<sub>2</sub> nanostructures exhibited greatly increased HER rates by visible light. However, the amount of H<sub>2</sub> gas generated from the Janus Au/TiO<sub>2</sub> nanostructure is 170% more than that from the core/yolk-shell counterpart. This greater enhancement in Janus Au/TiO<sub>2</sub> comes from a closer localized plasmon field near the interface, combined with the reduced probability of electron-hole recombination. Besides, larger Au nanocrystals were found to generate higher photocatalytic activity, coming from a stronger plasmon-enhanced field and more effective hot electron injection.

In addition, plasmonic energy from the metal can non-radiatively transfer to the contacted semiconductor through a plasmon-induced resonance energy transfer process (PIRET), as shown in Figure 1.9(c). The plasmons in the excited metal can generate a strong dipole, which induces the formation of a dipole in the semiconductor by a dipole-dipole interaction, generating electron-hole pair in the semiconductor.<sup>137</sup> The PIRET process can take place within an insulating space up to *ca.* 25 nm in-between the metal-semiconductor, with energy transfer efficiency dependent on primary two factors.<sup>138</sup> The first factor is the distance between the plasmonic metal and the semiconductor, and the other is the spectral overlap of the plasmonic resonance band and the absorption band of semiconductor. The PIRET process can be tuned by the spectral overlap and the spatial distance in-between the metal-semiconductor.<sup>139</sup> For example, PIRET can take place in the Ag-SiO<sub>2</sub>-TiO<sub>2</sub> core-insulator-shell nanostructure coming from the spectral overlap of Ag and TiO<sub>2</sub>. However, no PIRET happens in the Au-SiO<sub>2</sub>-TiO<sub>2</sub> core-insulator-shell nanostructure due to the insulating space layer SiO<sub>2</sub> and no spectral overlap of Au and TiO<sub>2</sub>.

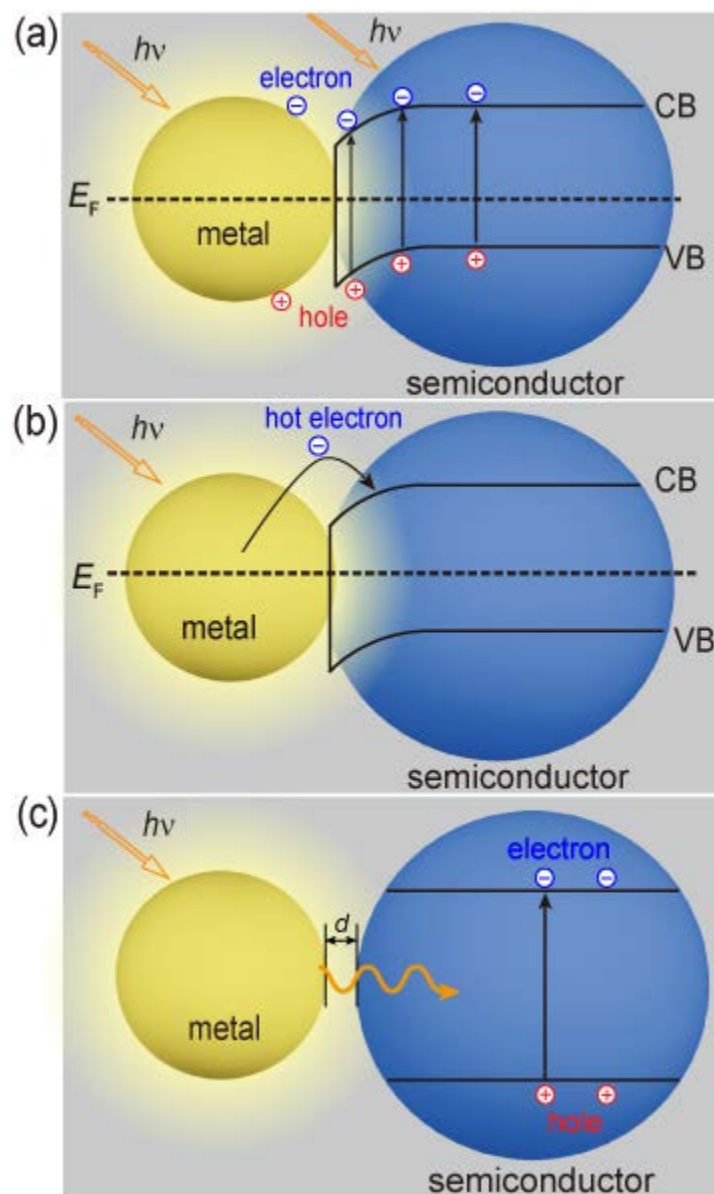


**Figure 1.9** Schematic mechanisms for plasmon-enhanced photochemical reactions by constructing metal/*p*-type semiconductor nanostructures. (a) Plasmon-enhanced light absorption. (b) Hot-electron effect; (c) Plasmon-induced resonance energy transfer.  $E_F$  is the Fermi energy level,  $d$  refers to the nanoscale distance between plasmonic metal and semiconductor nanomaterial.

## 1.5. Aims and objectives

Demands for sustainable development and environment protection turn our perspectives to infinite solar energy for energy conversion and storage. Converting solar energy through photocatalysis into high-value fuels such as H<sub>2</sub> gas from water has been considered to be a promising approach. To date, a major concern in this field is the development of low-cost, non-toxic, and highly-efficient photocatalytic systems. Among the systems studied, earth-abundant metal sulfide photocatalysts present to be promising candidates for this application owing to their relative low-cost, natural abundance of the elements, and the potential reactivity. The objective of this thesis is to boost up the rate of photocatalytic H<sub>2</sub> gas evolution reaction in water by constructing heterojunction and/or homojunction on semiconductor nanostructures and by utilizing the surface plasmon resonance effects. In this thesis, studies on the photocatalytic activities of ZnS nanoparticles and copper sulfide nanoparticles with multiple homojunctions, Cu<sub>1.8</sub>S nanocage yolk-shell nanoparticle embedded with Au nanoparticles of various shapes, and Au nanorod decorated with multiple Cu<sub>1.8</sub>S nanocages nanoparticle to carry out proton reduction reaction in water under simulated sunlight are discussed.

Chapter 1 is a general introduction to the background, problems and, strategies of photocatalytic hydrogen evolution from water. Up to date approaches to synthesize semiconductor photocatalyst and enhance solar-driven photocatalysts are reviewed. The thesis framework is outlined at the end of this chapter.

Chapter 2 summarizes the methodologies used for the experiments including the experimental setup, sample preparation and characterization for photocatalytic reaction.

Chapter 3 describes a two-step hydrothermal method for preparing ZnS nanocrystals with multiple homojunctions consisting of parallel sphalerite phase and wurtzite phase. By modulating the two-phase composition in ZnS nanocrystals, photocatalytic test gives the optimal H<sub>2</sub> gas evolution performance of ~70 times enhancement over normal ZnS without homojunctions.

In Chapter 4, a synthetic protocol of multiple homojunctions was developed by an ethylenediamine-mediated hydrothermal method on copper sulfides with various Cu and S compositions. Multiple homojunctions from hexagonal CuS-hexagonal Cu<sub>1.8</sub>S and hexagonal Cu<sub>1.8</sub>S-monoclinic Cu<sub>1.75</sub>S were constructed on copper sulfide nanoparticles, respectively, to establish multiple type-II energy gap within the copper sulfide nanoparticles, in order to better separate the photogenerated charge carriers. The hydrogen evolution rate of the copper sulfide with multiple homojunctions has increased by 230% from that of copper sulfide without homojunctions.

Chapter 5 presents the establishment of a Schottky junction between plasmonic Au nanomaterials and Cu<sub>1.8</sub>S to form the hetero-interfaces. The plasmons from

Au nanomaterials promote the photocatalytic activity of the nearby  $\text{Cu}_{1.8}\text{S}$ , by different levels of plasmonic effects from Au nanoparticles of various shapes. The Au- $\text{Cu}_{1.8}\text{S}$  hetero-nanostructure can offer an understanding in the mechanism of plasmonic energy transfer from plasmonic metals to semiconductors. Detailed preparation, characterization, and photocatalytic studies will be discussed.

Chapter 6 introduces a  $\text{Cu}_{1.8}\text{S}$  nanocage-Au nanorod supramolecular nanostructure that exhibits the antenna effect of plasmonic metal on semiconductor for using surface plasmon resonance effect on photocatalysis.

Finally, in Chapter 7 conclusions from Chapter 3 to 6 is summarized and future research directions are suggested. Future investigations will be put on cost-effective plasmonic metals (such as Cu, Al, Bi) and earth-abundant semiconductor materials. The chemical composition, micro/nanostructure, and electronic structure of plasmonic metal/semiconductor will then be explored. By designing high-performance plasmonic photocatalyst with metal-semiconductor heterojunctions, the efficiency of plasmonic energy transfer can be improved to drive photochemical reactions such as solar-to-hydrogen conversion.

## **Chapter 2**

### **Experimental Section and Characterization Techniques**

## 2.1 Materials

Unless otherwise specified, all chemicals were used as received without further purification. Zinc acetate ( $\text{Zn(OAc)}_2$ ), *L*-cysteine (98%), ethylenediamine (99%), hexadecyltrimethylammonium bromide (CTAB) ( $\geq 99\%$ ), gold(III) chloride ( $\text{HAuCl}_4$ ) ( $\geq 49.0\%$  Au basis), sodium borohydride ( $\text{NaBH}_4$ ) ( $\geq 98\%$ ), *L*-ascorbic acid (AA) ( $\geq 99\%$ ), hydrochloric acid (HCl) (37%),  $\text{AgNO}_3$  ( $\geq 99\%$ ) hexadecyltrimethylammonium chloride (CTAC) ( $\geq 98\%$ ), copper(II) nitrate (98%), sodium dodecylbenzene sulfonate (SDBS) ( $\geq 95\%$ ), hydroxylamine hydrochloride ( $\text{NH}_2\text{OH}\cdot\text{HCl}$ ) ( $\geq 99\%$ ), NaOH (97%) and  $\text{Na}_2\text{S}$  ( $\geq 98\%$ ) were purchased from Sigma-Aldrich. Analytical grade methanol was purchased from Meck Chemicals.

## 2.2 Synthesis

2.2.1 ZnS nanocrystal with parallel phase-junctions for photocatalytic water reduction to hydrogen

2.2.1.1  $\text{ZnS}(\text{ethylenediamine})_{0.5}$  as precursor

ZnS nanocrystals were prepared via hydrothermal treatment of the  $\text{ZnS}(\text{en})_{0.5}$  (en=ethylenediamine) precursor. The precursor was prepared by an ethylenediamine-mediated solvothermal method. In a typical synthesis, 2 mmol  $\text{Zn(OAc)}_2$  and 4 mmol *L*-cysteine were dispersed in 30 mL ethylenediamine by stirring until the solution becomes transparent. The mixture was then placed into a 50-mL Teflon-lined stainless-steel autoclave and maintained at 180 °C for 24

h. After that, the resulting precursor as precipitate was collected by centrifugation, washed with deionized water (DI water) and absolute ethanol respectively for three times, then dried in a vacuum oven at room temperature.

#### 2.2.1.2 ZnS nanocrystal with parallel phase-junctions

In a typical synthesis, 50 mg of the dried precursor was placed in 30 mL DI-water by vigorous stirring until well-dispersed. The mixture was transferred into a 50-mL Teflon-lined stainless-steel autoclave followed by hydrothermal treatment at 140, 180, 220 and 260 °C for 12 h. After that, the precipitate was collected by centrifugation, washed with DI water and absolute ethanol respectively for three times, then dried in a vacuum oven at room temperature. The dried products are labeled as ZS-1, ZS-2, ZS-3 and ZS-4, respectively.

#### 2.2.2 Cu<sub>x</sub>S nanocrystals with phase-junctions for photocatalytic water reduction to hydrogen

##### 2.2.2.1 Cu<sub>x</sub>S (x=1, 1.8, 1.75, 2) nanocrystals

In typical synthesis, 0.5 mmol of Cu(oleate)<sub>2</sub> was dissolved in anhydrous ethylenediamine (0 mL, 2 mL, 5 mL, 10 mL, respectively) and stirred until a blue solution was obtained. Then 0.5 mmol *L*-cysteine was added to the above solution. After 30 min of magnetic stirring, the total volume of the solution was adjusted to 10 mL by adding DI water. The content of ethylenediamine is controlled to be

0 vol%, 20 vol%, 50 vol%, 100 vol%, respectively. Then the mixture was transferred into a 15 mL Teflon-lined stainless-steel autoclave, which was then sealed and maintained at 120 °C respectively for 4 h. After that, the autoclave was cooled down naturally and a solid precipitate was produced, which was washed by DI water and absolute ethanol three times to removed unreacted species, and collected by centrifugation. Finally, purified samples were dried in vacuum at room temperature for overnight. The obtained products were labelled as CS-1, CS-2, CS-3, and CS-4, respectively.

#### 2.2.2.2 Cu<sub>x</sub>S nanocrystal with phase-junctions

Cu<sub>x</sub>S nanocrystals with multiple phase-junctions were prepared by adjusting the content of ethylenediamine in the solvent. Firstly, 0.5 mmol of Cu(oleate)<sub>2</sub> was dispersed in anhydrous ethylenediamine (0.5 mL, 2.5 mL, 7.5 mL, and 9 mL) and stirred until a blue solution was obtained. Then 0.5 mmol *L*-cysteine was added to the above solution followed by vigorous magnetic stirring. The total volume of the solvent was adjusted to 10 mL by adding DI water, and placed to 15-mL Teflon-lined stainless-steel autoclave. The autoclave was sealed and maintained at 120 °C respectively for 4 h. After that, the autoclave was cooled down naturally and a solid precipitate was produced. The product was washed by absolute ethanol several times, and then collected by centrifugation. Samples were dried in vacuum at room temperature for overnight.

### 2.2.3 Au nanomaterials embedded Cu<sub>1.8</sub>S hollow nanocage for photocatalytic water reduction to hydrogen

#### 2.2.3.1 Au nanomaterials

Au nanospheres were prepared by a citrate-stabilized seed approach. Firstly, 1.4 mL sodium citrate solution (1wt%) was added into 200 mL boiling HAuCl<sub>4</sub> solution (0.01wt%). The mixture was under vigorous stirring and refluxed for 1h. Upon cooling the Au sol of spherical nanoparticles was yielded, then 20 mL of 30 mM SDBS was added dropwise and kept stirred overnight. The obtained solution was centrifuged at 8000 rpm for 10 min, followed by storage in 50 mL SDBS (30 mM) solution.

Au nanorods were obtained by seed-mediated growth approach from modified previous reports. Typically, 600  $\mu$ L NaBH<sub>4</sub> (10 mM) was injected into a 10 mL CTAB (100 mM) aqueous solution containing 250  $\mu$ L HAuCl<sub>4</sub> (10 mM) to obtain the seed solution, which was placed at room temperature for 2 h. Growth solution was prepared by adding 2 mL HAuCl<sub>4</sub> (10 mM), 75  $\mu$ L AgNO<sub>3</sub> (10 mM), 0.32 mL ascorbic acid (AA) (0.1M), and 0.8 mL HCl (1.0 M) into 40mL CTAB solution (0.1 M). Then, 96  $\mu$ L of the synthesized seed solution was added to the growth solution, which was placed at room temperature for 6 h for Au nanorods formation. The mixture was centrifuged and concentrated into 20 mL aqueous solution. Subsequently, 40 mL CTAC (80 mM) and 40 mL SDBS (30 mM) were

added to the above solution for overnight stirring. The mixed solution was centrifuged and stored in the 20 mL SDBS (30mM) for next step.

Au nanostars were synthesized from a seed solution. Firstly, 5 mL of sodium citrate solution (34 mM) was injected to 95 mL of boiling H<sub>AuCl</sub><sub>4</sub> solution (0.5 mM) under vigorous stirring. After boiling for 15 min, the solution was cooled down to 4 °C. This solution was kept as seed solution. Secondly, 2.5 mL of the citrate-stabilized Au seed solution was injected to 50 mL of H<sub>AuCl</sub><sub>4</sub> (0.25 mM) (pH adjusted by 1M HCl) at room temperature, followed by the dropwise addition of 0.5 mL AgNO<sub>3</sub> (3 mM) and 0.25 mL AA (100 mM). After that, 20 mL SDBS (30 mM) was added dropwise and kept stirring overnight. The obtained solution was centrifuged at 8000 rpm for 10 min and stored in 15 mL SDBS (30 mM) solution.

#### 2.2.3.2 Cu<sub>1.8</sub>S hollow nanocage

Cu<sub>2</sub>O nanocube is firstly prepared and used as a precursor. The synthetic route refers to reported literature with modification. Typically, a 0.5 mL Cu (NO<sub>3</sub>)<sub>2</sub> (0.1 M) aqueous solution was injected to 10 mL SDBS aqueous solution under vigorous stirring for 10 min until well mixed. To this solution, 0.2 mL NH<sub>2</sub>OH·HCl (0.2 M) was added dropwise, followed by fast injection of 0.18 mL NaOH (1.0 M) aqueous solution. The mixed solution rapidly turned greenish and gradually became turbid yellow. After stirring for 1 h, the solution was quenched

by adding 2 mL methanol and centrifuged to remove the supernatant. A light-yellow product was obtained and stored in methanol. The as-prepared Cu<sub>2</sub>O nanocube in methanol was stirred in an ice bath for 20 min. A 0.1 mL Na<sub>2</sub>S (50 mM) aqueous solution was quickly injected to the cooled suspension and kept vigorous mixing for 5 min. After centrifuge, dark yellow product was obtained and re-dispersed in methanol, then 0.2 mL HCl (aq) (20 mM) was added dropwise to etch the Cu<sub>2</sub>O core. The color of mixed solution gradually turned dark brown. After centrifuge, a dark brown product was collected after removing the supernatant. The product was re-dispersed in methanol and stored at room temperature.

#### 2.2.3.3 Au nanosphere embedded Cu<sub>1.8</sub>S hollow nanocage

Au nanosphere (55 nm) embedded Cu<sub>2</sub>O was firstly prepared and used as the precursor. Typically, a 0.5 mL Cu (NO<sub>3</sub>)<sub>2</sub> (0.1 M) aqueous solution was injected to 10 mL as-prepared Au nanosphere solution under vigorous stirring until well mixed. To this solution, 0.2 mL NH<sub>2</sub>OH·HCl (0.2 M) was added dropwise followed by fast injection of 0.18 mL NaOH (1.0 M) aqueous solution. The mixed solution rapidly turned greenish and gradually became turbid yellow. After stirring for 1 h, the solution was quenched by adding 2 mL methanol and centrifuged to remove the supernatant, a light-yellow product was obtained and stored in methanol. The as-prepared Au nanorod embedded Cu<sub>2</sub>O nanocube in methanol was under stirring and kept in ice bath for 20 min. A 0.1 mL Na<sub>2</sub>S (50 mM) aqueous solution was fast injected to the cooled suspension and kept

vigorous mixing for 5 min. After centrifuge, dark yellow product was obtained and re-dispersed in methanol, then 0.2 mL HCl (aq) (20 mM) was added dropwise to etch the Cu<sub>2</sub>O core, the mixed solution continued to be stirring for 20 min and the color turned dark brown. After removing the supernatant by centrifugation, a dark brown product was obtained. The product was re-dispersed in methanol and stored at room temperature.

#### 2.2.3.4 Au nanorod embedded Cu<sub>1.8</sub>S hollow nanocage

Au nanorod embedded Cu<sub>2</sub>O nanocube as the precursor was firstly prepared and treated similarly as the case of Au nanosphere embedded Cu<sub>2</sub>O. Finally, Au nanorod-Cu<sub>1.8</sub>S nanocage was re-dispersed in methanol and stored at room temperature.

#### 2.2.3.5 Au nanostar embedded Cu<sub>1.8</sub>S hollow nanocage

Au nanostar embedded Cu<sub>2</sub>O as the precursor was first prepared and treated similarly with the case of Au nanosphere embedded Cu<sub>2</sub>O. Finally, the product Au nanostar-Cu<sub>1.8</sub>S nanocage was re-dispersed in methanol and stored at room temperature.

#### 2.2.4 Cu<sub>1.8</sub>S nanocage decorated Au nanorod for photocatalytic water reduction to hydrogen

#### 2.2.4.1 Cu<sub>2</sub>O nanocube decorated Au nanorod

Typically, a 0.125 mL Cu(NO<sub>3</sub>)<sub>2</sub> (0.1 M) aqueous solution was injected to 10 mL as-prepared Au nanorod solution under vigorous stirring for 10 min until well mixed. To this solution, 50 μL NH<sub>2</sub>OH·HCl (0.2 M) was added and then 45 μL NaOH (1.0 M) aqueous solution was rapidly injected. The mixed solution turned deep red. After stirring for 5 min, the solution was quenched by adding 2 mL methanol and centrifuged to remove the supernatant. A deep red product was obtained and stored in methanol.

#### 2.2.4.2. Cu<sub>1.8</sub>S nanocage decorated Au nanorod

The as-prepared Au nanorod embedded Cu<sub>2</sub>O nanocube in methanol was stirred in ice bath for 30 min. A 50 μL Na<sub>2</sub>S (20 mM) aqueous solution was fast injected to the cooled suspension and kept vigorous mixing for 10 min. After centrifuge, a dark red product was obtained and re-dispersed in methanol, and then 50 μL HCl (aq) (20 mM) was added dropwise to etch the Cu<sub>2</sub>O core. The solution was stirred for 20 min and the color turned dark brown. After centrifuge, a dark brown product was obtained after removing the supernatant. The product was re-dispersed in methanol and stored at room temperature.

### **2.3 Characterization techniques**

#### 2.3.1 Transmission electron microscopy

Transmission electron microscopy (TEM) is a microscopic technique by which the transmittance of electron beam through a sample is adopted to produce images. The TEM is capable of imaging at a significantly higher resolution (down to 0.1 nm) than optical microscopes, because of the smaller de Broglie wavelength of incident electrons. This enables the TEM apparatus to observe a small object down to a single column of atoms. The focused beam of electrons is accelerated and transmitted through a thin layer of sample (~100 nm). The direction of beam can be changed by the collisions between the electrons and sample atoms, producing a solid angle scattering. The sample morphology is imaged by the light scattering on a fluorescent screen and captured by the charge-coupled device (CCD) camera. The amount of electron beam interaction with the sample depends on the atomic number of the sample. Atoms with a larger atomic number interact with the electron beam more strongly, creating a darker area in the image. By contrast, the bare background is left unchanged and will therefore appear bright, this technique is known as bright field TEM. A lower wavelength X-ray could be used to increase the resolution of a TEM image. According to the Planck-Einstein equation,

$$E = h\nu$$

where  $E$  is the energy of photon,  $h$  is Planck's constant, and  $\nu$  is the frequency of photon, since a higher frequency X-ray beam can also have a higher energy, therefore the sample degradation may occur if the electron beam is excessively energetic, which limits the resolution of TEM. TEM images were collected using a STEM (JEOL JEM-2100F) operated at 200 kV.

TEM samples were made by drop-casting 10  $\mu\text{L}$  ethanol solution of nanomaterials onto the holey carbon-coated 400 mesh copper or nickel TEM grids. Sample-ethanol solutions were obtained by sonication until well-dispersed.

### 2.3.2 Powder X-ray diffraction

Powder X-ray diffraction (XRD) is a simple and accurate technique for characterizing crystallographic orientation at an atomic level. X-rays can be taken as the electromagnetic waves of radiation, which are scattered by atoms, primarily through the electrons of atoms. The X-ray striking an electron generates secondary spherical waves of a lower energy from the electron. When the sample is irradiated by X-ray, the beam is scattered by each layer of atoms and forms scattering waves. All these waves interfere with one another from different atoms, either constructively or destructively, depending on the phase difference of the scattered X-ray, and produce a diffraction pattern as a result, according to Bragg's law,

$$n\lambda = 2d \sin \theta$$

where  $n$  is a positive integer (normally taken as 1),  $\lambda$  is the wavelength of the X-ray wave,  $d$  is the lattice interspacing between crystal planes, and  $\theta$  is the incident beam angle.

For nanomaterials smaller than 100 nm in diameter, the grain boundaries would enable X-ray to scatter, leading to a line broadening in their X-ray diffraction pattern. This broadening phenomenon is described by the Scherrer Equation,

$$\tau = \frac{K\lambda}{\beta \cos(\theta)}$$

where  $\tau$  is the mean crystal domains,  $K$  is the form factor (typically 0.9 for a cubic system),  $\lambda$  is the wavelength of X-ray,  $\beta$  is the line broadening of full width half at maximum (FWHM), and  $\theta$  is the Bragg angle. This equation can be used to determine the lower boundary of the particle size.

The wavelength light is generated by an anode material, typically copper, and the intensity is limited by the power applied and cooling capacity to avoid the anode melting. Therefore, electrons are excited from the cathode material and accelerated by a high electric potential of *ca.* 50 kV. The X-ray is generated by the relaxation of higher-shell electrons to the K-shell (1s). If the electron is from the 2p orbital, the generated X-ray is known as  $K_{\alpha}$  radiation. The X-ray is  $K_{\beta}$  if the electron is from the 3p orbital. The  $K_{\alpha}$  and  $K_{\beta}$  radiations can be easily separated because of their large difference in energy. However, by spin-orbital coupling,  $K_{\alpha}$  radiation is further split into  $K_{\alpha 1}$  and  $K_{\alpha 2}$  radiations from the 2p<sub>3/2</sub> and 2p<sub>1/2</sub> shells, respectively.

The crystallographic orientation of samples was determined by XRD (Bruker D8 Advance and Rigaku Smartlab), with a diffraction angle  $2\theta$  ranging from 10 to 80° and scan rate of 5°·min<sup>-1</sup>. On a silica substrate *ca.* 50 mg of sample was

placed and compressed to a well-packed bulk with a smooth surface of *ca.* 2 mm in thickness by a glass slide.

### 2.3.3 Ultraviolet-visible spectroscopy

Ultraviolet–visible spectroscopy (UV-vis) is the absorption spectroscopy or diffuse reflectance spectroscopy in the ultraviolet-visible spectral region (190–760 nm). It is a basic technique for analyzing optical property of semiconductor materials using a range of electromagnetic radiation from UV to visible region to scan a sample material. When the sample is excited electronically from its ground state, it absorbs light at a specific wavelength, showing a peak in the absorption spectrum. The band gap energy of semiconductor materials can be generally calculated from the UV-vis absorption spectrum using the Kubelka-Munk equation:

$$(\alpha h\nu) = A(h\nu - E_g)^n$$

where  $\alpha$  is the optical absorption coefficient of the material,  $h\nu$  is the energy of incident light, and the value of the  $n$  varies by the transition type of semiconductor; to exemplify,  $n = \frac{1}{2}$  is for direct transition,  $n = 2$  is for indirect transition. The band gap energy ( $E_g$ ) of semiconductor samples can be estimated by plotting  $(\alpha h\nu)$  against  $h\nu$ , by extrapolating the fitted straight line to the photon energy ( $h\nu$ ) axis in the plot, an intercept can be extracted to obtain the  $E_g$ .

For powder sample, the UV–vis absorption spectra were measured by a Cary 4000 UV-vis spectrophotometer in the scan range of 300–800 nm. For

nanomaterials dispersed in solution sample, the UV–vis absorption spectra were recorded on Hewlett Packard Model 8453 diode array UV-vis spectrophotometer with the scan range of 300–1100 nm.

#### 2.3.4 Scanning electron microscopy

Scanning electron microscope (SEM) is an electron microscopic technique that produces images by scanning the sample surface with a focused electrons beam. By the interaction of electrons with atoms in the sample, multiple signals can be produced that contains information about the sample surface topography and elemental composition. The electron beam scans in a raster scan pattern, and the beam position with the detected signal works in combination to produce images. The most commonly-used SEM mode is detection of secondary electrons emitted from atoms by electron beam excitation. The capacity of secondary electrons for the detection relies on the sample topography. Images of the sample surface topography can be produced by scanning the sample surface and collection of emitted secondary electrons using a detector.

Secondary electron imaging is generated by the emitting of secondary electrons near the sample surface. As a result, high-resolution images of a sample surface can be produced by SEM, revealing details down to 1 nm in size. Back-scattered electrons (BSEs) are beam electrons of high energy reflected from the sample by elastic scattering. The BSEs come from deeper locations of the sample and in turn the resolution of BSE images is lower than that of SEM images. However,

BSEs are often used in analytical SEM along with the spectra from X-rays, since the intensity of the BSE signal is strongly related to the atomic number ( $Z$ ) of the sample. Due to the narrow energy spread of electron beam, SEM images are of a large depth of field that produce a typical three-dimensional image useful for investigating the surface morphology of samples.

Samples for SEM imaging were prepared to resist the vacuum conditions and high-energy beam of electrons, and have the size that can fit on the sample stage. Samples are mounted rigidly and steadily to a sample holder or well-attached using a conductive adhesive.

### 2.3.5 Raman scattering spectroscopy

Raman scattering spectroscopy is a spectroscopic technique used to observe vibrational, rotational, and other low-frequency modes in sample system. Raman spectroscopy is a commonly-used measurement in material characterizations for the structural identification of molecules. For solid state materials, Raman spectroscopy as a non-destructive technique is usually used to study the lattice vibration properties, complementary to XRD. Generally, Raman spectroscopy can provide more reliable information about the symmetry and polarization configurations of a crystalline structure in materials.

The magnitude of the Raman effect is related to the polarizability of electrons in solid sample. Raman scattering is a form of inelastic light scattering, releasing a photon to excite solid samples. This excitation takes the molecule into a virtual energy state for a short period before emitting a photon. Besides, inelastic scattering denote that the energy of emitted photons is either lower or higher than that of incident photons. Samples after the scattering are of a different rotational or vibrational state. For the case of Stoke lines caused by inelastic scatterings ( $Q$ ), vibrational Raman spectroscopy requires the polarizability ( $\alpha$ ) to be non-zero during the vibration, i.e.

$$\frac{\delta\alpha}{\delta Q} \neq 0$$

The specific selection rules state that the allowed rotational transitions are,

$$\Delta J = \pm 2$$

where  $J$  is the rotational state.

Raman spectra were recorded on a Renishaw inVia spectrometer with a laser wavelength of 532 nm and coupled with a metallographic microscope. Before measurement, the Raman instrument was calibrated with silicon wafer, which has a characteristic scattering peak at  $520.4 \text{ cm}^{-1}$ .

### 2.3.6 X-ray photoelectron spectroscopy

X-ray photoelectron spectroscopy (XPS) is a forensic technique used for analyzing the surface composition, chemical state, and electronic state of

elements within a sample. When irradiated by X-rays, surface top atoms (1-10 nm depth of the sample) of a sample adsorb photons causing the ejection of core or valence electrons, which have a certain binding energy ( $E_b$ ) and kinetic energy ( $E_{kin}$ ). The number of photoelectrons escaping from a sample surface is collectively counted as a function of the  $E_{kin}$ , which is expressed in the  $E_b$  characteristic for one element

$$E_b = h\nu - E_{kin} - \phi$$

$\phi$  is the work function of the spectrometer (an arbitrary correction parameter unique to the instrument),  $h$  is Planck's constant,  $\nu$  is the frequency of excitation radiation. XPS measurement requires a high vacuum and is surface sensitive because enough energy is needed for the incident photons to penetrate the surface layers. Charge compensation for analysis was carried out using an electron energy of 8 eV and low energy Argon ions ( $Ar^+$ ) to prevent localized charging. The energy scale was calibrated to the  $E_b$  of C 1s (C-C, C-H) at 284.8 eV and was shifted by the photoelectron peak of metallic Cu, Ag, or Au, respectively.

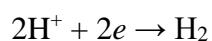
As each element has the unique electronic configuration and therefore orbital energies, the  $E_b$  recorded by XPS are based on a unique excitation from a specific energy level of a given element. The difference in binding environment in the sample, such as changes in adjacent atoms, can lead to changes of the  $E_b$  in the electrons. Further information on the surface chemical environment can be collected by studying the energy shift of one spectral line to others. As the oxidation state of an element changes, the extent of shielding effect of electron

also changes, causing either an upshift or downshift in the  $E_b$  of its electrons. The spectral shift provides evidence on the change in the electronic environment of an element, and the ratio of the element in such chemical state. Also, electron withdrawing or donating groups can influence the  $E_b$  of an atom in the sample. Coupling the electronic and chemical environment will provide a whole picture of surface information on nanomaterials.

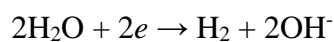
XPS results in this study were obtained using a K-Alpha X-ray photoelectron spectrometer (Thermo Fisher Scientific, UK) with a monochromatic Al K $\alpha$  X-ray source. High-resolution spectrum was obtained by using the monochromatic Al K $\alpha$  line with energy of 1486.6 eV. The pass energy was 160 and 40 eV for wide survey and high-resolution determination, respectively. About 10 mg of sample powder was pressed and attached to a carbon tape for measurement.

### 2.3.7 Electrochemical polarization

The electrocatalytic hydrogen evolution reaction (HER) is one of the most intensively studied electrochemical elementary reactions. The reaction of H<sub>2</sub> formation involves two electrons per H<sub>2</sub> molecule:

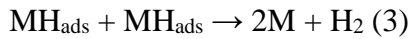
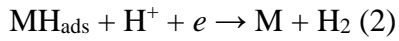
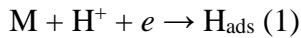


in acid solutions ( $E^\circ = 0 \text{ V (RHE)}$ ) and



in basic solutions ( $E^\circ = -0.8282 \text{ V (RHE)}$ ).

The H-H bonds formed and split in the reaction are of moderate strength, that is, moderate activation energies. The overall reaction rate is closely related to the energies of H<sub>2</sub>O molecule adsorption at the electrode surface site (M) and desorption of intermediate atomic hydrogen (H) by electron transfer. The HER occurs by a multi-step reaction and the generally accepted mechanism is described by the following steps:



where the initial discharge step (1), involving an adsorbed H intermediate (H<sub>ads</sub>) is followed by either the recombination of the H<sub>ads</sub> to form molecular H<sub>2</sub> (2) (Tafel reaction), or electrochemical desorption of H<sub>ads</sub> to form H<sub>2</sub> molecule (3), (Heyrovsky reaction). By the electrocatalytic properties of the electrode material, H<sub>2</sub> evolution proceeds in two alternative routes (1) + (2) or (1) + (3). In acidic solutions, H<sub>3</sub>O<sup>+</sup> ion is the proton source for the initial discharge step (1), while H<sub>2</sub>O is the proton source in basic solutions.

Mechanistic studies to explain the elementary steps of HER are generally based on the determination of kinetic parameters such as Tafel slope, reaction order for a specific electrode material. If the initial discharge (1) is the rate determining step, Tafel slope values of 120 mV are observed. Tafel slope is 40 mV if the reaction (2) is the rate determining step and if the chemical recombination (3) is

rate determining, the slope is 30 mV. When the H intermediate coverage ( $\theta_H$ ) on the electrode surface is high, a Tafel slope of 120 mV is expected if reaction (2) is rate determining. If reaction (3) is the rate determining step, a limiting current is expected. For materials with weakly binding H intermediate, the mechanism is governed by steps (1) + (2), with a Tafel slope of 120 mV, suggesting inactive electrode materials. A Tafel slope of 30 mV usually occurs with strongly binding intermediate, indicative of active electrode materials.

Electrochemical polarization was performed using a 1030A CHI electrochemical workstation. Catalyst (3 mg) and 5 wt% Nafion solution (20  $\mu\text{L}$ ) were dispersed in 2 mL water/ethanol (3:1 v/v) by 10 min sonication to form a homogeneous suspension. Then, 10  $\mu\text{L}$  of catalyst ink was drop-cast onto a glassy carbon electrode of 3 mm diameter (surface area = 0.07  $\text{cm}^2$ ) as the working electrode with a constant mass loading of 0.21  $\text{mg cm}^{-2}$ . A linear sweep voltammogram from 0 to  $-0.6$  V was measured at a scan rate of 1  $\text{mV s}^{-1}$  in 0.5 M  $\text{H}_2\text{SO}_4$  using a saturated calomel electrode and a Pt wire as the reference electrode and counter electrode, respectively.

### 2.3.8 Gas chromatography and hydrogen evolution measurements

Gas chromatography (GC) is a useful analytical technique for separation and identification of compounds that can be vaporized without decomposition. Depending on the boiling point, polarity, and adsorption ability of compounds

for analysis, the compounds can be separated efficiently by the interaction between the stationary phase and the sample-containing mobile phase with specific elution times. The mobile phase is a carrier gas, usually an inert gas such as helium (He) or an unreactive gas such as nitrogen (N<sub>2</sub>). The stationary phase is a microscopic layer of liquid or polymer on an inert solid support, inside a tube of glass or metal, called a column.

For photocatalytic hydrogen evolution experiments, 5 mg photocatalyst was dispersed in an aqueous solution (20 mL) containing sacrificial agent (such as Na<sub>2</sub>S (0.35 M) + Na<sub>2</sub>SO<sub>3</sub> (0.25 M) (aq), methanol/water) in a 50 mL round-bottom quartz flask, as shown in the schematic diagram Figure 2.1. After 20 min stirring, the solution was degassed by bubbling Argon (Ar) gas for 30 min, followed by continuous stirring and irradiated with a Newport solar simulator (Xenon lamp, ozone free, 150 W) of a light intensity 100 mW cm<sup>-2</sup>. The amount of H<sub>2</sub> gas evolved was measured by an Agilent 7890B GC system with a ValcoPLOT Molesieve 5Å PLOT column (CFS-X3053-500) using N<sub>2</sub> as carrier gas and thermal conductivity detector (TCD). The temperature of oven and detector was 40 and 280 °C, respectively.

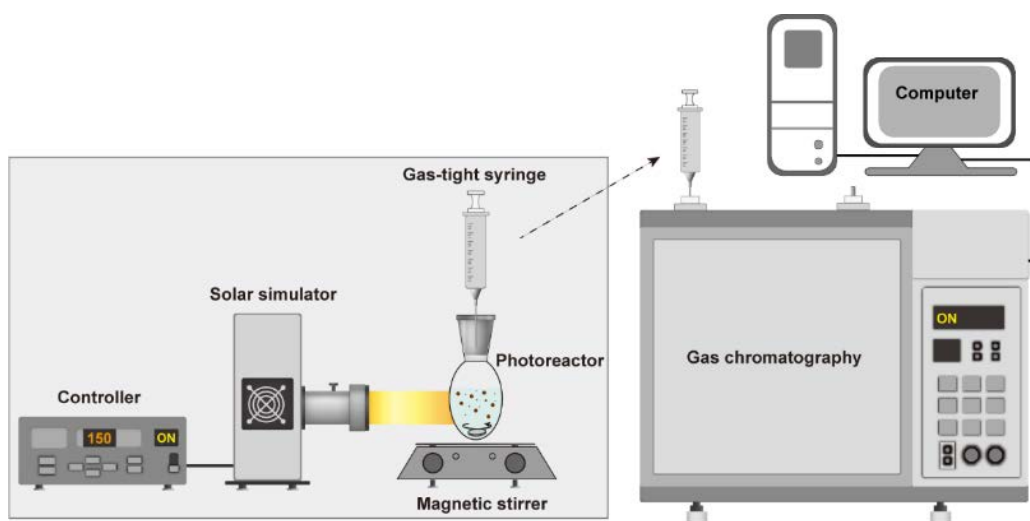


**Figure 2.1** Schematic photocatalytic hydrogen evolution setup. A 25 mL round-bottom quartz flask (photoreactor) containing 5 mg photocatalyst dispersed in aqueous sacrificial agent solution. A certain amount of H<sub>2</sub> evolved was taken by a gas-tight syringe for analysis on the nearby GC equipment.

## **Chapter 3**

### **ZnS Nanoparticles with Multiple Parallel Phase-junctions as Highly Active Photocatalyst for Water Reduction to Hydrogen**

### 3.1 Introduction

Semiconductors made of earth-abundant and low-toxic elements are most studied for photo-catalytic reactions, such as hydrogen generation from water<sup>140</sup> and photoreduction of CO<sub>2</sub>,<sup>141, 142</sup> and gaseous pollutants.<sup>143</sup> Over the past decade, several strategies including metal ion doping,<sup>144, 145</sup> vacancy creation<sup>146</sup> and heterojunctions construction by coupling with plasmonic metal<sup>147</sup> and/or low-bandgap semiconductor materials<sup>42, 148, 149</sup> have been used to push on the photocatalytic performance. Creating internal interface between two different crystal phases, has been documented to boost the photocatalytic activities on semiconductor photocatalysts such as Ga<sub>2</sub>O<sub>3</sub>,<sup>150</sup> ZnS,<sup>151</sup> and Cd<sub>1-x</sub>Zn<sub>x</sub>S.<sup>152</sup> The internal electrostatic field formed at these phase-junctions was associated with type-II staggered bandgap alignment that promotes the spatial separation and transfer of photogenerated charges.<sup>153, 154</sup> With various polymorphs available, the construction of such internal phase-junctions in metal sulfides can be an effective approach for tuning their band structure to better separate the charge carriers. Nevertheless, how to introduce these phase junctions into the semiconducting materials in a systematic and rational manner is still a big challenge.

In this chapter, a simple two-step method of constructing multiple internal phase junctions (MIPs) in ZnS nanoparticles is demonstrated, where sphalerite (Sp) and wurtzite (Wz) phases coexist as alternating parallel layers. The alternating MIPs have been reported to be highly desirable for the effective transfer and separation of charge due to new electronic states leading to the pinned Fermi level in the

energy gap.<sup>155-157</sup> The Fermi level difference at the parallel phase-junctions can act as a localized electric field that drives separation and directional migration of electron-hole pairs.<sup>152, 158</sup> The density of phase-junctions prepared by this two-step method is readily tunable and correlated to effective promotion of charge separation and transfer, thus contributed to a significant promotion on the photocatalytic hydrogen evolution reaction (HER) rate. The rational design of such parallel MIPs in photocatalysts presents a promising strategy for enhancing the photocatalytic activity without introducing any foreign, usually either toxic or rare, components as required by conventional heterojunctions.

## **3.2 Results and discussion**

### **3.2.1 Precursor ZnS(en)<sub>0.5</sub>**

#### **3.2.1.1 Powder X-ray diffraction**

ZnS-ethylenediamine (ZnS(en)<sub>0.5</sub>) was first prepared by solvothermal method as a precursor for ZnS nanocrystal. The X-ray diffraction (XRD) pattern of as-obtained ZnS(en)<sub>0.5</sub> (Figure 3.1) was indexed to orthorhombic structure, which agrees well with literature.<sup>159, 160</sup> The peak positions of the precursor are 10.28°, 20.56°, 22.49°, 24.88°, 24.92°, 27.90°, 28.80°, 29.27°, 31.46°, 33.15°, 34.17°, 35.77°, 37.19°, 41.81°, 43.73°, 47.58°, 48.87°, 53.02°, 53.56°, 58.97°, 60.13°, 62.88°, 66.76°, can be indexed to crystal planes (200), (210), (111), (211), (410), (020), (411), (102), (511), (221), (610), (611), (421), (711), (003), (430), (313), (10 0 0), (812), (532), (713), (831), (11 0 2), respectively.

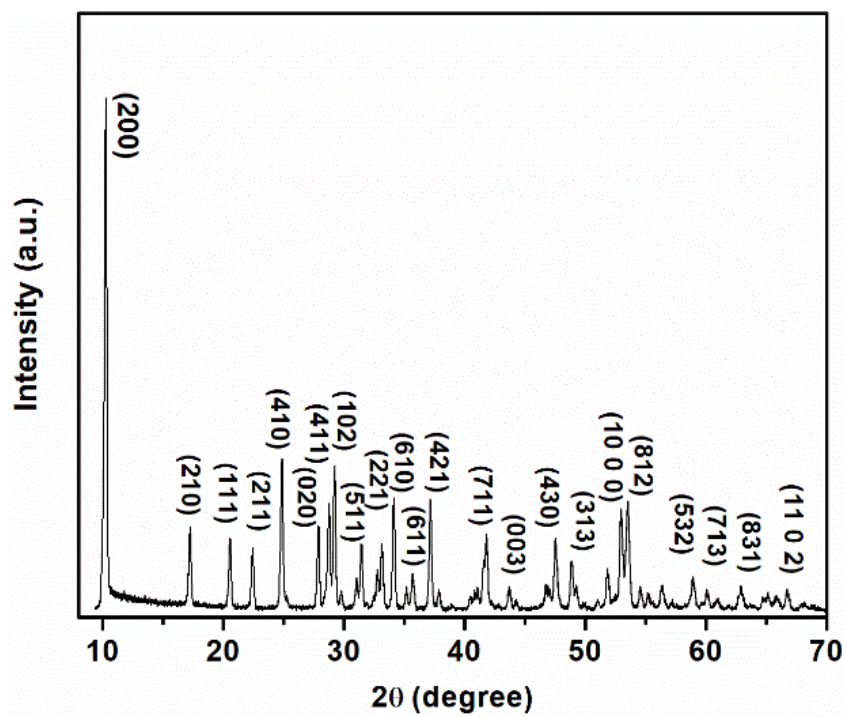


*Figure 3.1* XRD pattern of precursor ZnS(en)<sub>0.5</sub>.

### 3.2.1.2 Structure analysis

Scanning electron microscope (SEM) and transmission electron microscope (TEM) analyses (Figure 3.2b and c) show its plate-like morphology, which was further revealed to comprise numerous nanocrystals ( $d = 5.3 \pm 1.2$  nm) by high-resolution TEM (HR-TEM, Figure 3.3). As both sulfur source and protecting ligand, *L*-cysteine was used which coordinates with metal ions and forms stable complexes. Under the solvothermal conditions used, initially formed  $\text{Zn}^{2+}$ -cysteine complex gradually dissociates to  $\text{Zn}^{2+}$  and  $\text{S}^{2-}$  ions, stabilizing the nucleation and growth of  $\text{ZnS(en)}_{0.5}$ . The ethylenediamine intercalates between two ZnS layers, constructing a plate-like morphology by multiple stacking, as indicated by the sharp XRD peak at  $10.2^\circ$ .<sup>160, 161</sup>

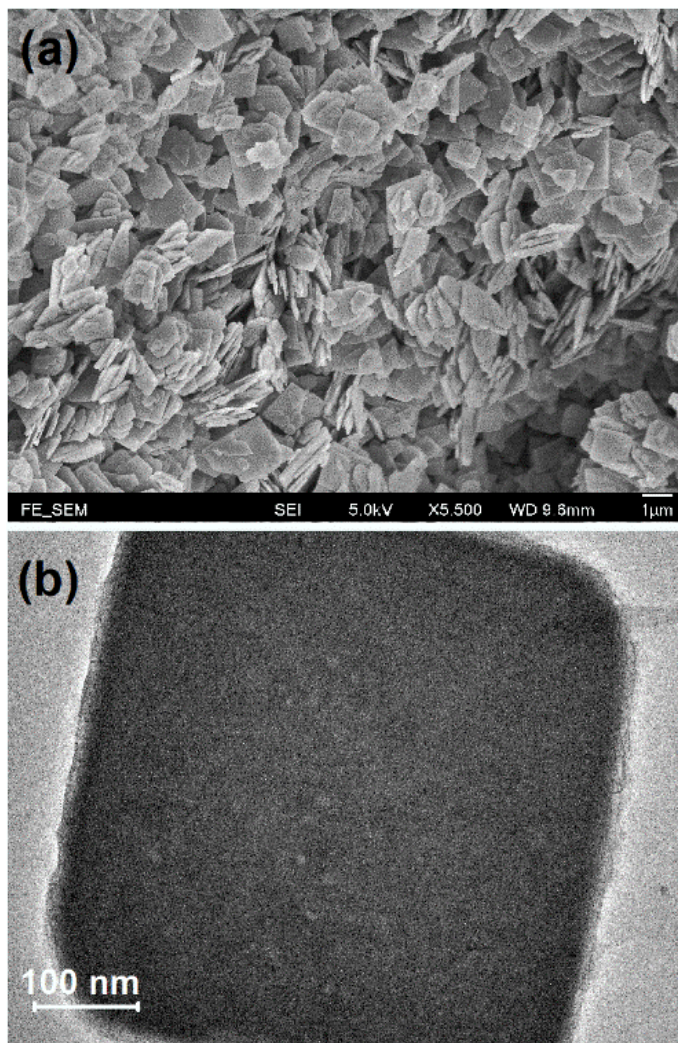


*Figure 3.2* (a) SEM and (b) TEM image of precursor  $\text{ZnS(en)}_{0.5}$ .

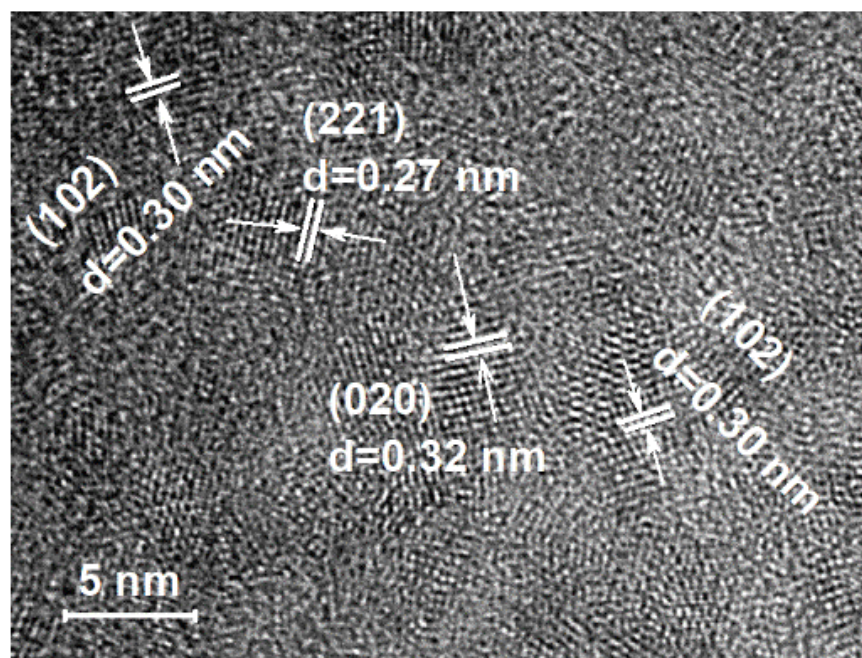


*Figure 3.3* TEM close-up image of precursor ZnS(en)<sub>0.5</sub>.

### 3.2.2 ZnS nanocrystal

#### 3.2.2.1 Transmission electron microscopy

ZnS(en)<sub>0.5</sub> was further treated at various temperatures (from 140 to 260 °C) under hydrothermal conditions, four ZnS nanocrystals were obtained at 140, 180, 220, and 260 °C, labeled as ZS-1, ZS-2, ZS-3, and ZS-4, respectively. Figure 3.4 compares the TEM images of the obtained ZnS nanocrystals. By hydrothermal treatment, decomposition of ZnS(en)<sub>0.5</sub> produced smaller and round-shaped ZnS nanocrystals. Depending on the hydrothermal temperature, *in situ* nucleation and atomic rearrangement lead to not only different shapes but also different crystal phases of ZnS.<sup>149, 162</sup> The size of ZnS nanocrystals show an increasing trend with hydrothermal temperature, ranging from 36.5 nm at 140 °C to 133.1 nm at 260 °C. The particle growth could be caused by the crystal ripening or aggregation process at higher temperatures.<sup>163</sup> Further, we observed stripe-like interfaces, the density of which generally increases with reaction temperature (Figure 3.5); the average interface length per particle increases from 1.5 nm for ZS-1 to a maximum of 7.4 nm for ZS-3 but decreases slightly to 5.2 nm for ZS-4. The increased density of interfaces can be arising from the extent of ethylenediamine removal from ZnS at elevated temperature, while further atomic rearrangement by crystal ripening at higher temperature (260 °C) could be responsible for the decrease in interface length for ZS-4.

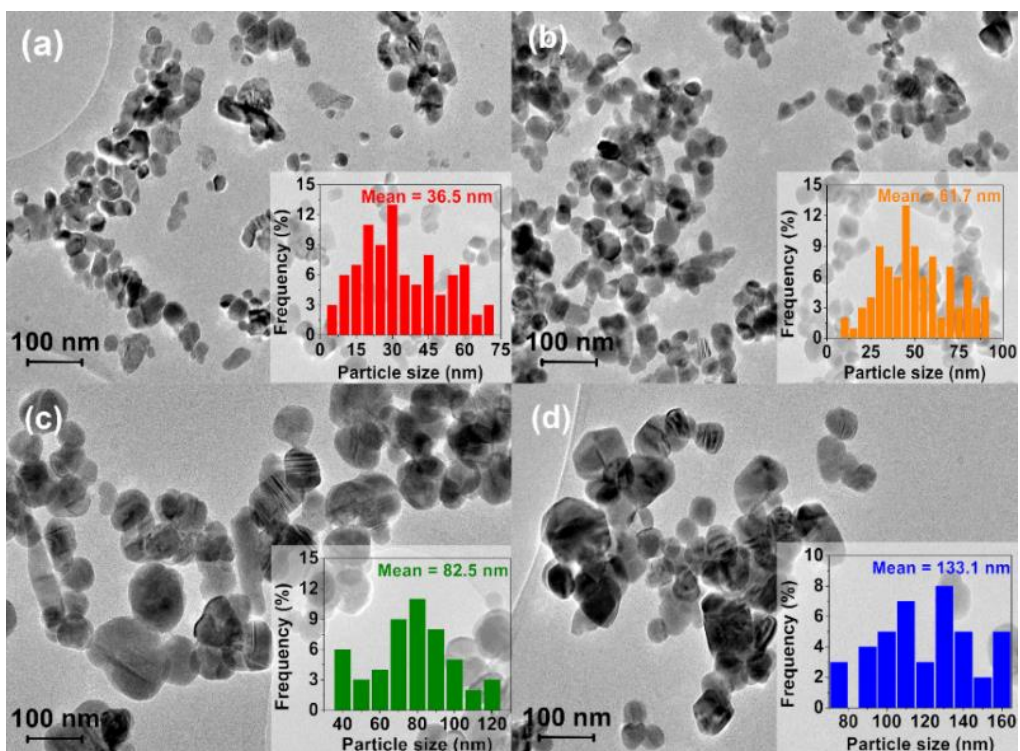


**Figure 3.4** Hydrothermally treated ZnS nanocrystals at different temperatures (a) 140 °C; (b) 180 °C; (c) 220 °C; (d) 260 °C. Insets show the size distribution.

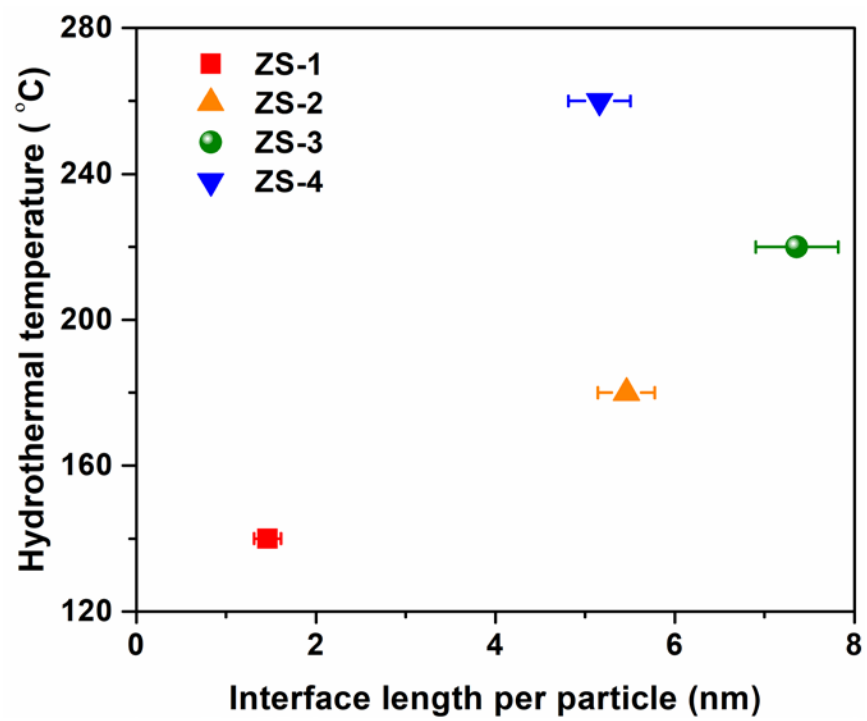


*Figure 3.5* Relationship between the hydrothermal reaction temperature and the density of internal phase-junctions observed in ZnS nanocrystals.

ZS-3 with maximum interface length per particle was investigated and shown in Figure 3.6 where dual crystal phases are clearly revealed by distinctive lattice fringes; the lattice spacings of 0.33 and 0.27 nm are ascribed to the (100) plane of wurtzite (Wz) phase and the (200) plane of sphalerite (Sp) phase, respectively. These Wz and Sp phases are periodically alternating, thus forming multiple parallel interfaces over most of nanocrystal surface. The associated fast Fourier transform (FFT) pattern also supports this polytype nature with organized Sp and Wz phases (inset in Figure 3.6(b)).<sup>164, 165</sup> We also observed a few twisted lattice fringes (indicated with arrow in Figure 3.6(b)) that constitute a sandwiched interface and may serve as a transitional state between the Sp-Wz heterophase. Such stripe-like MIPs may result from the atomic rearrangement as a transitional state between two crystalline phases, which have a mean surface energy difference of  $0.22 \text{ J m}^{-2}$ .<sup>151, 166</sup>

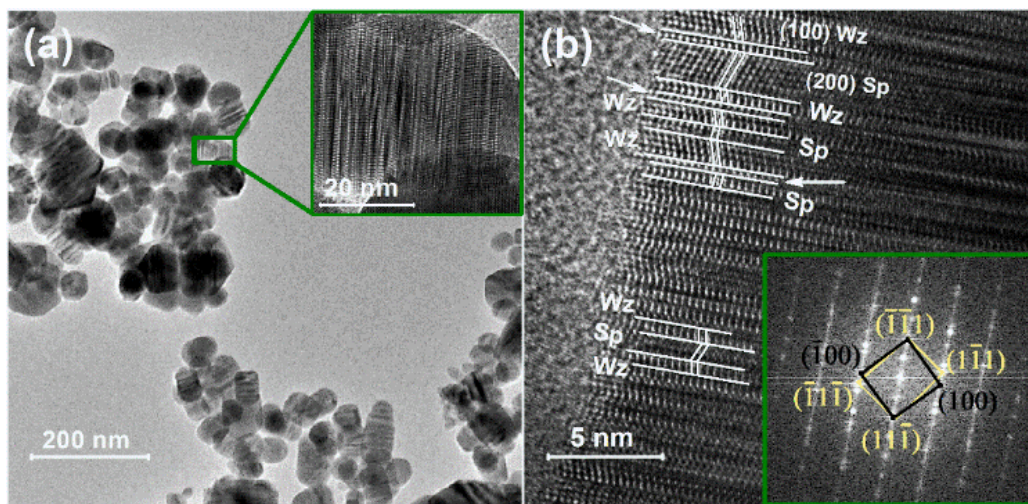


**Figure 3.6** (a) TEM image of ZS-3 ZnS nanocrystals. Inset is a close-up image of the region with MIPs. (b) HR-TEM image of ZS-3. The lines are the interfaces between Wz and Sp phases, and the arrows indicate sandwiched interfaces. Inset shows the fast Fourier transform (FFT) pattern.

### 3.2.2.2 Powder X-ray diffraction

To investigate the crystalline structure and phase composition, powder XRD was employed and the patterns are shown in Figure 3.7. ZS-1 shows a characteristic diffraction pattern indexed to hexagonal Wz phase ZnS (JCPDS No.36-1450) with a small peak at  $33.1^\circ$  suggesting the existence of Sp phase. It is noteworthy that thermodynamically metastable Wz phase was obtained in ZS-1 at  $140^\circ\text{C}$ , which is usually formed only at  $> 400^\circ\text{C}$ .<sup>167</sup> This could be related to the  $\text{Zn}^{2+}$ -cysteine complex that has been shown to have the favorable surface energy, thus stabilizes the formation of metastable Wz phase ZnS at low temperature.<sup>168</sup> The ZnS nanocrystals prepared at higher temperatures, ZS-2 and ZS-3, show similar XRD patterns as ZS-1. The relative intensity of peak at  $28.6^\circ$ , however, increased sharply, which can be ascribed to both (111) plane of Sp phase and (002) plane of Wz phase. Such acute increase in peak intensity, in contrast to its two neighbor peaks ( $26.9$  and  $30.5^\circ$ ), suggests the substantial contribution from Sp phase. The formation of MIP can create plenty of dangling bonds along the direction of (111) plane of Sp phase and (002) plane of Wz phase, which lead to new electronic states on the surface of ZnS nanocrystal.<sup>169</sup> In addition, the peaks at  $33.1$  and  $39.6^\circ$  also indicates the co-existence of Wz and Sp phases. The hydrothermal extraction of ethylenediamine from the  $\text{ZnS}(\text{en})_{0.5}$  by the strong solvation of water is believed to lead to the surface atomic rearrangement and the formation of dual phase.<sup>151, 170</sup> Meanwhile, ZS-4 exhibits decreased intensities from (111) and (200) planes of Sp-phase, which could result from the transformation of interface states at a high temperature.<sup>171</sup> It is evident that the reaction temperature

modulates the phase evolutions in ZnS nanocrystals and the growth of thermodynamically stable phase-junctions.

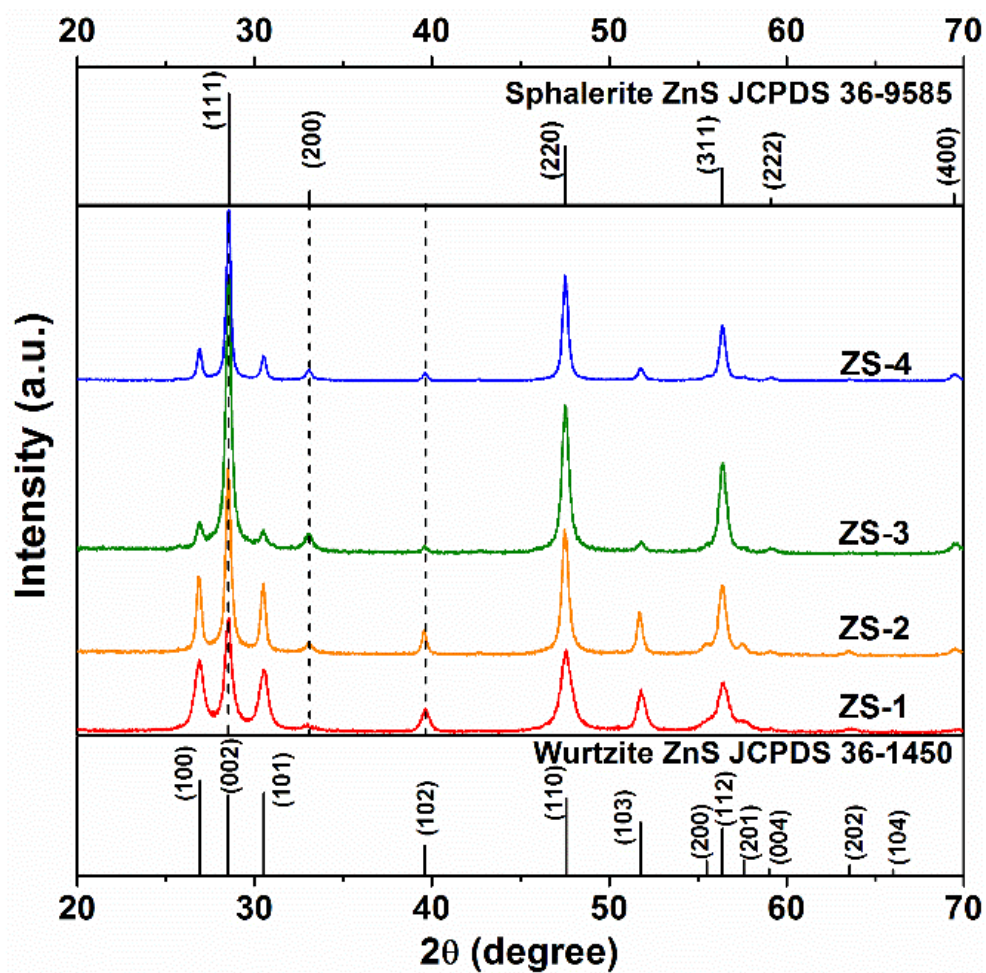


**Figure 3.7** XRD patterns of ZnS nanocrystals synthesized at various hydrothermal temperatures (ZS-1: 140 °C; ZS-2: 180 °C; ZS-3: 220 °C; ZS-4: 260 °C).

### 3.2.2.3 Raman Spectroscopy

The coexistence of Wz and Sp phases is also supported by the characteristic phonon modes in Raman spectroscopy (Figure 3.8). The broad band at  $218\text{ cm}^{-1}$  and bands at  $253\text{ cm}^{-1}$  ( $A_1, E_1$ ) and  $304\text{ cm}^{-1}$  ( $E_L^2$ ) can be assigned to the longitudinal acoustic overtone and polar modes observed in Wz phase of ZnS, respectively.<sup>172</sup> The longitudinal optical mode located at  $351\text{ cm}^{-1}$  ( $T_2$ ) is consistent with previous reports of the characteristic Sp phase in ZnS.<sup>173</sup> Notably, the band at  $267\text{ cm}^{-1}$  becomes prominent in ZS-3 and it merges with the band at  $253\text{ cm}^{-1}$  in ZS-4, which is a clear indication of the transverse optical mode of Sp phase ZnS.<sup>172</sup> In the high-frequency region ( $550 - 800\text{ cm}^{-1}$ ), the optical overtone and combinational bands at  $617, 642,$  and  $671\text{ cm}^{-1}$  are typical for Sp phase of ZnS (inset in Figure 3.8).<sup>174</sup>

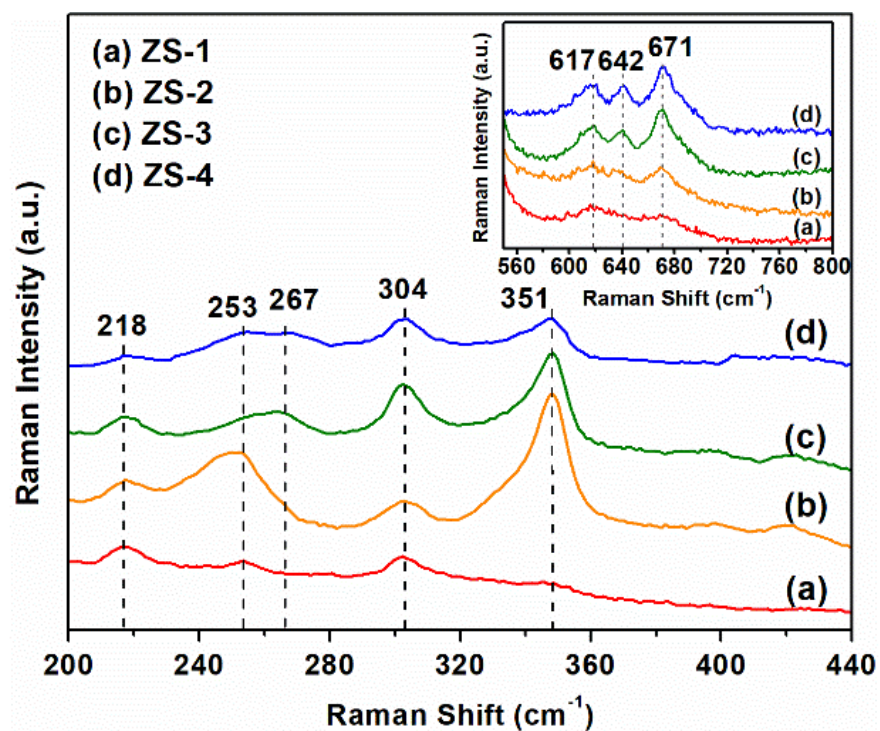


*Figure 3.8* Raman spectra of the ZnS nanocrystals with MIPs.

#### 3.2.2.4 X-ray photoelectron spectroscopy

The surface composition and chemical states of ZS-3 were examined by X-ray photoelectron spectroscopy (XPS) analysis. The XPS survey spectrum shown in Figure 3.9(a) identifies the presence of Zn and S on the surface with no other impurities. Contrary to the common ZnS 2p XPS spectrum where two single peaks corresponding to Zn 2p<sub>1/2</sub> and 2p<sub>3/2</sub> are observed, the Zn 2p HR-XPS spectrum of ZS-3 exhibits two split peaks corresponding to Zn 2p<sub>1/2</sub> and 2p<sub>3/2</sub>, suggesting different electronic environments for Zn atoms (Figure 3.9(b)). The major Zn 2p<sub>1/2</sub> and 2p<sub>3/2</sub> peaks with lower binding energies of 1044.5 and 1021.3 eV, respectively, can be related to the electron-rich Zn<sup>2+</sup> due to the Zn-Zn misalignment near MIPs, whereas the minor peaks with higher binding energies of 1045.9 and 1022.9 eV are due to surface Zn<sup>2+</sup> species with low-coordination number and stronger metallic character.<sup>161</sup> The different electronic environments of Zn species, which usually arise from the surface bonding faults or local surface disorder on surface, lead to splitting peaks.<sup>146</sup> At the engaged hydrothermal temperatures, the ethylenediamine molecules are released from the layer-structured precursor under kinetic control, which is believed to leave non-uniform surfaces that form the parallel interfaces between phases,<sup>175</sup> and thus cause the surface Zn-S bonding faults, leading to different chemical states of Zn and S.<sup>176, 177</sup> Meanwhile, two split peaks for S located at 161.8 and 160.4 eV are assigned to S 2p<sub>1/2</sub> and S 2p<sub>3/2</sub> (Figure 3.9(c)), which is consistent with the reported values.<sup>16, 178</sup>

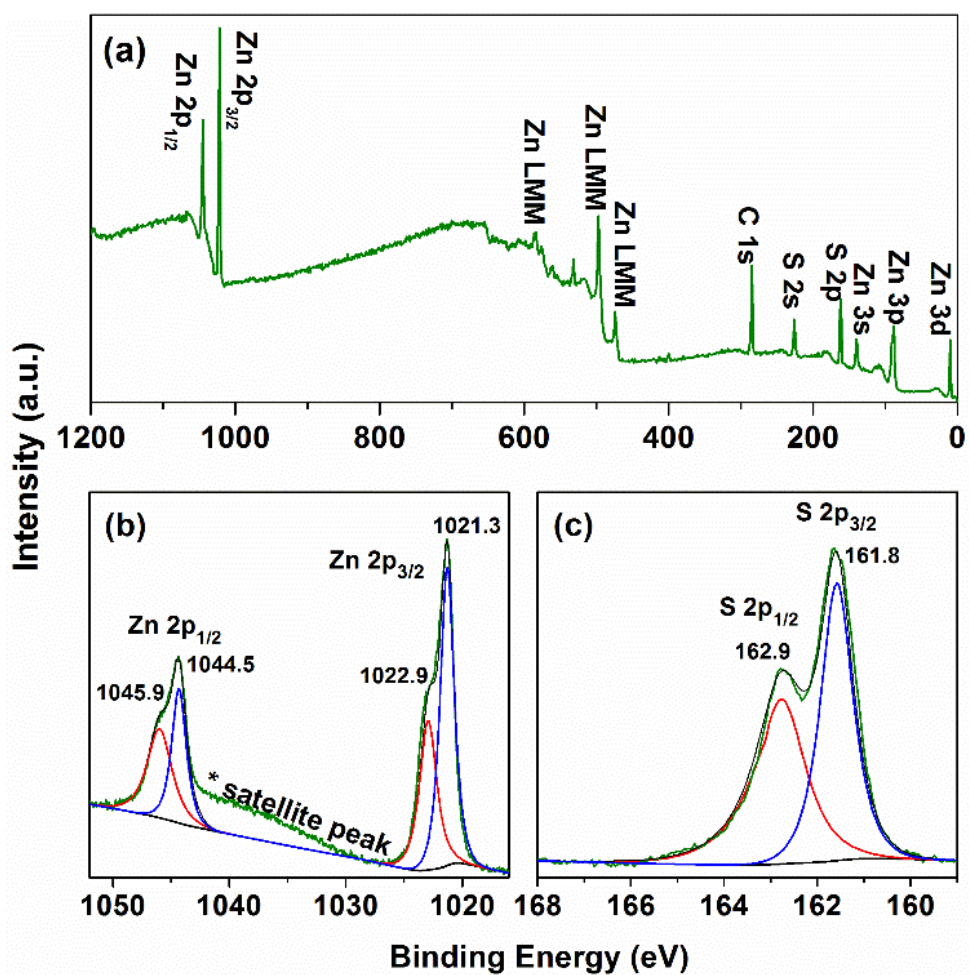


**Figure 3.9** (a) XPS survey spectra of ZS-3 and high-resolution XPS spectra of (b) Zn 2p and (c) S 2p.

### 3.2.2.5 Ultraviolet-visible spectroscopy and energy-gap calculation

The MIP, as a line of defects, can alter the physicochemical properties of nanocrystals by lowering the energy barriers at surface. We first studied the effects of MIPs on the optical properties of ZnS nanocrystals by UV-Vis diffuse reflectance spectroscopy. All four samples exhibit the absorption cut-offs at ~375 nm (Figure 3.10), which are red-shifted from that of the commercial ZnS (C-ZS, 343 nm). The corresponding bandgap energy ( $E_g$ ) calculated by the transformed Kubelka–Munk function and the Tauc plot (inset in Figure 3.10) yields the  $E_g$  of *ca.* 3.4 eV, slightly lower than that of C-ZS (3.6 eV). The narrowing bandgap is apparent in the spectra of ZS-1 and ZS-2 with broad absorption bands tailing off to 800 nm. Therefore, the formation of MIPs induces bond distortions that lead to localized electronic levels in the forbidden band gap.<sup>179</sup> ZS-3 and ZS-4, however, show only subtle changes in the visible range absorption, probably due to the increased local surface disorder.<sup>180</sup>

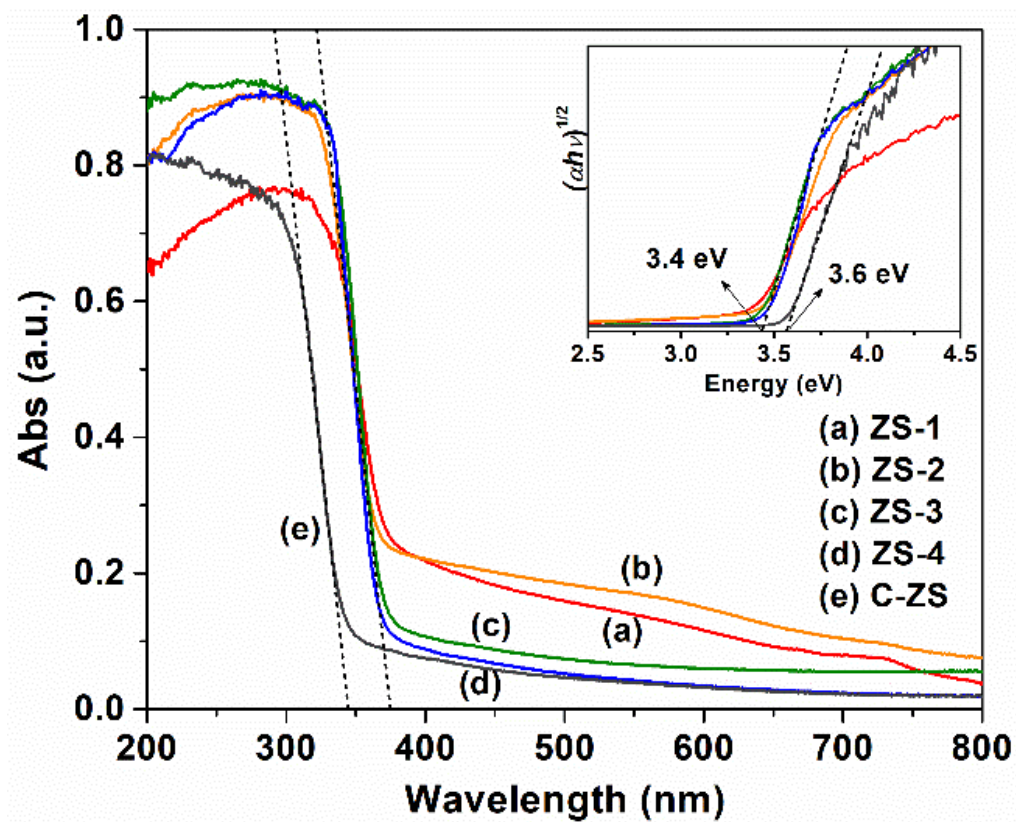


*Figure 3.10* UV-Vis diffuse reflectance spectra of ZnS nanocrystals with MIPs.

### 3.2.2.6 Photocatalytic hydrogen evolution

With modified atomic arrangements and optical properties, it is of great interest to find out how these aligned MIPs affect the photocatalytic activity of ZnS. The photocatalytic HER was carried out under simulated solar illumination using 0.35 M Na<sub>2</sub>S + 0.25 M Na<sub>2</sub>SO<sub>3</sub> solution as sacrificial agent and the results are summarized in Figure 3.11(a). The C-ZS showed poor photocatalytic HER rate of merely 0.10 mmol g<sup>-1</sup> h<sup>-1</sup>, which is expected for its limited light absorption and fast recombination of charge carriers.<sup>181</sup> On the contrary, all ZnS nanocrystals with MIPs show significantly enhanced HER rates. ZS-1 and ZS-2 generate H<sub>2</sub> at the rates of 0.32 and 0.71 mmol g<sup>-1</sup> h<sup>-1</sup>, which account for 320 and 710 % enhancement from C-ZS, respectively. The most MIP-rich ZS-3 shows an exceptionally high HER rate of 6.9 mmol g<sup>-1</sup> h<sup>-1</sup> with an apparent quantum efficiency (AQE) of 36.8 %. More importantly, such high HER rate was achieved without the assistance of any co-catalyst or support. As suggested by TEM images, the enhanced photocatalytic activity of ZS-3 is associated with the highest density of alternating Sp-Wz interfaces, which may form ordered type-II energy band alignments to effectively drive the spatial separation of photogenerated charge carriers.<sup>182, 183</sup> Such parallel interfaces are known to eliminate the charge recombination centers and facilitate the transport of charge carriers. Moreover, the MIPs along (111) plane of Sp phase and (002) plane of Wz phase possess a lower potential barrier, which would help charge localization and migration out by a tunneling process to the surface for H<sub>2</sub> generation.<sup>184</sup>

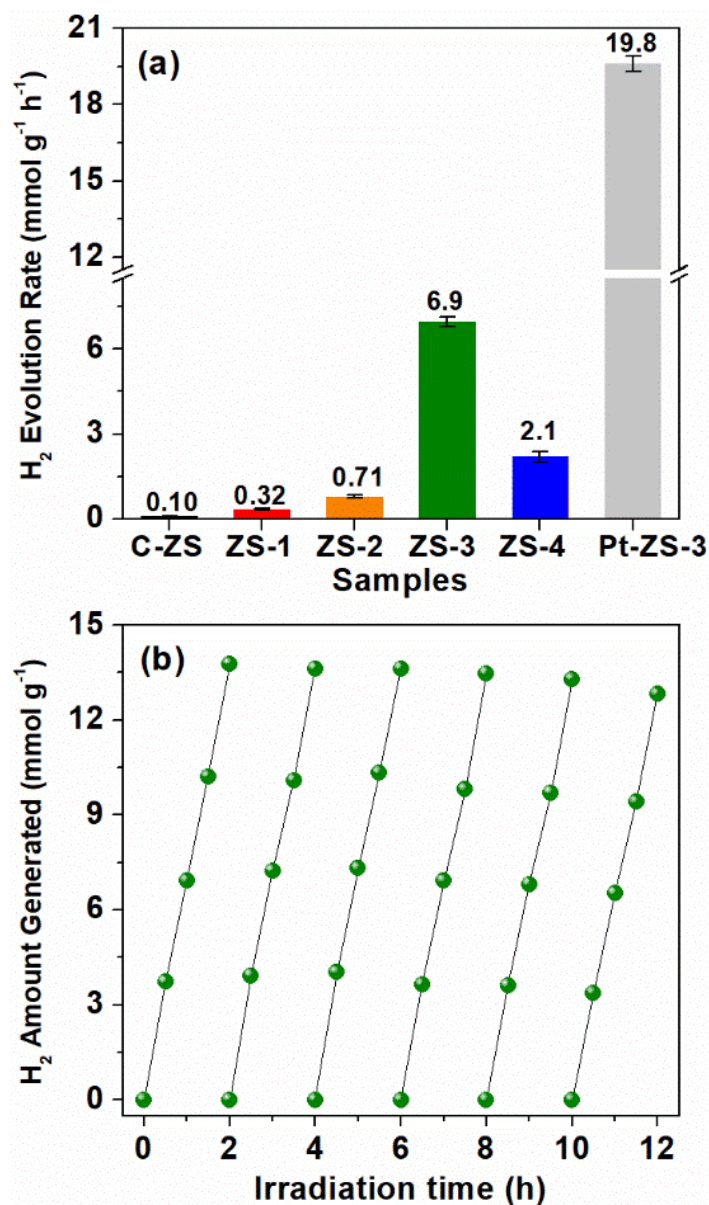


**Figure 3.11** (a) Photocatalytic hydrogen generation rates of ZnS nanocrystals prepared at various hydrothermal temperatures (ZS-1 to ZS-4). Commercial ZnS nanocrystal (C-ZS) and Pt nanoparticle decorated ZS-3 (Pt/ZS-3) are shown for comparison. (b) Stability test for photocatalytic cycles of ZS-3. All measurements were carried out with a 100 mW cm<sup>-2</sup> solar simulator.

To shed light on the active sites, we carried out the photo-reduction of metal ions on ZS-3.  $\text{H}_2\text{PtCl}_6$  was selected as a metal salt based on the lower Fermi level of Pt, compared with other noble metals, to trap electrons from the surface of ZS-3. The electrons were released for  $\text{H}_2$  evolution due to the lowest activation energy of Pt.<sup>101</sup> With 0.3 wt% Pt nanoparticles loaded, the photocatalytic HER rate of ZS-3 was further boosted to  $19.8 \text{ mmol g}^{-1} \text{ h}^{-1}$ , a 2.8-fold enhancement from the bare ZS-3 and nearly 200 times higher than C-ZS. To our knowledge, this is among the highest HER rates of metal sulfide-based photocatalysts reported up to date. The photocatalytic performance of ZS-4 is, however, substantially lower ( $2.1 \text{ mmol g}^{-1} \text{ h}^{-1}$ ) than that of ZS-3, presumably due to the collective effects of increased particle size and decreased MIP density. The HER activity of studied samples correlates well with the average interface length. In a continuous 10 h reaction to test long term photo-stability, no significant loss of activity was observed (Figure 3.11(b)), and the subsequent TEM analysis confirmed no structural changes nor aggregation occurred during HER, both of which demonstrate good stability of ZS-3.

#### 3.2.2.7 Electrochemical polarization curve

In addition to photocatalysis, a parallel investigation of electrocatalytic properties can provide more information on the proton adsorption for  $\text{H}_2$  formation at ZnS nanocrystal surface. The ZnS nanocrystals were drop-cast onto the glassy carbon electrode (GCE) with 5 wt% Nafion (Figure 3.12) and used as the working electrode in a typical three-electrode setup.

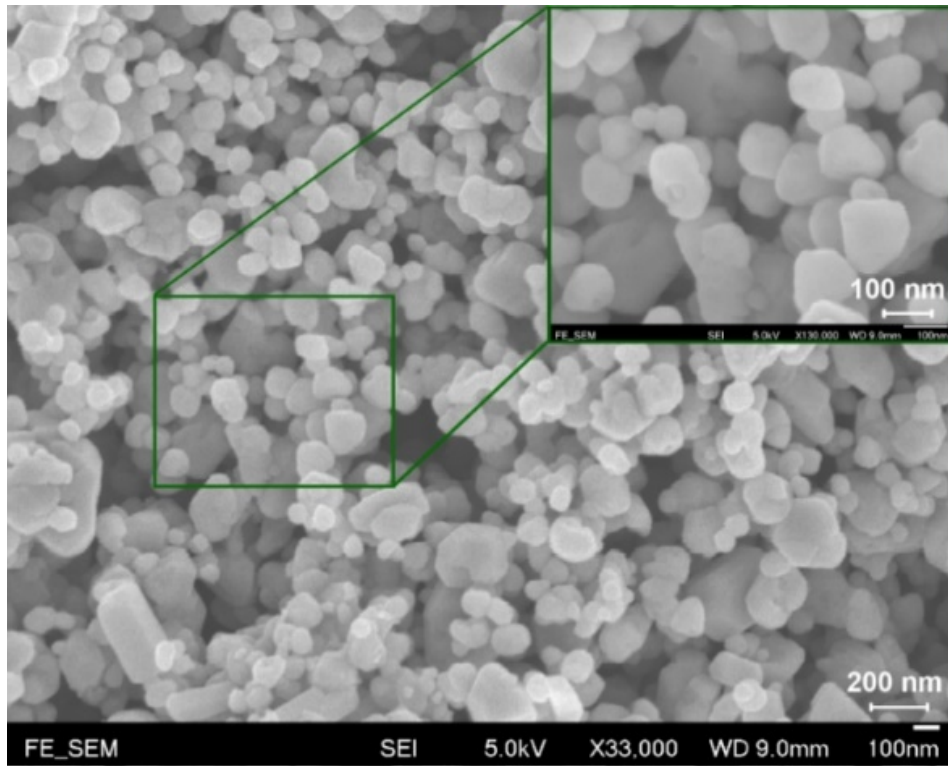


**Figure 3.12** SEM image of ZS-3 nanocrystals drop-cast onto the electrode surface.

Figure 3.13 compares the HER polarization curves of ZnS samples, C-ZS, and Pt on graphitized carbon (20 wt% Pt/C) measured in 0.5 M H<sub>2</sub>SO<sub>4</sub> at a scan rate of 1 mV s<sup>-1</sup>. In the studied potential range (50 to -550 mV), C-ZS shows the lowest electrocatalytic activity with an onset potential of -370 mV (*vs.* RHE). By contrast, all ZnS samples with MIPs show considerable improvements in electrocatalytic performances, as summarized in Table 3.1.

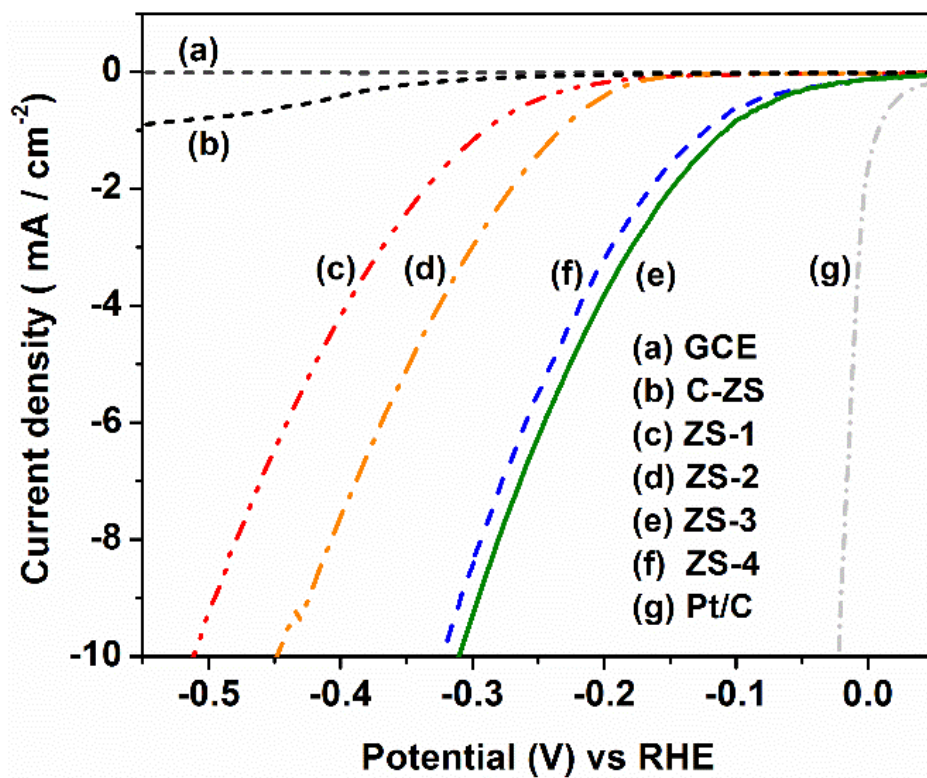


**Figure 3.13** Polarization curves of ZnS samples for HER. ZnS samples are compared with bare GCE, commercial ZnS (C-ZS), and 20 wt% Pt on graphitized carbon (Pt/C).

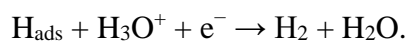
**Table 3.1** Summary of electrocatalytic performances of ZnS samples and Pt/C for hydrogen evolution.

<b>Electrocatalyst</b>	<b>Onset potential (mV vs. RHE)</b>	<b>Tafel Slope (mV/dec)</b>
ZS-1	-264	230
ZS-2	-212	219
ZS-3	-101	200
ZS-4	-122	204
C-ZS	-367	416
20% Pt/C	-3	33

ZS-3 exhibits the best electrocatalytic properties with a current density of  $-9.3 \text{ mA cm}^{-2}$  at  $-0.3 \text{ V}$  and an onset potential of  $-100 \text{ mV}$ , which accounts  $\sim 270 \text{ mV}$  improvement in overpotential and *ca.* 70-fold increase in current density from C-ZS. It is noteworthy that the electrocatalytic performance of ZnS nanocrystals is consistent with their photocatalytic activities and can be further correlated to the phase-junctions on the surface.<sup>185</sup> In general, the current density increases and the corresponding onset potential decreases with the MIP density. This trend is also noted from the Tafel plot (Figure 3.14) where the slope of the curve reflects the activity of catalytic reaction. It clearly suggests that the MIP formation on ZnS significantly benefits the catalytic performance for HER by promoting surface charge transport and enriching the localized electron density.<sup>101, 186</sup> In electrocatalytic HER, protons from the medium are first adsorbed onto the ZnS surface and form adsorbed species ( $\text{H}_{\text{ads}}$ ), which is known as Volmer reaction:



The electrons driven by applied potential reduce the  $\text{H}_{\text{ads}}$  into  $\text{H}_2$  through an electrochemical desorption step (Heyrovsky reaction):



As the MIPs are suggested to facilitate the charge transport, the desorption step occurs at lower overpotentials. Moreover, the increased current density of MIP-rich ZnS indicates lower resistivity to conduction electrons and expanded capacity for  $\text{H}^+$  adsorption on the surface.<sup>189, 190</sup>

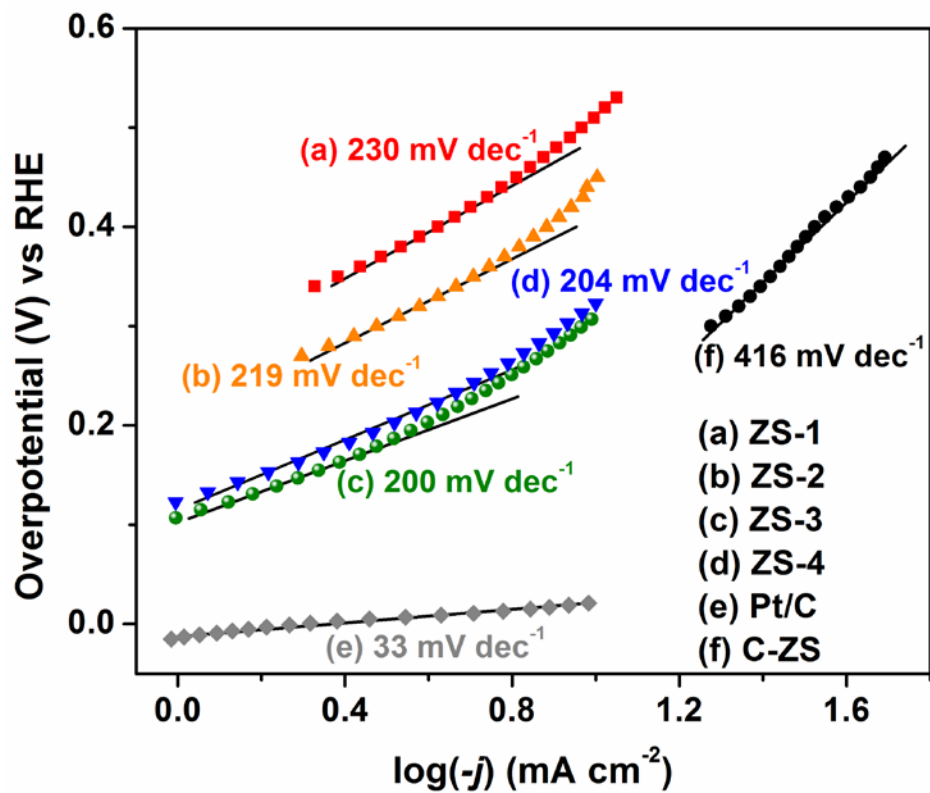


**Figure 3.14** Tafel plots of HER polarization curves measured in 0.5 M  $\text{H}_2\text{SO}_4$  at a scan rate of  $1 \text{ mV s}^{-1}$  using ZnS nanocrystals, commercial ZnS (C-ZS), and Pt on graphitized carbon (Pt/C) as the working electrode.

### 3.3 Concluding remarks

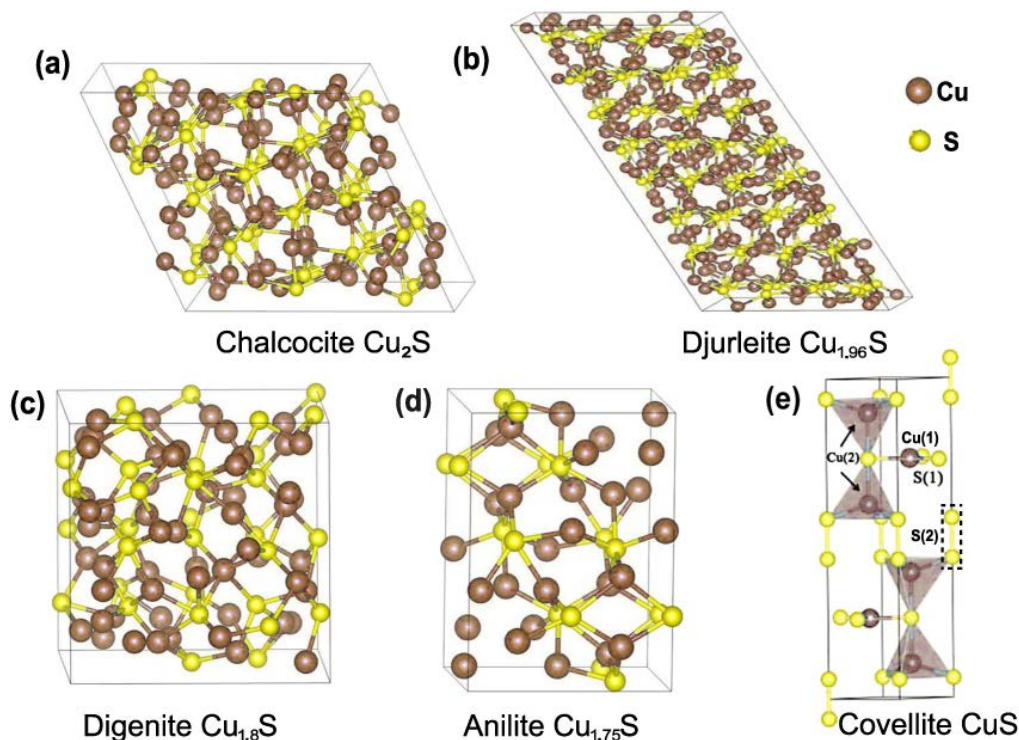
Multiple internal interfaces of alternating Wz and Sp phases are constructed on ZnS nanocrystals by a simple two-step method. The size and dominating phase of ZnS nanocrystals as well as the density of phase-junction are readily tunable. The existence of aligned Wz/Sp interfaces effectively facilitates the charge carrier separation and photoelectron localization for surface reaction, hence remarkably promotes photocatalytic HER rate of ZnS to  $6.9 \text{ mmol g}^{-1} \text{ h}^{-1}$ , almost two-orders of magnitude enhancement from normal ZnS. The electrocatalytic HER results also indicate the facilitated charge transport and easier proton adsorption and  $\text{H}_2$  desorption in the phase-junction-rich ZnS nanocrystals. This work demonstrates that internal interface engineering can be an effective strategy to realize highly-efficient co-catalyst-free photocatalytic  $\text{H}_2$  gas evolution from water.

## **Chapter 4**

### **Ethylenediamine-modulated Synthesis of Copper Sulfides and Their Photocatalytic Activities for Water Reduction to Hydrogen**

## 4.1 Introduction

Nanostructured copper sulfides are an interesting class of materials that have received wide research attention because of their great physicochemical properties available in multiple stable crystal phases.<sup>191</sup> The expanding developments in the materials introduce a systematic physicochemical engineering by varying element composition, valence states, nanocrystal morphologies and shapes. It has been revealed that the elemental composition and distribution can alter the electronic and optical properties of copper sulfides materials.<sup>192</sup> Even the simplest binary compounds,  $\text{Cu}_x\text{S}$  ( $1 \leq x \leq 2$ ), can readily form a series of derivatives with a band gap range of 1.2–2.4 eV because of the 3d electrons of copper.<sup>193</sup> Different Cu vacancies in  $\text{Cu}_x\text{S}$  derive several polymorphs such as covellite  $\text{CuS}$ , anilite  $\text{Cu}_{1.75}\text{S}$ , digenite  $\text{Cu}_{1.8}\text{S}$ , djurleite  $\text{Cu}_{1.96}\text{S}$ , and chalcocite  $\text{Cu}_2\text{S}$  (shown in Scheme 1), with crystal structures varying from monoclinic, orthogonal to hexagonal.<sup>194-196</sup> To date, up to twenty kinds of copper sulfides-based materials have also been reported on their potential applications in many fields, such as in photothermal conversion<sup>197</sup>, solar cell devices<sup>198</sup>, microwave shielding<sup>199</sup>, lithium ion batteries<sup>200, 201</sup> and photocatalysis<sup>29, 202</sup>



**Scheme 1** Crystal structures of (a) low-chalcocite  $\text{Cu}_2\text{S}$ , (b) djurleite  $\text{Cu}_{1.96}\text{S}$ , (c) digenite  $\text{Cu}_{1.8}\text{S}$ , (d) anilite  $\text{Cu}_{1.75}\text{S}$ , (e) covellite  $\text{CuS}$ ; adapted with permissions from ref 5 and 6. Copyright American Institute of Physics (AIP) publishing group and Copyright American Chemical Society (ACS) publishing group.

However, there remains a challenge to develop simple synthetic methods to prepare  $\text{Cu}_x\text{S}$  nanocrystals with novel nanostructures. Fortunately, the wide availability of copper and sulfide sources, combined with a relatively low nucleation and growth temperature in reaction medium, makes stabilization in  $\text{Cu}_x\text{S}$  nanocrystal achievable. A successful synthetic strategy has been developed from a fundamental understanding and classification of Cu species and sulfur ligands with molecular structure, which allows for experiment design to alter their nucleation and growth process.<sup>203</sup> This also has enabled a controlled

synthesis to define the size, shape, crystal structure, and composition of  $\text{Cu}_x\text{S}$  nanocrystals. With the need to define the crystal structure and composition, using bottom-up methods such as hydrothermal reaction offers a rapid and controllable synthetic approach to prepare well-defined nanocrystals.<sup>204</sup>

The common aspect in all approaches used for hydrothermal nucleation and growth of semiconductor nanocrystals in solution, is the use of coordinating reagents (or surfactants), although the binding behavior for crystal permit size and shape formation is different. The defined morphology requires a balanced combination of synthetic factors, including the choice of precursors and reaction medium, reaction temperature, ligand functions and combination.<sup>205</sup> These factors have been proven to affect the collective properties of semiconductor nanocrystals, arising from the need for applications.

Herein, we focus on the composition manipulation of  $\text{Cu}_x\text{S}$  nanomaterials by synthesizing four kinds of  $\text{Cu}_x\text{S}$  ( $x=1, 1.8, 1.75, 2$ ) nanocrystals using hydrothermal method. On this basis, multiple phase-junctions are designed and fabricated on  $\text{Cu}_x\text{S}$  and found to have active surface, thus resulting in a heterostructure with new electronic states. The active surface can lower down the energy barrier for reaction, with a great potential for improving the activity of  $\text{Cu}_x\text{S}$  for photochemical reactions. As a model reaction, photocatalytic

hydrogen evolution reaction (HER) is used to measure and compare the photocatalytic performances of the prepared  $\text{Cu}_x\text{S}$  nanocrystals.

## 4.2 Results and discussion

### 4.2.1 $\text{Cu}_x\text{S}$ ( $x=1, 1.75, 1.80, 2$ ) nanocrystals

#### 4.2.1.1 Powder X-ray diffraction

Hydrothermal synthesis was used to synthesize  $\text{Cu}_x\text{S}$  nanoparticles. In a typical reaction, equal molar *L*-cysteine and  $\text{Cu}(\text{oleate})_2$  was mixed in the binary solvents containing a certain volume of ethylenediamine in water and followed by hydrothermal reaction. Although the same experimental conditions were carried out in preparing  $\text{Cu}_x\text{S}$  ( $1 \leq x \leq 2$ ) nanocrystals, different crystal structures and phase compositions were expected in the products. Powder XRD was employed and the patterns are shown for comparison in Figure 4.1.

Ethylenediamine (en) is often used as a reaction medium for hydrothermal synthesis of well-defined semiconductor nanocrystals, arising from the high polarity, strong chelating ability and reducing power of en.<sup>206, 207</sup> An important role of using en has been found in controlling different crystal phases of semiconductor nanocrystals in synthetic process.<sup>8, 129, 151</sup> Thus, a series of experiments using controlled concentration of en moiety were done to study the

formation mechanism of  $\text{Cu}_x\text{S}$ . And the product prepared without using en was also investigated for comparison.

Firstly, the product prepared without using en can be assigned exclusively to the hexagonal CuS (JCPDS 06-0464, space group:  $P63/mmc$  (194)). The weak and wide diffraction peaks indicate the poor crystallization of the as-obtained product. When 20 vol% en moiety was introduced to the reaction medium, the as-obtained product shows that the diffraction pattern is well matched with the hexagonal  $\text{Cu}_{1.8}\text{S}$  (JCPDS 47-1748, space group:  $R3m$  (166)) and no impurities could be detected from the spectra. Further increased en ratio to 50 vol%, phase-pure monoclinic  $\text{Cu}_{1.75}\text{S}$  (JCPDS 23-0958, space group:  $C2/m(12)$ ) was successfully synthesized. However, when the en moiety was only used as the solvent, hexagonal  $\text{Cu}_2\text{S}$  (JCPDS 26-1116, space group:  $P63/mmc(194)$ ) was obtained. The widened diffraction peaks in the diffraction pattern suggest that the obtained products are in nanocrystalline nature. It may be concluded that the en used in the hydrothermal synthesis enables the reduction of some  $\text{Cu}^{2+}$  to  $\text{Cu}^+$ , thus the formation of different stoichiometric copper sulfides can be controlled by adjusting the ratio of en moiety while maintaining other conditions. The obtained  $\text{Cu}_x\text{S}$  nanocrystals with different stoichiometries are labeled as CS-1, CS-2, CS-3, CS-4, respectively.

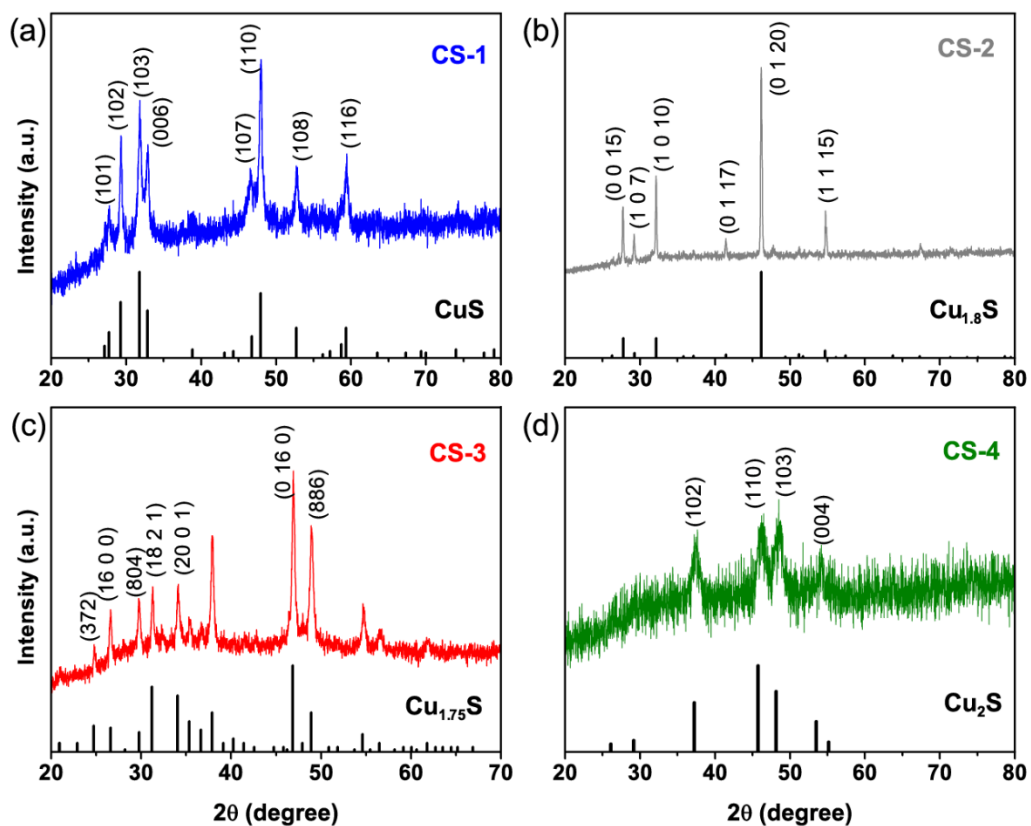


**Figure 4.1** Powder XRD pattern of (a) CS-1, (b) CS-2, (c) CS-3, and (d) CS-4. The standard JCPDS XRD pattern of hexagonal  $\text{CuS}$ , hexagonal  $\text{Cu}_{1.8}\text{S}$ , monoclinic  $\text{Cu}_{1.75}\text{S}$ , and hexagonal  $\text{Cu}_2\text{S}$  are shown for comparison.

#### 4.2.1.2 Transmission electron microscopy

The structures of as-obtained  $\text{Cu}_x\text{S}$  crystals were studied by transmission electron microscopy (TEM) as shown in Figure 4.2. From the low-resolution TEM images, CS-1 shows a hexagon-like shape particle with an average diameter of  $131 \pm 23.7$  nm, while CS-2 shows nearly monodispersed spherical shapes with an average diameter of  $122 \pm 8.3$  nm. However, CS-3 and CS-4 has wider size distributions with irregular shapes. The obtained  $\text{Cu}_x\text{S}$  with different stoichiometries show alterations in size and morphology, which can be related to the concentration of en moiety as a typical bidentate ligand for its coordination with metal cations. The size distributions of the resulting nanoparticles (NPs) are summarized Table 4.1. The median/standard deviation (Median/SD) ratio was used to evaluate the degree of mono-dispersity of the resulting NPs. NPs with high mono-dispersity have also higher value of Median/SD ratio. The result reveals that the en moiety plays an important role in the synthesis of  $\text{Cu}_x\text{S}$  NPs and generally two aspects can be considered. Firstly, en is a strong base medium and different concentrations can change the pH value in the reaction environment, which will affect the rate of reaction and the sizes of final  $\text{Cu}_x\text{S}$  NP. On the other hand,  $\text{Cu}^{2+}$  ion can be coordinated with en moiety to form stable  $[\text{Cu}(\text{en})_2]^{2+}$  complexes, which could work as a molecular template in the formation of  $\text{Cu}_x\text{S}$  NP into various morphologies.<sup>208, 209</sup> As a result, this bidentate ligand complex shows its capabilities of controlling the growth and directing the structure for the  $\text{Cu}_x\text{S}$  NPs.

Close-up view of the  $\text{Cu}_x\text{S}$  NPs were taken by high-resolution transmission electron microscopy (HR-TEM). The HR-TEM images are shown in Figure 4.2 which indicated that all  $\text{Cu}_x\text{S}$  NPs are well-crystallized with clear lattice  $d$ -spacing. For CS-1, a  $d$ -spacing of 0.31 nm from crystal plane (1 0 2) was measured from the lateral crystal fringe, indicating the growth along the (0 0 1) direction. CS-2 shows a clear  $d$ -spacing of 0.34 nm which is ascribed to the (1 0 1) crystal plane. CS-3 and CS-4 show a clear  $d$ -spacing of 0.19 nm and 0.33 nm, assigned to the (0 16 0) and (0 0 2) crystal planes, respectively. The observation from HR-TEM further confirms the crystalline nature of obtained copper sulfides.

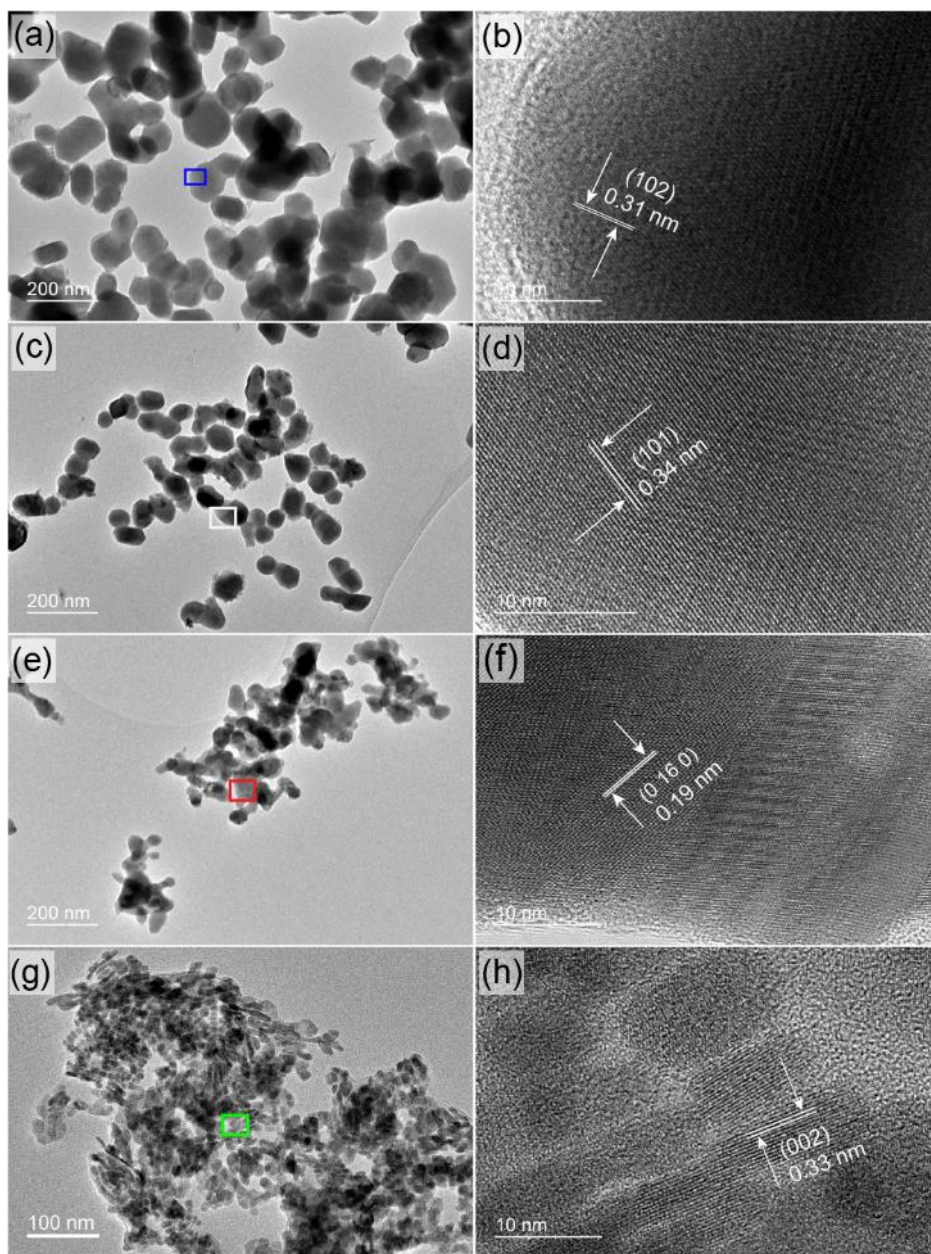


**Figure 4.2** TEM images of (a) CS-1, (c) CS-2, (e) CS-3, and (g) CS-4; and HR-TEM images of selected areas from (a), (b), (c), and (d), with lattice  $d$ -spacings in (b), (d), (f), (h) respectively.

**Table 4.1** Size summary of Cu<sub>x</sub>S (x=1, 1.8, 1.75, 2) NPs from TEM analysis.

Sample	Mean (nm)	Median (nm)	SD* (nm)	Median/SD
CS-1	131.1	124.1	23.7	5.24
CS-2	62.3	61.4	9.6	6.39
CS-3	42.3	42.6	13.3	3.21
CS-4	L:10.7	12.4	2.1	5.93

\* Standard deviation

#### 4.2.1.3 Energy dispersive X-ray spectroscopy

Energies of X-rays are characteristic of the difference in the energy between two discrete electron shells bound to nucleus, and the atomic structure of emitting elements. With this principle, the energy dispersive X-ray spectroscopy (EDS) can be used for measuring elemental composition of samples. The EDS measurement was taken to determine the average compositions of as-synthesized  $\text{Cu}_x\text{S}$  NPs, the maps of detected elements are shown in Figure 4.3. By measuring the atomic weight (Table 4.2), CS-1 was determined to be  $\text{Cu}_{1.19}\text{S}$ , CS-2 was determined as  $\text{Cu}_{1.81}\text{S}$ , CS-3 was  $\text{Cu}_{1.69}\text{S}$ , and CS-4 was  $\text{Cu}_{1.96}\text{S}$ , all of which are close to the theoretical stoichiometries and in accordance to XRD results.

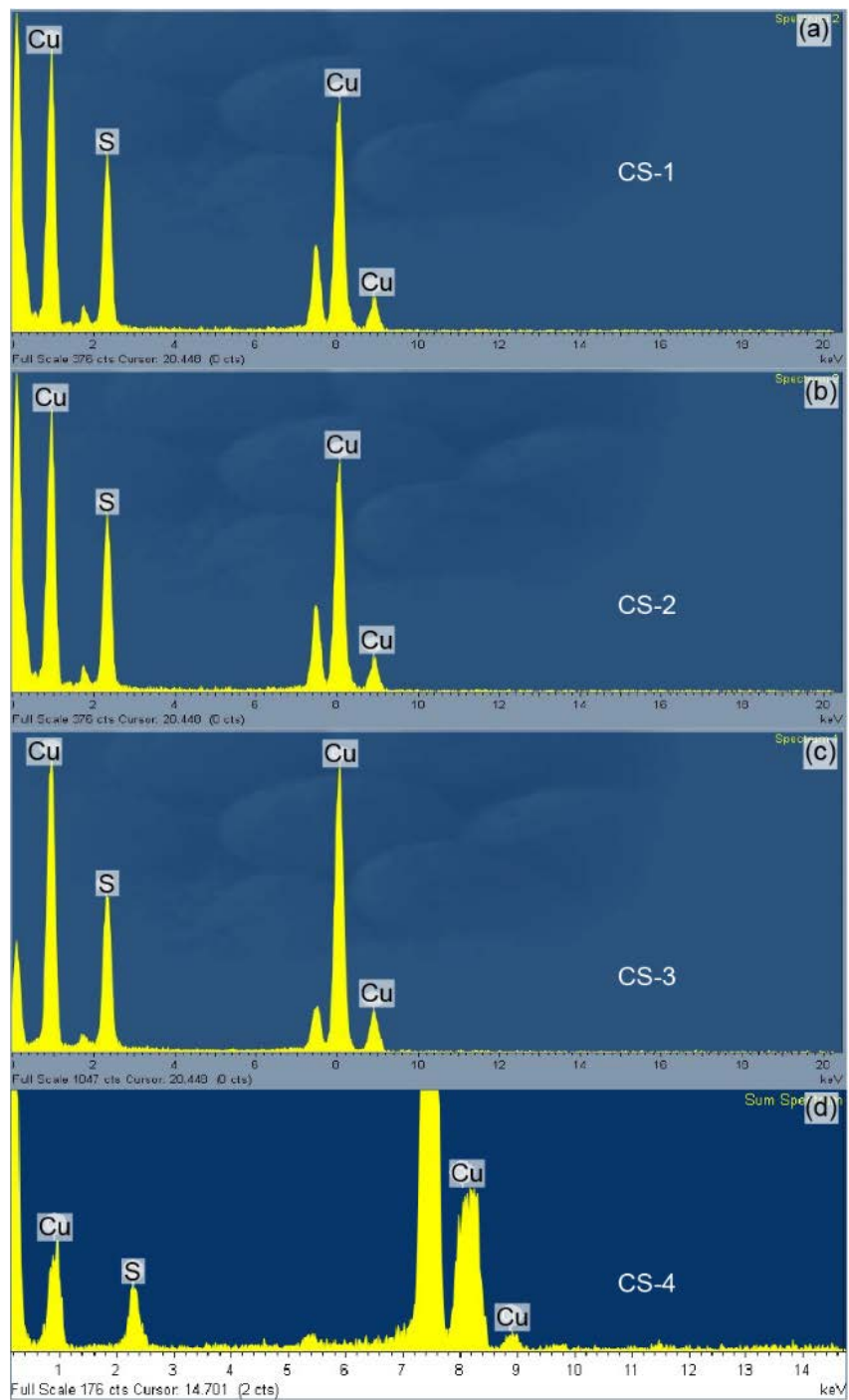


**Figure 4.3** EDS spectrum of (a) CS-1, (b) CS-2, (c) CS-3, and (d) CS-4.

**Table 4.2** A summary of elements composition in CS-1, CS-2, CS-3, and CS-4.

Samples	Theoretical ratios	Atomic ratios by EDS	
	Cu/S	Cu/S	ratio
CS-1	1	54.35/45.46	1.19
CS-2	1.8	64.38/35.62	1.81
CS-3	1.75	62.8/37.2	1.69
CS-4	2	66.23/33.77	1.96

#### 4.2.1.4 Ultraviolet–Visible spectroscopy and energy-gap calculation

Different stoichiometries in semiconductor materials can alter the physicochemical properties of nanocrystals by changing the energy structure and levels. The optical properties of CS-1, CS-2, CS-3, CS-4 were firstly investigated by UV-Vis absorption spectroscopy, as shown in Figure 4.4. Absorbance in near infrared (NIR) region was found on  $\text{Cu}_x\text{S}$  with different copper vacancies, arising from the plasmonic effect of  $\text{Cu}_x\text{S}$  by its free holes, which is stoichiometry dependent. CS-1 shows a stronger NIR absorbance intensity, compared with a weaker absorbance from CS-2 and CS-3. However, no NIR absorbance was observed on CS-4 with full stoichiometry. The band gap energies of the  $\text{Cu}_x\text{S}$  were estimated by a classical Tauc plot using the Kubelka-Munk equation. In the case of direct transition semiconductor,<sup>210,211</sup> the square of absorption coefficient  $\alpha$  multiplied by the photon energy ( $h\nu$ ) versus  $h\nu$  was plotted, a band gap energy of 2.21 eV was calculated for CS-1, 2.11 eV for CS-2, 1.93 eV for CS-3, and 1.62 eV for CS-4, respectively. The band gap values of  $\text{Cu}_x\text{S}$  vary with stoichiometry and increase with copper deficiency. These observations are consistent with the literature reports.<sup>211</sup> Hence, the compositional control of  $\text{Cu}_x\text{S}$  is an effective way to tune their optical properties by altering the optical band gap. Nevertheless, the light absorption range of all four  $\text{Cu}_x\text{S}$  NPs fall within the visible and near-infrared region ( $>420$  nm), demonstrating their potential application in sunlight absorber for solar energy harvesting and solar photochemical reactions.

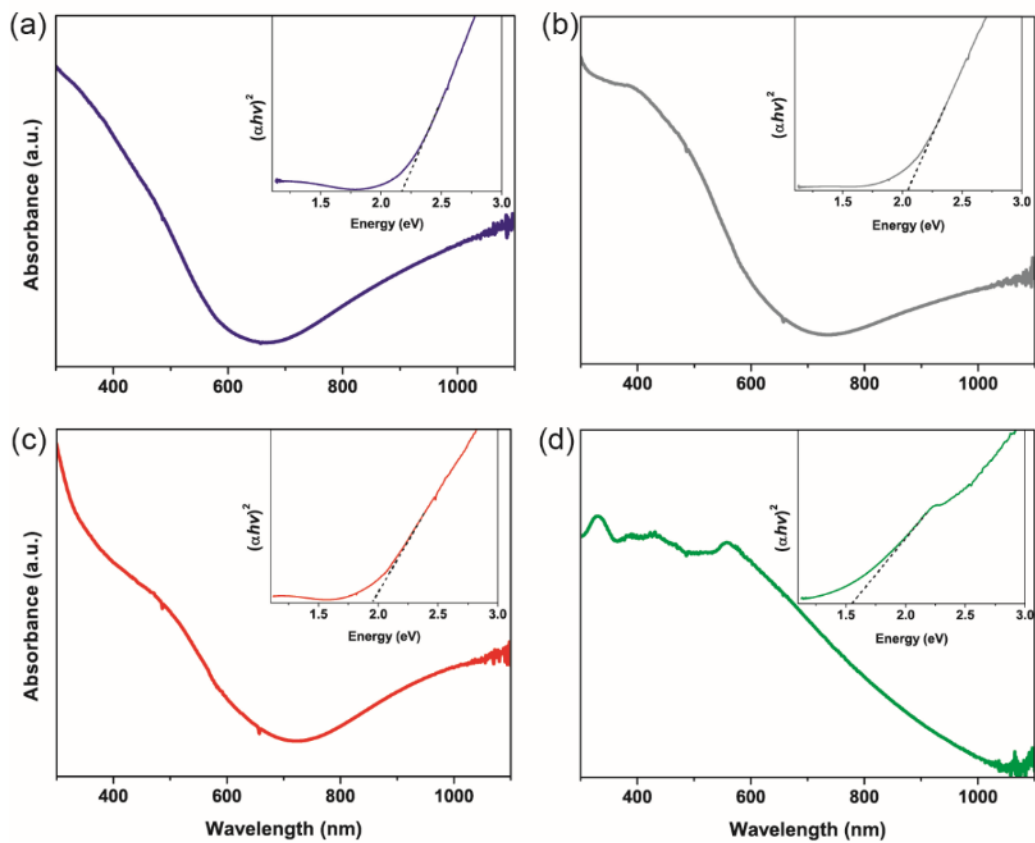


**Figure 4.4** UV-vis spectra and band gap energy estimation for (a) CS-1, (b) CS-2, (c) CS-3, and (d) CS-4. The dotted line is the extrapolation from the linear region of  $(\alpha hv)^2$  plotted against  $hv$ .

#### 4.2.1.5 Photocatalytic hydrogen evolution

It is of much interest to find out how  $\text{Cu}_x\text{S}$  with different Cu vacancies affect the photochemical activity. The photocatalytic HER performance of CS-1, CS-2, CS-3, CS-4 was evaluated under simulated sunlight irradiation for 3 h and the amount of  $\text{H}_2$  amount evolved was measured each hour. A mixed solution of 0.35 M  $\text{Na}_2\text{S}$  + 0.25 M  $\text{Na}_2\text{SO}_3$  (aq) was used as the sacrificial agent for scavenging photogenerated holes. The  $\text{H}_2$  gas evolution rates of the  $\text{Cu}_x\text{S}$  photocatalysts were calculated by measuring the evolved  $\text{H}_2$  gas with gas chromatography (GC), shown in Figure 4.5 for comparison.

Among the  $\text{Cu}_x\text{S}$  NPs compared, CS-2 shows the highest  $\text{H}_2$  gas evolution rate ( $167.9 \mu\text{mol h}^{-1} \text{g}^{-1}$ ) (Figure 4.5). The rates of  $\text{H}_2$  gas evolution for CS-1, CS-3, and CS-4 are 72.3, 131.9, and  $110.6 \mu\text{mol h}^{-1} \text{g}^{-1}$ , respectively. The results demonstrated a higher photochemical activity of CS-2 in the  $\text{Cu}_x\text{S}$  system for photocatalytic HER. All the hydrogen evolution rates from these  $\text{Cu}_x\text{S}$  photocatalysts were higher than the reported rates of general photocatalysts (e.g. N-doped  $\text{TiO}_2$ , CdS NPs)<sup>212,213</sup> under simulated sunlight illumination. Therefore, the potential application of these  $\text{Cu}_x\text{S}$  NPs as a new generation of photocatalysts is demonstrated.

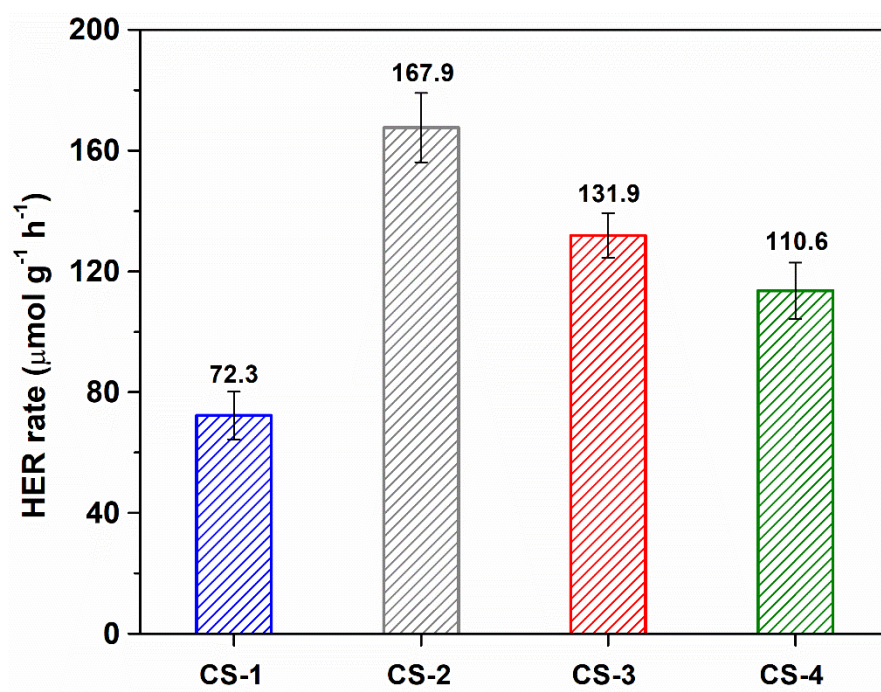


*Figure 4.5* A comparison of the photocatalytic H<sub>2</sub> gas evolution rates among CS-1, CS-2, CS-3, and CS-4.

## 4.2.2 Cu<sub>x</sub>S nanoparticles with multiple phase-junctions

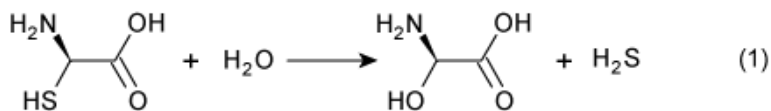
### 4.2.2.1 Powder X-ray diffraction

Attempts to make Cu<sub>x</sub>S nanoparticles with phase-junctions were done by an en-mediated hydrothermal method, with varying ratios of the en moiety. Typically, equal molar of *L*-cysteine and Cu (oleate)<sub>2</sub> were mixed in the binary medium containing a certain volume of en in water, followed by hydrothermal reaction. It is expected that different crystal phases of Cu<sub>x</sub>S could be achievable by stabilizing metastable phases through fine-tuning ratios of en moiety in water. The Cu<sub>x</sub>S products were collected as solid powders.

To investigate the crystalline structure and phase composition, powder XRD was employed and the patterns are shown in Figure 4.6. From Figure 4.6(a) and (b), each product shows two sets of diffraction patterns, one consists of hexagonal CuS and hexagonal Cu<sub>1.8</sub>S, labeled as CS-12, the other one comprises of hexagonal Cu<sub>1.8</sub>S and monoclinic Cu<sub>1.75</sub>S, labeled as CS-23. CS-12 has two sets of diffraction peaks at 27.77°, 32.16°, 46.17°, and 54.70° respectively indexed to (0 0 15), (1 0 10), (0 1 20), and (1 1 15) crystal planes of Cu<sub>1.8</sub>S and 29.28°, 31.78°, 32.85°, 47.94°, 52.71°, 59.35° respectively indexed to (1 0 2), (1 0 3), (0 0 6), (1 1 0), (1 0 8), (1 1 6) crystal planes of CuS. CS-23 has characteristic peaks at 20.85°, 24.71°, 31.20°, 34.06°, 36.62°, 46.84°, 48.90° respectively indexed to (12 2 0), (3 7 2), (18 2 1), (20 0 1), (1 5 5), (0 16 0), (8 8 6) crystals planes of

$\text{Cu}_{1.75}\text{S}$  and  $27.77^\circ$ ,  $32.16^\circ$ ,  $46.17^\circ$  from (0 0 15), (1 0 10), (0 1 20) crystal planes of  $\text{Cu}_{1.8}\text{S}$ .

At the early stage of reaction, hydrogen sulfide was formed from the decomposition of *L*-cysteine which reacted with the  $\text{Cu}^{2+}$  ions to form  $\text{CuS}$ .<sup>214</sup>  $\text{Cu}_{1.8}\text{S}$  was found to form when the en ratio was 5 vol%, indicating that some  $\text{Cu}^{2+}$  were reduced to  $\text{Cu}^+$  by the en moiety.<sup>205</sup> However, two sets of diffraction patterns from  $\text{Cu}_{1.8}\text{S}$  and  $\text{Cu}_{1.75}\text{S}$  were found at a higher en ratio over 25 vol%, while the diffraction pattern of  $\text{CuS}$  disappeared. The reaction route for the synthesis of  $\text{Cu}_{1.8}\text{S}$  and  $\text{Cu}_{1.75}\text{S}$  can be described as follows.



Different ratios of en moiety are proven to produce different amounts of  $\text{Cu}^+$  species, which may modulate the crystal phase in  $\text{Cu}_x\text{S}$  and the growth of thermodynamically stable crystal phase.<sup>205</sup> The locations of Cu atoms within the sublattice of S atoms are reported to be mobile at elevated temperatures, making  $\text{Cu}_x\text{S}$  a partially ionic conductor.<sup>215</sup> Further, the phase transformations of  $\text{Cu}_x\text{S}$

from hexagonal to monoclinic packing by S atoms rearrangement are slow,<sup>191</sup> which may lead to the existence of two polymorphs in both CS-12 and CS-23. Further increased the ratio of en moiety in the binary medium cannot enable the synthesis of  $\text{Cu}_2\text{S}$ , which is possibly due to the solid-state reaction of  $\text{Cu}^+$  species with CuS in the off-stoichiometric  $\text{Cu}_x\text{S}$  polymorphs.

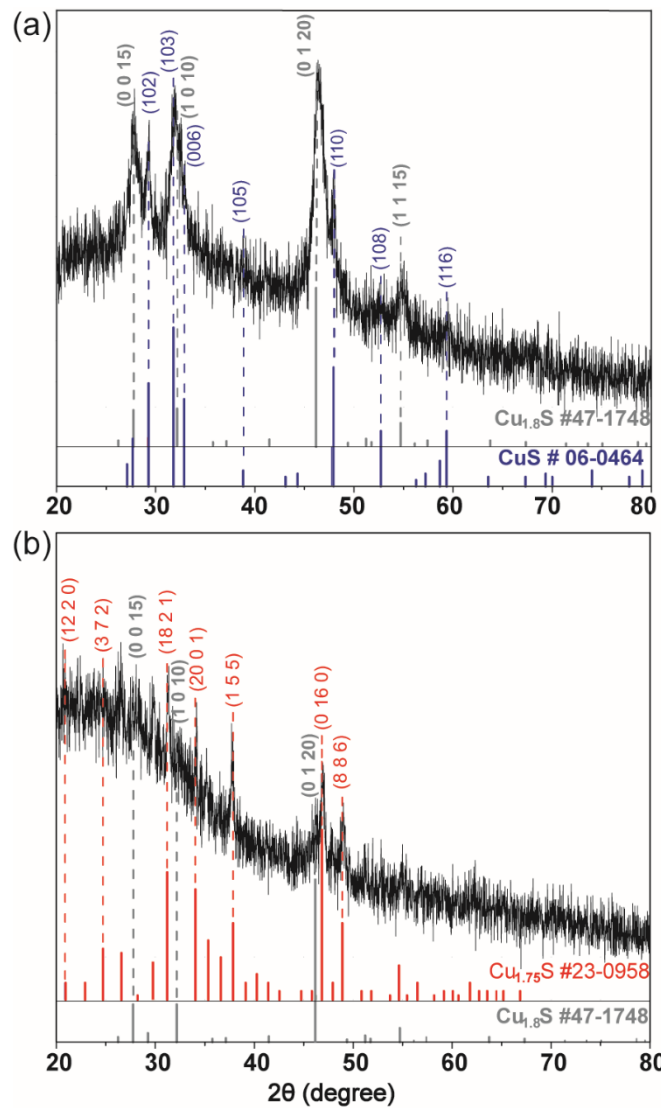


**Figure 4.6** Powder XRD patterns of  $\text{Cu}_x\text{S}$  with two patterns from (a) CS-12 and (b) CS-23. The standard JCPDS XRD patterns for  $\text{CuS}$  (No. 06-0464),  $\text{Cu}_{1.8}\text{S}$  (No. 47-1748) and  $\text{Cu}_{1.75}\text{S}$  (No. 23-0958) are shown at the bottom.

#### 4.2.2.2 Transmission electron microscopy

The size and morphology of the obtained  $\text{Cu}_x\text{S}$  NPs have also been studied by TEM analysis. The low-resolution TEM images of the  $\text{Cu}_x\text{S}$  NPs are shown in Figure 4.7 (a) and (c). CS-12 shows spherical shape with an average diameter of  $81 \pm 10.6$  nm. However, the CS-23 NPs showed irregular shapes with an average size of  $92 \pm 9.8$  nm. The obtained  $\text{Cu}_x\text{S}$  with different stoichiometries shows different dimensions, which can be related to the different concentrations of en moiety from different amounts of  $[\text{Cu}(\text{en})_2]^{2+}$  cuprammonium complexes as molecular templates. The HR-TEM images, shown in Figure 4.7(b) and (d), of CS-12 and CS-23 reveal light/dark contrast with multiple lines across the nanoparticles. This suggests the formation of twinned structure on the  $\text{Cu}_x\text{S}$  evolving from CuS to  $\text{Cu}_{1.8}\text{S}$ , from  $\text{Cu}_{1.8}\text{S}$  to  $\text{Cu}_{1.75}\text{S}$ , generating phase-junctions by phase transformation. However, close-up view for locating phase-junctions was failed, probably resulted from the electron-induced structural reconstruction and phase transition induced during electron beam focus in TEM.<sup>216</sup>

Furthermore, multiple stripe-like interfaces can be observed throughout the crystal lattice of the CS-23 NPs, indicating that an increased density of twin structures when a higher concentration of en moiety was used. The twin structure caused by phase transformation in the growth of semiconductor nanomaterials,<sup>166</sup> supports the observation of multiple phase-junctions on the  $\text{Cu}_x\text{S}$  nanocrystals. In addition, the phase-junctions usually coincide with lattice mismatches between two crystal phases,<sup>217</sup> particularly between hexagonal  $\text{Cu}_{1.8}\text{S}$  structures and

monoclinic  $\text{Cu}_{1.75}\text{S}$  structures, which can alter lattice parameters such as lattice strain and interplanar spacings.<sup>218</sup> Interestingly, the multiple interfaces are observed to be parallel to each other and across the body of each particle, suggesting that the transformation of hexagonal  $\text{Cu}_{1.8}\text{S}$  structures into monoclinic  $\text{Cu}_{1.75}\text{S}$  proceeds in a layer-by-layer manner.<sup>219</sup> It has been reported that mismatched lattices have excess elastic energy within phase-junctions,<sup>220</sup> which implies the introduction of high energy surfaces onto  $\text{Cu}_x\text{S}$  by the multiple phase-junctions. The high energy surfaces may possess potential activities for catalyzing chemical reactions.

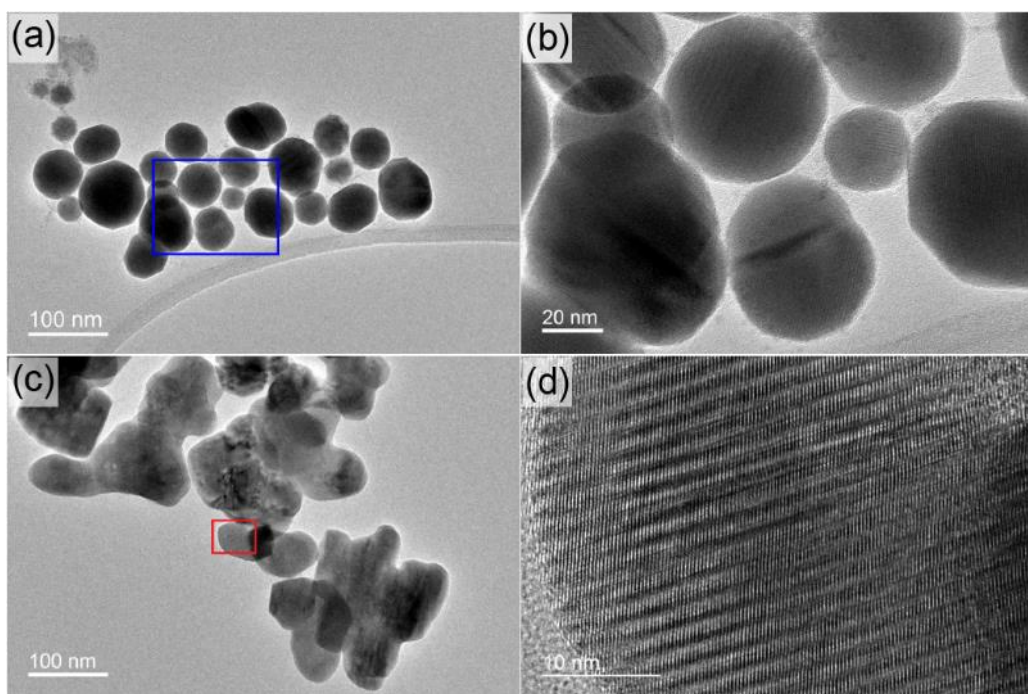


**Figure 4.7** low-resolution TEM images of  $\text{Cu}_x\text{S}$  (a) CS-12 and (b) CS-23 and corresponding high-resolution TEM images in (b) and (d).

#### 4.2.2.3 Energy dispersive X-ray spectroscopy

Energy dispersive X-ray spectroscopy (EDS) measurements were performed to determine the average compositions of as-synthesized  $\text{Cu}_x\text{S}$  NPs, the maps of detected elements are shown in Figure 4.8. By measuring the atomic weight from multiple spots for each sample, the atomic ratios of Cu/S for CS-12 and CS-23 are summarized in Table 4.3. It can be found that the atomic ratios of CS-12 fall between 1.39 and 1.52, while the ratios of CS-23 is from 1.69 to 1.77, demonstrating the altered stoichiometries in the  $\text{Cu}_x\text{S}$  nanocrystals with multiple phase-junctions. As a result, the average composition in CS-12 corresponds to  $\text{Cu}_{1.44}\text{S}$ , and CS-23 corresponds to  $\text{Cu}_{1.73}\text{S}$ .

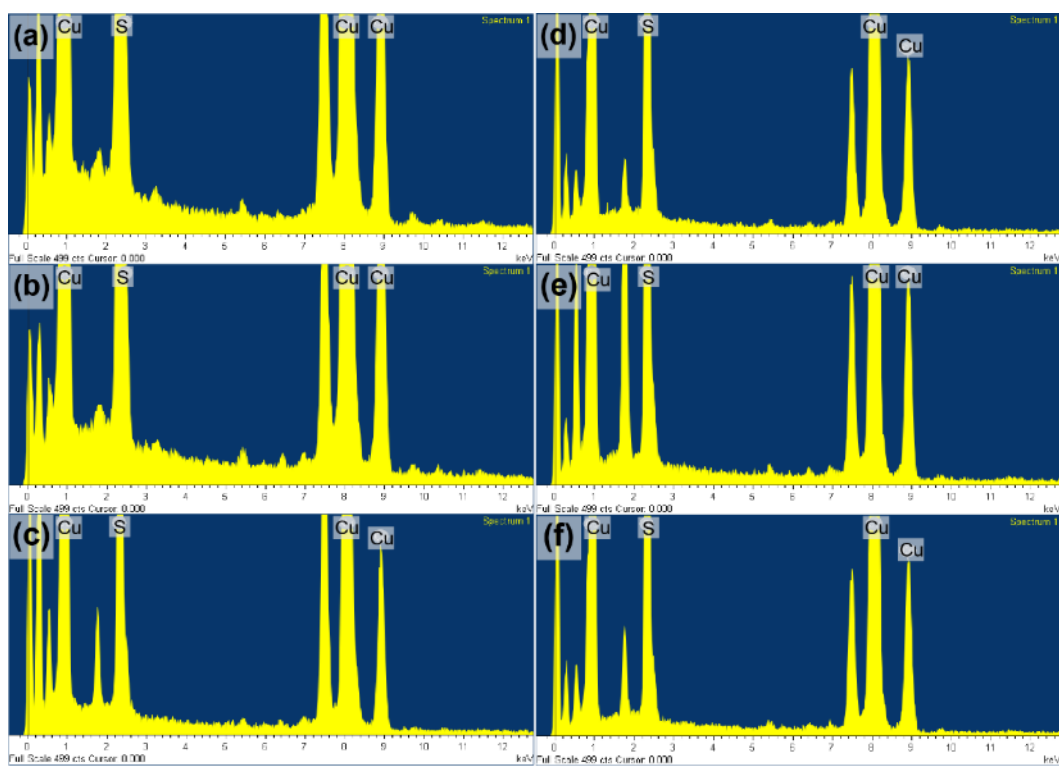


**Figure 4.8** Elemental analysis by EDS on three different spots from (a)-(c) in CS-12, and (d)-(f) in CS-23.

**Table 4.3** A summary of experimental elements composition in CS-12, CS-23.

Samples	Atomic ratios by EDS					
	Spot 1		Spot 2		Spot 3	
	Cu/S	ratio	Cu/S	ratio	Cu/S	ratio
CS-12	58.20/41.80	1.39	58.65/41.35	1.42	60.28/39.72	1.52
CS-23	62.77/37.23	1.69	63.25/36.75	1.72	63.74/36.26	1.77

#### 4.2.2.4 Ultraviolet–visible spectroscopy and energy-gap calculation

Multiple junctions have been revealed to alter physicochemical properties of semiconductor materials by lowering the energy barriers thus enhancing activity.<sup>221</sup> Thus, the multi-junctions effect on the optical properties of the  $\text{Cu}_x\text{S}$  nanocrystals was firstly studied by UV-Vis absorption spectroscopy as shown in Figure 4.9. Absorbance in near infrared (NIR) region was found in  $\text{Cu}_x\text{S}$  with multiple phase-junctions, derived from free charge carriers by plasmon on the surface. A stronger NIR absorbance intensity of CS-12 can be seen in comparison with that of CS-23, confirming the dependence of free carriers on the stoichiometry in  $\text{Cu}_x\text{S}$  with different Cu vacancies. The energy gaps of the  $\text{Cu}_x\text{S}$  were estimated by a Tauc plot using Kubelka-Munk equation. The calculated energy gap of the CS-12 is 2.16 eV, while CS-23 has a much narrower energy gap of 2.04 eV. The energy gap values of  $\text{Cu}_x\text{S}$  comprising two crystal phases are found to vary with the stoichiometry in  $\text{Cu}_x\text{S}$ , as shown in Figure 4.10. Typically,  $\text{Cu}_x\text{S}$  with different stoichiometric compositions have a certain degree of Cu vacancies, compared with CS-4 ( $\text{Cu}_2\text{S}$  in full stoichiometry). The order in an increasing trend of Cu vacancy number is, CS-4 ( $\text{Cu}_2\text{S}$ ) > CS-2 ( $\text{Cu}_{1.8}\text{S}$ ) > CS-23 > CS-3 ( $\text{Cu}_{1.75}\text{S}$ ) > CS-12 > CS-1 ( $\text{CuS}$ ).

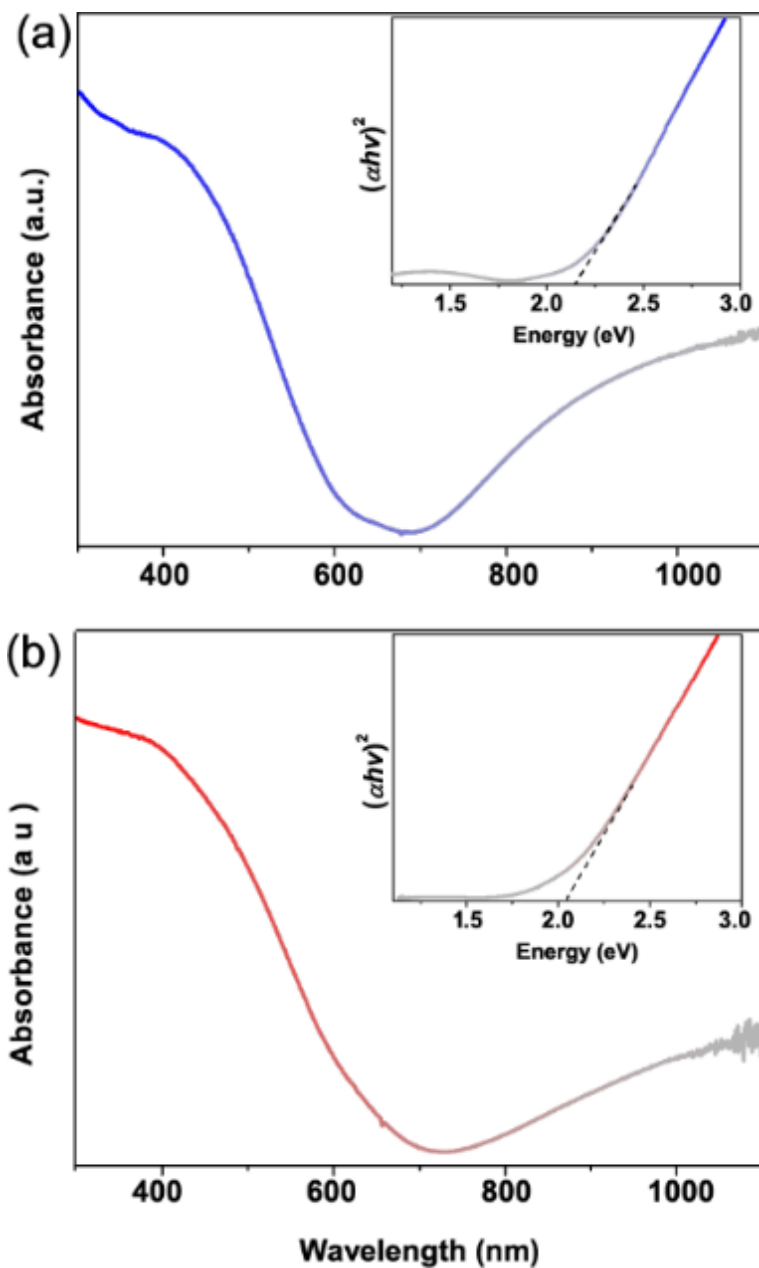


**Figure 4.9** UV-vis spectra of (a) CS-12, (b) CS-23. Inset is band gap energy estimation by a dotted line extrapolated from the linear region of  $(\alpha h\nu)^2$  plotted against energy ( $h\nu$ ).

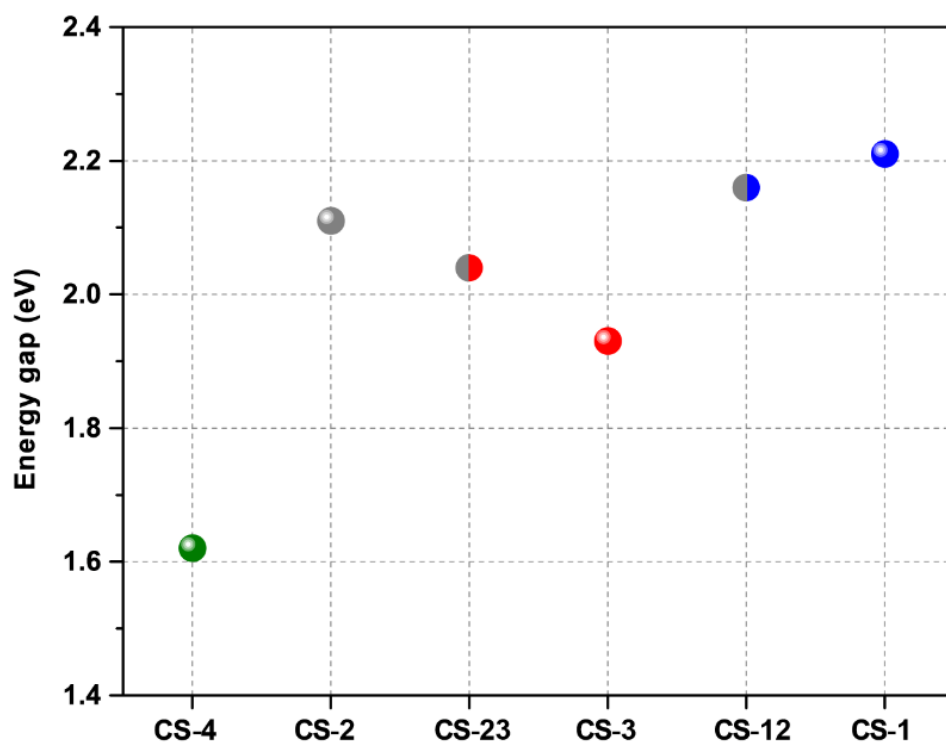


*Figure 4.10* Energy gap values of  $\text{Cu}_x\text{S}$  ( $1 \leq x \leq 2$ ) with different stoichiometries.

#### 4.2.2.5 Photocatalytic hydrogen evolution

It is of much interest to see how the junctions in  $\text{Cu}_x\text{S}$  affect the photochemical activity for photocatalytic reaction. The photocatalytic HER on the CS-12, CS-23 NPs was performed under simulated sunlight irradiation for 3 h and the  $\text{H}_2$  amount evolved was measured each hour. A polysulfide solution of 0.35 M  $\text{Na}_2\text{S}$  + 0.25 M  $\text{Na}_2\text{SO}_3$  (aq) was used as the sacrificial agent for photogenerated hole scavenger. For comparison, a CS-1 and CS-2 mixture (labeled as CS-1/CS-2), and a CS-2 and CS-3 mixture (labeled as CS-2/CS-3) were also tested at the identical conditions. The  $\text{H}_2$  evolved rates of the  $\text{Cu}_x\text{S}$  were calculated by measuring the photogenerated  $\text{H}_2$  gas with gas chromatography (GC). The results are shown in Figure 4.11.

Control samples of CS-1/CS-2, CS-2/CS-3 mixtures showed HER rate of 128.3, 156.5  $\mu\text{mol g}^{-1} \text{h}^{-1}$ , respectively, which are slightly higher than CS-1 and CS-3 alone. CS-12 and CS-23 with multiple interfaces show significantly enhanced photocatalytic performances at the  $\text{H}_2$  evolved rates of 278.2 and 383.7  $\mu\text{mol g}^{-1} \text{h}^{-1}$ , which account for 165 and 230 % enhancement from the single-phase copper sulfide (CS-2), respectively. This enhancement indicates that the interfacial contact is critical to the electron transfer between the two components for water reduction reaction to hydrogen. Such boosted HER rate was achieved without using any co-catalyst (such as noble metal or semiconductor nanomaterials) or supportive materials. Associated with the TEM images, the enhanced photocatalytic activity of CS-23 can be corroborated with the increased density

of multiple interfaces, which may form multiple staggered type-II energy band alignments<sup>222</sup> that effectively drive the spatial separation of photogenerated charge carriers. Interestingly, the interfacial structures are generally lattice-mismatched layers because of excess strain at the junctions, making multiple highly-active sites available on the materials. As a result, the presence of multiple interfaces shows much improved photochemical activities, which is similar to the interface-dependent ZnS nanocrystals with boosted HER performances.<sup>129, 151</sup> Furthermore, such multiple interfaces in close pattern is shown to suppress the charge recombination and favor the transport of charge carriers.<sup>223-225</sup> Therefore, this construction of multiple interfaces by phase-junctions in  $\text{Cu}_x\text{S}$  nanocrystals could inspire a new class of narrow bandgap semiconductor materials with highly-active catalytic properties.

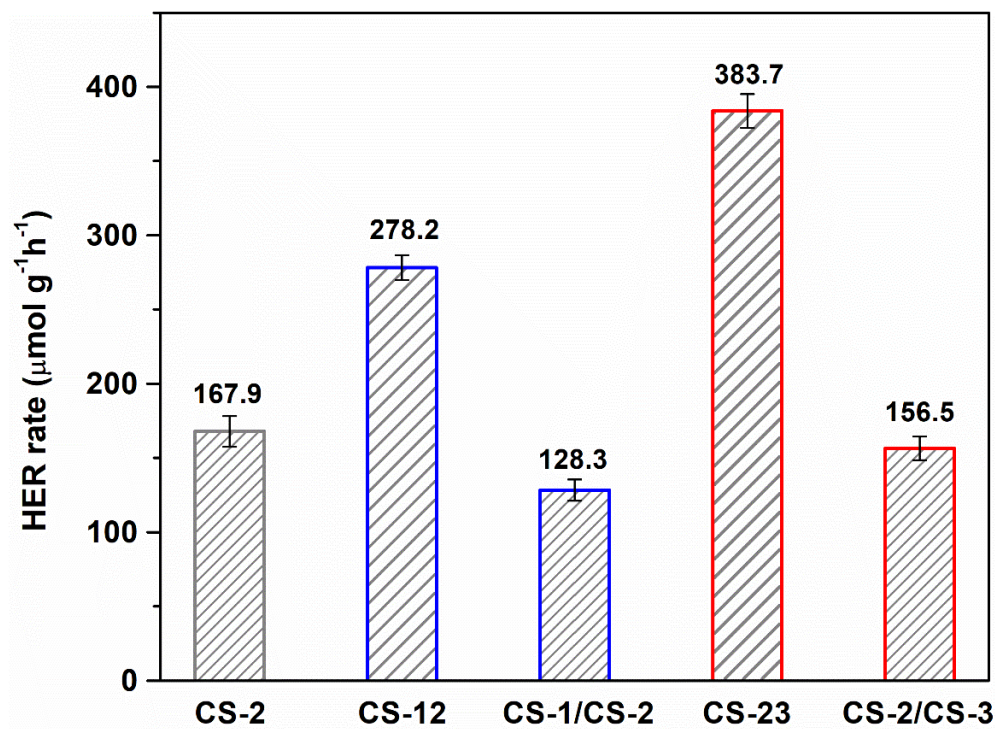


**Figure 4.11** Photocatalytic H<sub>2</sub> gas evolution rates for CS-12, CS-23 compared with single-phase CS-2, CS-1/CS-2 mixture and CS-2/CS-3 mixture.

### 4.3 Concluding remarks

Four kinds of  $\text{Cu}_x\text{S}$  ( $1 \leq x \leq 2$ ) nanocrystals with different Cu/S stoichiometries ( $\text{CuS}$ ,  $\text{Cu}_{1.75}\text{S}$ ,  $\text{Cu}_{1.8}\text{S}$  and  $\text{Cu}_2\text{S}$ ) were prepared by an ethylenediamine-mediated hydrothermal method. A higher ethylenediamine ratio in the ethylenediamine-water medium was found to yield monoclinic  $\text{Cu}_{1.75}\text{S}$  compared with the hexagonal  $\text{Cu}_{1.8}\text{S}$ . By fine-tuning the concentration of ethylenediamine, multiple phase-junctions are introduced to  $\text{Cu}_x\text{S}$  nanocrystals to modify their surface states, which was found to improve the photochemical activity in photocatalytic  $\text{H}_2$  gas evolution from water. The phase-junction-rich  $\text{Cu}_x\text{S}$  nanocrystal comprising  $\text{Cu}_{1.75}\text{S}$ - $\text{Cu}_{1.8}\text{S}$  exhibited a significantly enhanced photocatalytic  $\text{H}_2$  gas evolution rate of  $383 \mu\text{mol g}^{-1} \text{h}^{-1}$ , which is *ca.* 2.3 times higher than that of single phase  $\text{Cu}_{1.8}\text{S}$  under simulated sunlight irradiation. With such phase-junctions on  $\text{Cu}_x\text{S}$ , an active surface arising from multiple interfaces is believed to lower the energy barrier for reaction and improves the photochemical activity of  $\text{Cu}_x\text{S}$  for  $\text{H}_2$  gas evolution reaction in water.

## **Chapter 5**

### **Au Morphology-dependent Plasmon-enhanced Photocatalytic Water Reduction to Hydrogen by Au/Copper Sulfide Yolk-Shell Nanostructure**

## 5.1 Introduction

Integration of semiconductor nanomaterials with plasmonic metals to form plasmonic metal/semiconductor hetero-nanostructure has recently received much attention and as it can lead to an enhanced conversion efficiency in photocatalysis<sup>226</sup> and solar cells.<sup>227</sup> Photocatalytic hydrogen evolution reaction (HER) from water, as a green measure for solar fuel generation, has long been an important solar energy conversion reaction and attracted numerous research works on the photocatalyst nanostructure engineering. Over past decade, the plasmonic metal-semiconductor, hybrids of Au, Ag, and Cu nanomaterials and semiconductor has become an important class of photocatalysts for boosting HER performance and more.<sup>228-230</sup> With superior stability and strong surface plasmon resonance (SPR) effect, Au nanostructures are usually introduced onto semiconductor to improve its performance by a modified interface between Au and semiconductor. A new Fermi level equilibrium can be formed at the interface which effectively promotes transfer of photogenerated charge carrier,<sup>231</sup> for improved HER performance. To this target, several Au-semiconductor nanostructures have been designed that including core-shell,<sup>35, 232</sup> Janus type,<sup>136, 233</sup> yolk-shell,<sup>234-236</sup> and multiple phase-junctions,<sup>140, 237</sup> and showed significant enhancements on HER performance.

In particular, the yolk-shell Au-semiconductor photocatalysts have been reported to exhibit significant enhancement from individual semiconductor nanomaterials.<sup>238</sup> It is widely accepted that the photocatalytic activity is closely

associated with the amount of photogenerated electron-hole pairs, which is strongly dependent on the capability of light absorption of the photocatalyst. It is also known that in the hollow structure, incident light can be reflected and scattered then redirected to nearly all directions, leading to a greater utilization of incident light due to an increased light path length. To date, Au-semiconductor yolk-shell photocatalysts are rare in the literature, for example, Au-TiO<sub>2</sub><sup>239</sup> and Au-CdS<sup>235</sup> have shown much greater photoactivity as benefited from the nanostructure. The multiple light reflection and scattering in-between the yolk and shell are claimed to be responsible for an enhanced local-field of Au, giving rise to the boosted photocatalytic performance. However, semiconductors such as TiO<sub>2</sub>, CdS suffer from demerits such as weak photo-response from wide bandgap (above 3 eV) and toxicity, respectively. Green semiconductors with a suitable bandgap for greater light harvesting are therefore needed.

The copper sulfide family (Cu<sub>2-x</sub>S, 0 ≤ x ≤ 1), as an efficient solar absorber,<sup>240, 241</sup> has been explored for solar-to-fuel applications due to its near-ideal bandgaps (1.2-2.35 eV)<sup>193</sup> for light harvesting and earth abundance. Cu<sub>2-x</sub>S shows intense near-infrared (NIR) absorption arising from the collective oscillation of holes, which is an indication of the unique localized SPR effect.<sup>242</sup> Typically, digenite Cu<sub>1.8</sub>S is a stable and less resistive semiconductor material with a suitable band gap of 1.5-1.9 eV,<sup>30, 243</sup> and has shown its robustness for photocatalytic HER<sup>30</sup>. By constructing Au-Cu<sub>1.8</sub>S yolk-shell structure, multiple light reflections and scattering are introduced to enable light collision with the Au yolk and the Cu<sub>1.8</sub>S

shell. This structure not only increases the light path length but also allows for SPR coupling between the plasmonic Au and plasmonic copper sulfide, provides a platform to investigate their photocatalytic activities. Thus, the plasmonic coupling of Au with  $\text{Cu}_{1.8}\text{S}$  could be advantageous for HER not only due to increased efficiency of charge carriers generation from enhanced light harvesting but a basic understanding of SPR couplings of two plasmonic components.<sup>244</sup>

Herein, the Au nanostructures with different shapes are embedded in the  $\text{Cu}_{1.8}\text{S}$  hollow nanocage (HNG), and their photocatalytic activities on  $\text{H}_2$  gas evolution from water are investigated by measuring the evolution rates. The multi-scatterings in-between nanostructures are greatly dependent on the shape of Au and the distance between the yolk and the shell materials. Therefore, three different Au- $\text{Cu}_{1.8}\text{S}$  yolk-shell nanostructures were prepared; one is spherical Au nanoparticles, the second is Au nanorods, and the third one is Au nanostar with multiple spikes. The synthesized Au- $\text{Cu}_{1.8}\text{S}$  heterostructure NPs were characterized by transmission electron microscopy (TEM), energy dispersive spectroscopy (EDS), and Ultraviolet-visible absorption spectroscopy (UV-vis) as well as powder X-ray diffraction (PXRD). The photocatalytic HER tests were carried out using the hetero-nanostructures, to evaluate the plasmonic enhancement by various combination of nanostructures.

## 5.2 Results and discussion

### 5.2.1 Au nanomaterials

#### 5.2.1.1 Transmission electron microscopy

Au nanoparticles with different shapes were prepared by a seed-mediated approach. Firstly,  $\text{NaBH}_4$  was used to reduce  $\text{HAuCl}_4$  into Au seeds, which were stabilized by CTAB at room temperature. The growth of seeds into nanosphere was induced by adding additional  $\text{HAuCl}_4$  and ascorbic acid (AA) for 2h. Alternatively, adding the seed solution to a growth solution containing a mixture of  $\text{HAuCl}_4$ ,  $\text{AgNO}_3$  and AA for a period of 6 h induced the nanorod formation.

The sizes and morphologies of the obtained Au nanoparticles were studied by transmission electron microscopy (TEM). The TEM images shown in Figure 5.1 clearly revealed the 0,1, and 3 dimensional structures of Au nanosphere (NP), Au nanorod (NR) and Au nanostar (NS), respectively. The Au NPs have a spherical shape with an average diameter of  $45 \pm 5.8$  nm. The Au NRs have a regular rod shape with an average length of  $77 \pm 4.6$  nm in length and a diameter of  $34 \pm 2.7$  nm with an aspect ratio of 2.2. The Au NSs have an average core diameter of  $48 \pm 7.5$  nm with non-uniform structures and various number of spikes in different length are observed.

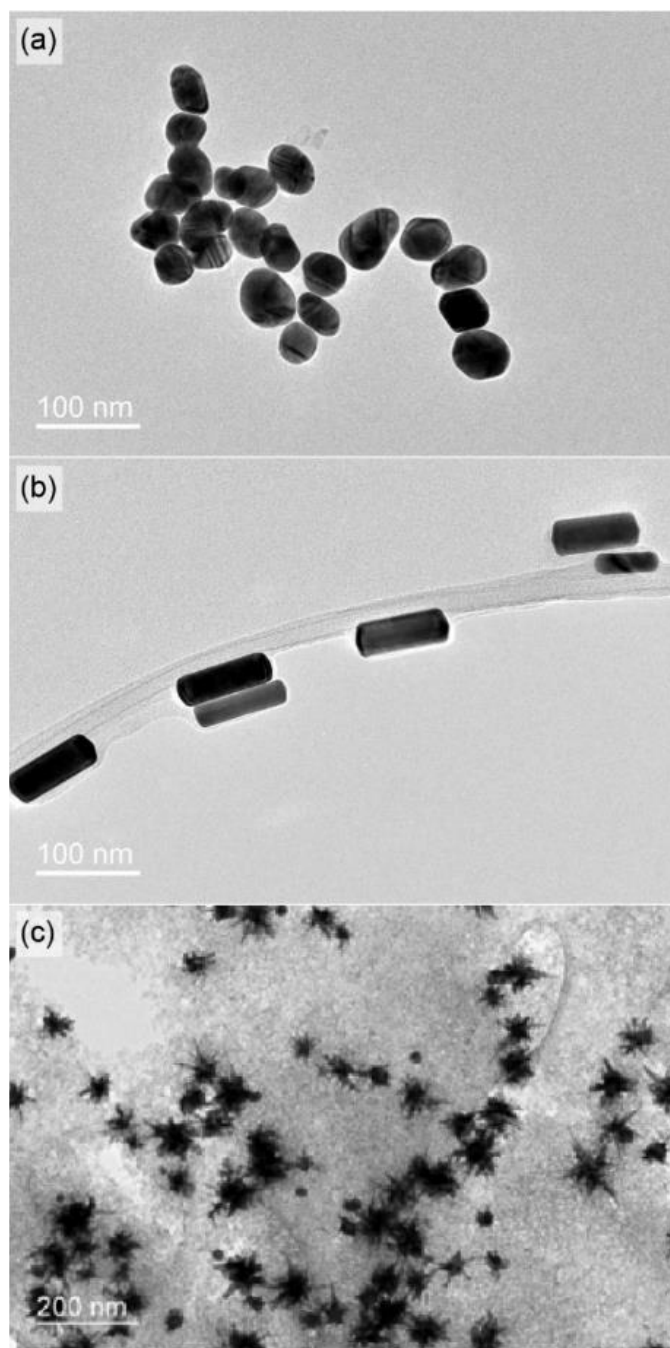


**Figure 5.1** TEM images of Au nanomaterials with different shapes (a) nanosphere (b) nanorod and (c) nanostar.

### 5.2.1.2 Ultraviolet-visible absorption spectroscopy

Optical properties of the Au nanomaterials with different shapes were studied by ultraviolet–visible (UV-Vis) absorption spectroscopy. From the UV-Vis spectra in Figure 5.2, Au NPs as a typical 0-dimensional nanomaterial show a single peak at 530 nm, whereas the Au NRs exhibit dual band peaks at 515 and 740 nm, originating from the transverse and longitudinal free electrons oscillation from the interactions with electromagnetic field.<sup>245</sup> The Au NSs with multiple spikes exhibit a broad band peak at 656 nm, which can be associated with its anisotropic property by multiple spikes.<sup>246</sup> The distinctive optical properties of these Au nanomaterials are expected to play a crucial role on their photo-electric activity due to their different electromagnetic field enhancements.

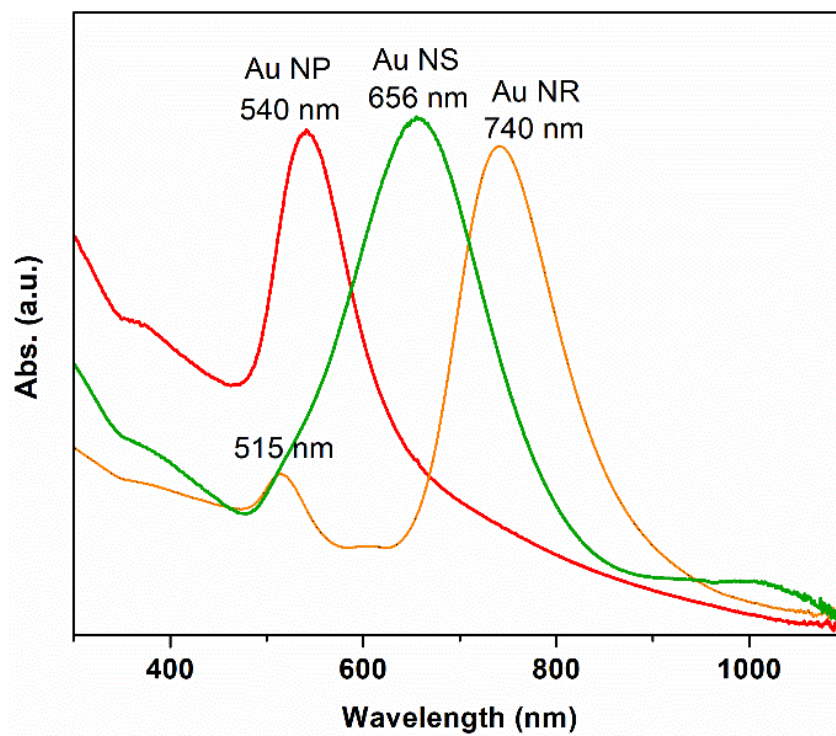
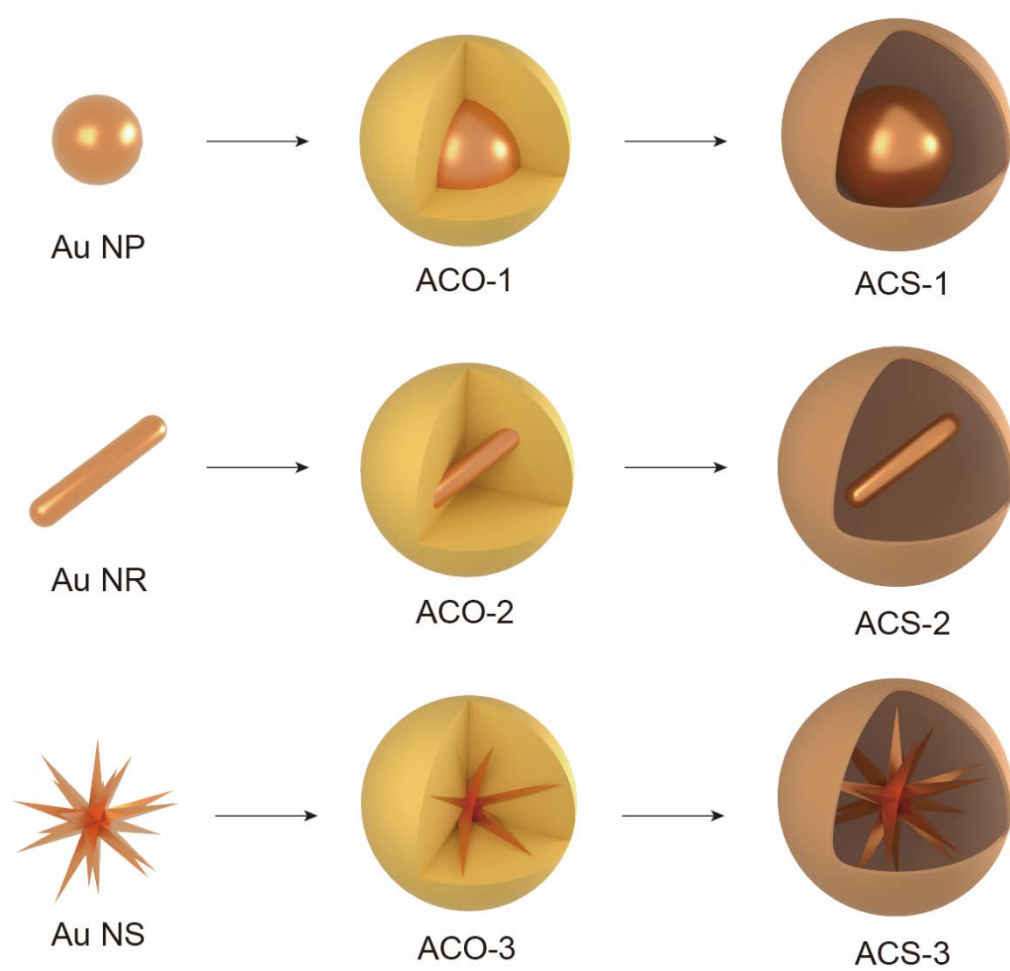


*Figure 5.2* UV-Vis-NIR absorption spectra of Au NP, Au NR and Au NS.

## 5.2.2 Precursor Au/Cu<sub>2</sub>O nanostructure

### 5.2.2.1 Powder X-ray diffraction

The Au-Cu<sub>2</sub>O hetero-structured nanoparticles were prepared via *in-situ* nucleation and growth approach, which was used as sacrificial templates to produce various Au-copper sulfide nanostructures. A schematic diagram of the synthetic procedure is shown in Scheme 5.1. Each pre-prepared Au nanomaterial with different shape was well mixed with Cu<sup>2+</sup> and hydroxylamine to allow [Cu(NH<sub>2</sub>OH)]<sup>2+</sup> adsorbed on Au surface. The formation of Cu<sub>2</sub>O nuclei on Au surface was *in situ* initiated by adding OH<sup>-</sup> and quenched after 1h reaction. The Au-Cu<sub>2</sub>O was cooled to 0 °C then treated with Na<sub>2</sub>S for surface sulfidation to form thin sulfide shell, followed by etching the Cu<sub>2</sub>O core using dilute HCl until a dark brown product Au-copper sulfide was yielded. The Au-Cu<sub>2</sub>O precursors containing Au NP, Au NR, and Au NS are labeled as ACO-1, ACO-2, and ACO-3, respectively. The Au-copper sulfide with Au NP, Au NR, Au NS are labeled as ACS-1, ACS-2, and ACS-3, respectively.



**Scheme 5.1** Schematic synthetic procedure of Au-Cu<sub>2</sub>O precursors and Au-copper sulfide hetero-structured nanoparticles.

To study the crystalline structure and phase compositions of the Au-Cu<sub>2</sub>O precursors, powder X-ray diffraction (XRD) was employed and the diffraction patterns are shown in Figure 5.3. The XRD patterns of Au and Cu<sub>2</sub>O are shown for reference, which can be indexed to the cubic phase Cu<sub>2</sub>O (No. 34-1354) and face-centered cubic (fcc) Au (No. 04-0748), respectively. The precursors show two sets of patterns featured by characteristic peaks from (110), (111), (200), (220), and (311) lattice planes of cubic Cu<sub>2</sub>O and (111), (200), (220), and (311) lattice planes of fcc Au, indicating that the precursors are only composed of Au and Cu<sub>2</sub>O. ACO-2 and ACO-3 show relatively weaker peaks for Au than Cu<sub>2</sub>O due to the embedded nature of Au<sup>247</sup>, while the stronger peaks for Au than Cu<sub>2</sub>O in ACO-1 suggest an uneven thinner Cu<sub>2</sub>O shell. Above all, the widened diffraction peaks in Au-Cu<sub>2</sub>O spectra indicate that the Au and Cu<sub>2</sub>O crystallites are nanocrystalline in nature.<sup>248</sup>

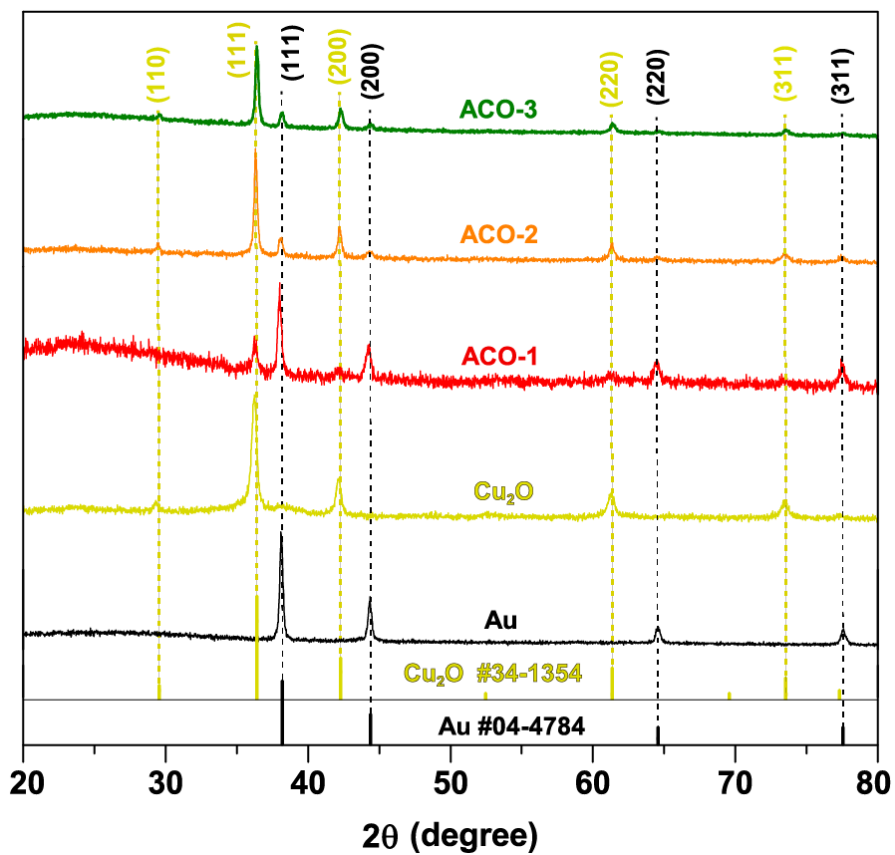


**Figure 5.3** Powder XRD pattern of ACO-1 (red), ACO-2 (orange), and ACO-3 (green). The standard JCPDS XRD patterns for Au (No. 04-0784) and Cu<sub>2</sub>O (No. 34-1354) are shown at the bottom.

### 5.2.2.2 Transmission electron microscopy

The nanostructures of the Au-Cu<sub>2</sub>O precursors were investigated by TEM. From the low-resolution TEM images in Figure 5.4 (a), (c) and (e), a core-shell nanostructure composed of an Au core and a Cu<sub>2</sub>O shell can be clearly seen by sharp contrast. ACO-1 with spherical shape and uniform morphology has an average size of  $205 \pm 6.7$  nm, ACO-2 is  $207 \pm 8.3$  nm in length and  $178 \pm 5.4$  nm in width, and ACO-3 has a diameter of  $189 \pm 3.6$  nm. The interfacial contact of Au and Cu<sub>2</sub>O is confirmed by close-up images are shown in Figure 5.4 (b), (d), and (f), with the Au cores preserving their shapes after Cu<sub>2</sub>O encapsulation.

To have a clearer view on the contrast between the core and shell material, high-angle annular dark-field imaging–scanning transmission electron microscopy (HAADF–STEM) imaging was taken to discern the core–shell heterostructure and interfacial contact, with bare Cu<sub>2</sub>O shown in Figure 5.5 (a) for reference. It is obvious to see the contrast between the Au core and Cu<sub>2</sub>O shell from Figure 5.5 (b)-(d), due to the different electron density of Au and Cu<sub>2</sub>O. From the entire samples that were studied, no nanoparticles with either multiple or without Au core were observed, confirming the successful encapsulation of each Au core by Cu<sub>2</sub>O. The obtained core–shell nanoparticles show uniform morphology, preserving the shape of the Au cores.

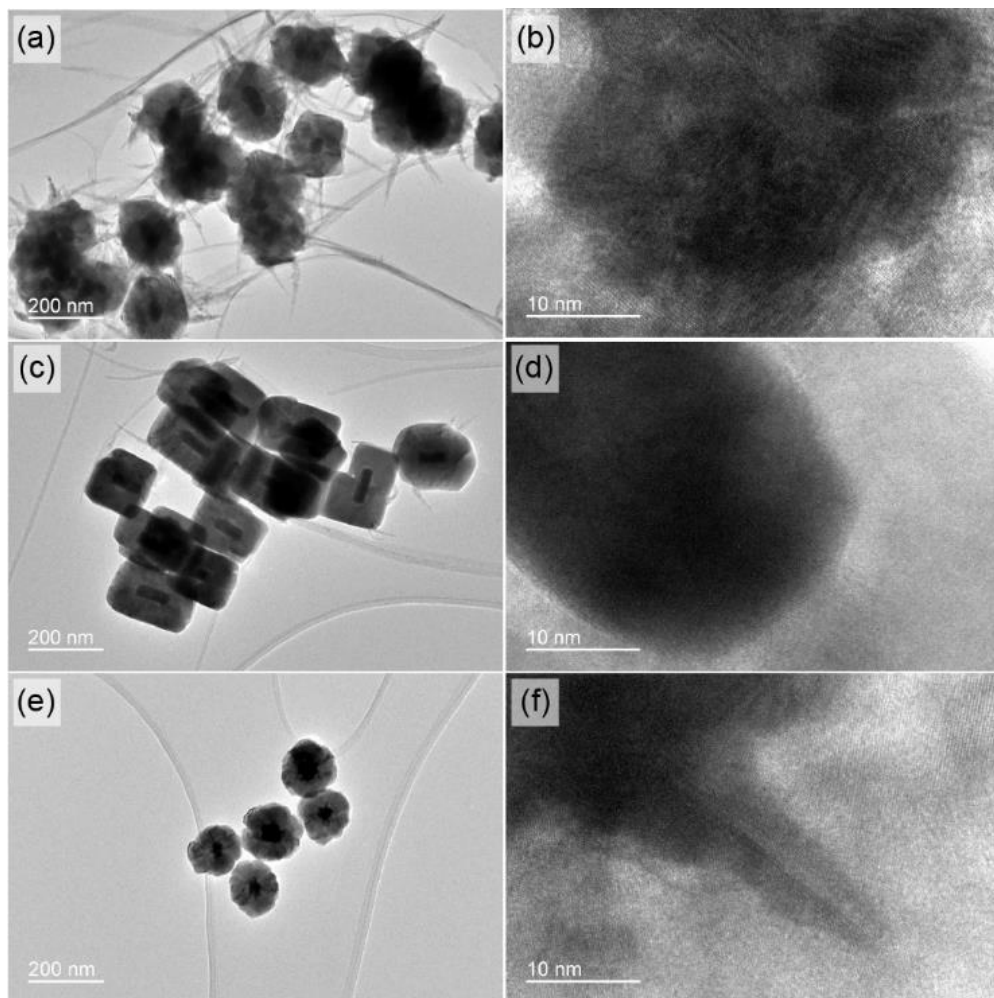


**Figure 5.4** low-resolution TEM images of (a) ACO-1, (c) ACO-2, (e) ACO-3 and corresponding high-resolution TEM images in (b), (d), (f).

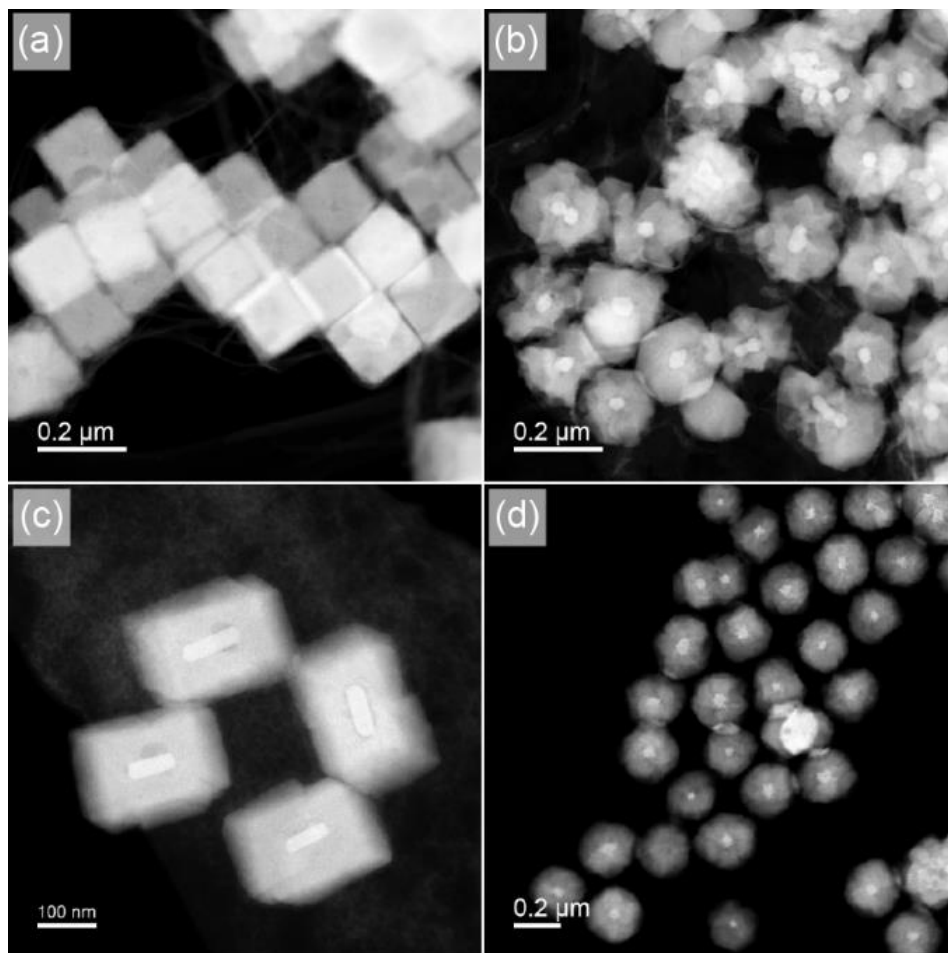


**Figure 5.5** HAADF-STEM images of (a)  $\text{Cu}_2\text{O}$  NC, (b) ACO-1, (c) ACO-2, and (d) ACO-3 nanoparticles.

### 5.2.2.3 Ultraviolet-visible absorption spectroscopy

The effect of Cu<sub>2</sub>O on the optical properties of Au was studied by UV–Vis absorption spectroscopy and the spectra are shown in Figure 5.6. The pristine Cu<sub>2</sub>O shows its characteristic absorption band at 490–500 nm and strong light scattering features in the range between 500 and 1,100 nm. This characteristic Cu<sub>2</sub>O absorption peaks were also observed from the Au–Cu<sub>2</sub>O core–shell nanoparticles at *ca.* 495 nm. The plasmon resonances at the nanoscale can be red-shifted as the refractive index of the surrounding medium increases.<sup>249</sup> Tens of nanometers redshift in SPR wavelength have been reported by coating plasmonic Au or Ag nanomaterials with a SiO<sub>2</sub> shell, simply attributed to the increased refractive index of SiO<sub>2</sub> ( $n = 1.43$ ) compared with that of H<sub>2</sub>O ( $n = 1.33$ ).<sup>250, 251</sup> The redshifted SPR peaks of the Au NPs are also found in Au–Cu<sub>2</sub>O core–shell nanostructures, due to the larger refractive index ( $n = 2.7$  above 600 nm)<sup>247</sup> of the Cu<sub>2</sub>O shell. The Au NP shows the absorption maxima at 540 nm, which is red-shifted to 650 nm after Cu<sub>2</sub>O coating. The coated Cu<sub>2</sub>O on Au NR introduces a split band in between 600 and 700 nm, which is known to be the scattering of the transverse SPR peak (515 nm) of Au NR by Cu<sub>2</sub>O.<sup>252</sup> At the same time, the longitudinal SPR peak of Au NR is red-shifted from 740 nm to near-infrared range. However, the Au NS characteristic absorption peak at 656 nm disappeared after Cu<sub>2</sub>O encapsulation, a new band at 610 nm related to the scattering of the ACO-3 appeared. The overall spectral features on the Au–Cu<sub>2</sub>O core–shell nanoparticles show a widened absorption range and weak SPR response from Au cores, attributed to the scattering effect of the thick Cu<sub>2</sub>O shell.<sup>248, 253</sup>

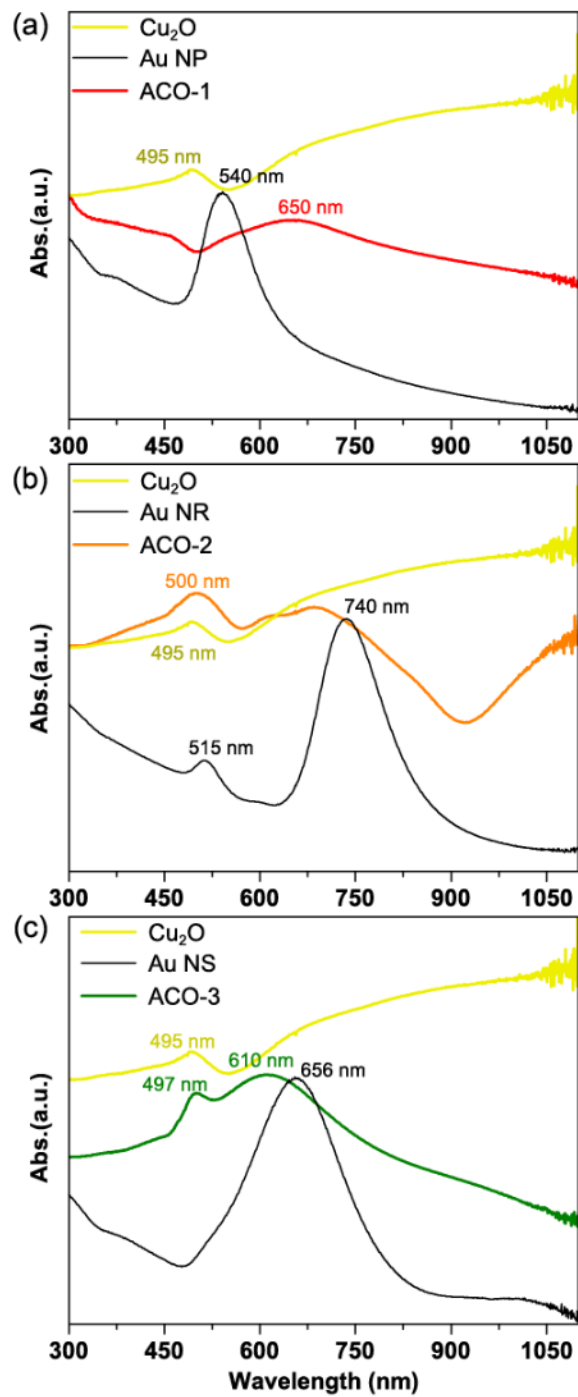


**Figure 5.6** UV-Vis spectra of Cu<sub>2</sub>O (yellow), Au with different shapes (black) and Au-Cu<sub>2</sub>O core-shell structures: (a) ACO-1 (red), (b) ACO-2 (orange) and (c) ACO-3 (green).

### 5.2.3 Au/copper sulfide yolk-shell nanostructure

#### 5.2.3.1 Powder X-ray diffraction

The  $\text{Cu}_2\text{O}$  surface can be transformed into copper sulfide by controlled sulfidation. The  $\text{S}^{2-}$  ions introduced first react with the surface  $\text{Cu}^+$  species of the  $\text{Cu}_2\text{O}$  to generate a thin sulfide layer which hindered further conversion of inner  $\text{Cu}_2\text{O}$  to sulfide. Therefore, a core-double shell Au- $\text{Cu}_2\text{O}$ /copper sulfide heterostructure is formed, which can be used to fabricate copper sulfide with hollow structure followed by the treatment with weak acid to remove the inner  $\text{Cu}_2\text{O}$ .

To study the crystalline structure and phase composition of the obtained Au-copper sulfides, powder XRD was employed and the patterns are shown in Figure 5.7. The XRD patterns of  $\text{Cu}_2\text{O}$  and bare copper sulfide (CS) are shown for comparison, which match well with cubic phase  $\text{Cu}_2\text{O}$  (No. 34-1354) and hexagonal phase  $\text{Cu}_{1.8}\text{S}$  (No. 47-1748), respectively. The Au- $\text{Cu}_{1.8}\text{S}$  products show two sets of patterns featured by characteristic peaks from (111), (200), and (220) lattice planes of hexagonal  $\text{Cu}_{1.8}\text{S}$  and (111), (200), and (220) lattice planes of face-centered cubic (fcc) Au, indicating that Au- $\text{Cu}_{1.8}\text{S}$  is only composed of Au and  $\text{Cu}_{1.8}\text{S}$ . The absence of  $\text{Cu}_2\text{O}$  peaks in Au- $\text{Cu}_{1.8}\text{S}$  spectra confirms that  $\text{Cu}_2\text{O}$  was completely removed. Also, the widened diffraction peaks in Au- $\text{Cu}_{1.8}\text{S}$  spectra suggest that the Au and  $\text{Cu}_{1.8}\text{S}$  are in nanocrystalline nature.<sup>254, 255</sup>

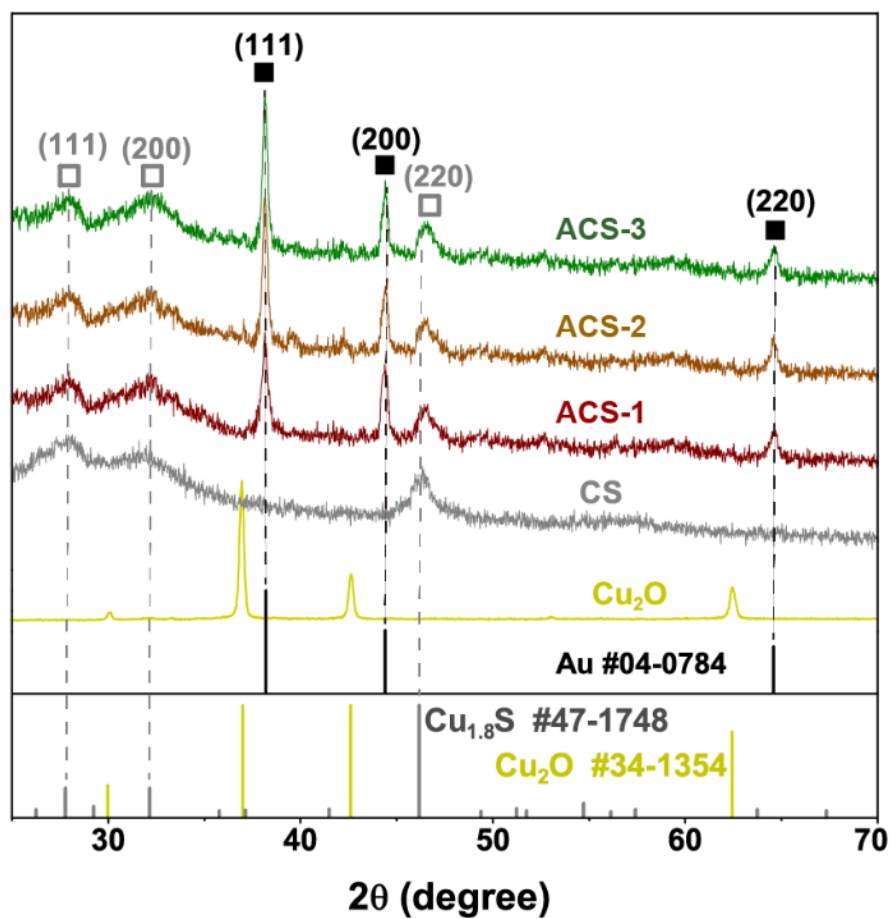


**Figure 5.7** Powder XRD patterns of Cu<sub>2</sub>O and Au-Cu<sub>1.8</sub>S system. The standard JCPDS XRD patterns for Au (No. 04-0784), Cu<sub>2</sub>O (No. 34-1354) and Cu<sub>1.8</sub>S (No. 47-1748) are shown at the bottom.

### 5.2.3.2 Transmission electron microscopy

Structures and geometries of the obtained Au-Cu<sub>1.8</sub>S nanoparticles are investigated by transmission electron microscopy (TEM), and the TEM images are shown in Figure 5.8. Distinguished void space with embedded Au nanoparticles for ACS-1, ACS-2, and ACS-3 can be clearly seen in Figure 5.8 (a), (c), and (e), respectively. All the three nanoparticles have a thin shell with thickness of  $6 \pm 1.2$  nm. The average sizes and cavity volumes of the yolk-shell nanoparticles are summarized in Table 5.1, which shows comparable sizes but different cavity volumes. The morphology of the yolk-shell nanoparticles is further confirmed by close-up views from Figure 5.8 (b), (d), and (f), showing preserved shapes of Au cores after removing Cu<sub>2</sub>O.

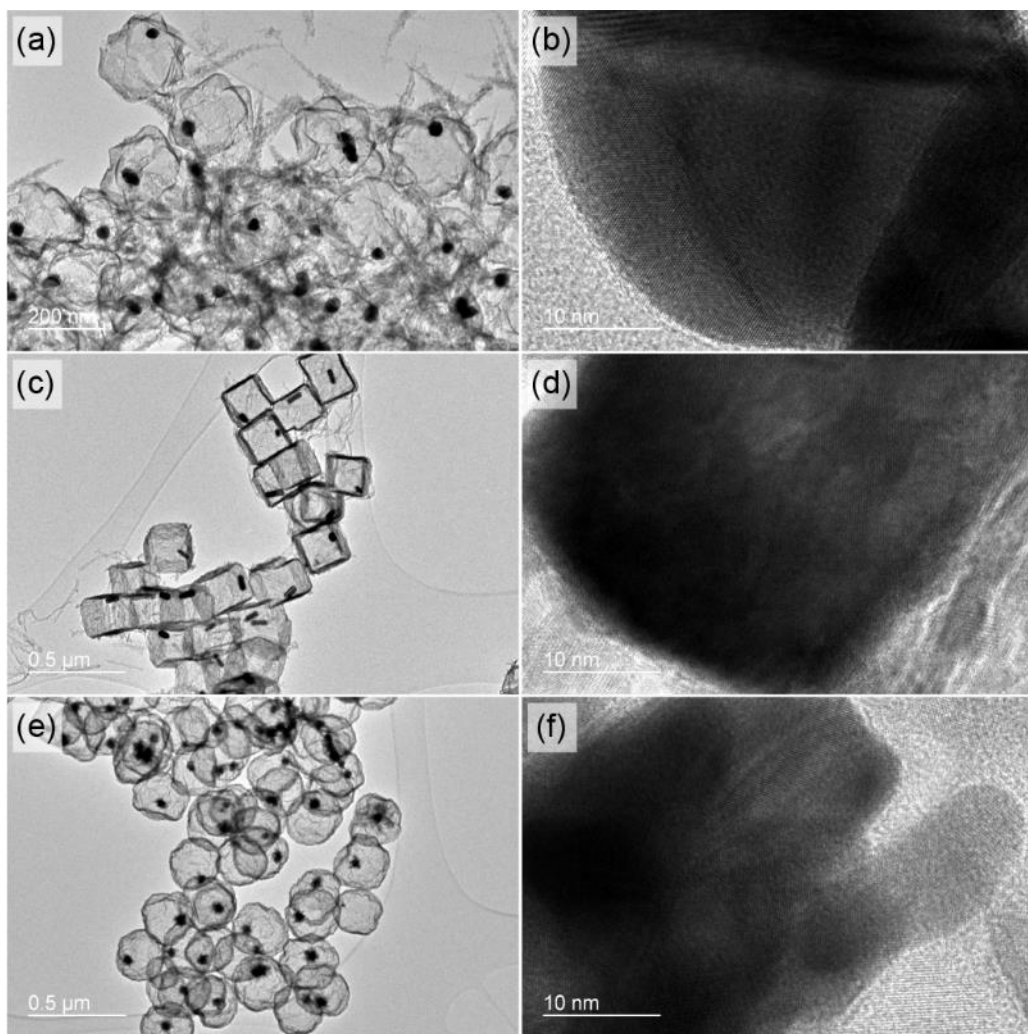


**Figure 5.8** Low-resolution TEM images of (a) ACS-1, (c) ACS-2, and (e) ACS-3. The corresponding high-resolution TEM images are shown in (b), (d), and (f).

**Table 5.1** Geometric dimensions of the Au-Cu<sub>1.8</sub>S system (*d*=diameter).

Sample	$d_{\text{Au}}$ (nm)	$d_{\text{overall}}$ (nm)	$d_{\text{cavity}}$ (nm)
ACS-1	45±5.8	206±5.7	ca.148
ACS-2	L: 77±4.6 W: 34±2.7	212±4.8	ca.129
ACS-3	67±10.6	208±7.2	ca. 118

### 5.2.3.3 Ultraviolet -visible absorption spectroscopy

The effects of  $\text{Cu}_{1.8}\text{S}$  HNG on the optical properties of Au were studied by UV-Vis absorption spectroscopy. The optical spectra of Au and CS are shown for reference in Figure 5.9. The increasing absorption of the CS after 700 nm is caused by the free carrier interband transitions from valence states to unoccupied states.<sup>211, 256</sup> The ACS-1 shows a much broader absorption band covering UV-Visible range compared with individual Au NP or CS, with the characteristic peak of Au NP at 530 nm redshifted to 630 nm. The dual SPR peaks of Au NR at 515 and 740 nm were slightly redshifted to *ca.* 525 and 798 nm respectively by the CS shell. The peak of Au NSs were further broadened and shows two absorption bands at 558 and 715 nm. This broadened absorption range can be related to the refractive index change from the CS shell.<sup>257, 258</sup> Obviously, different redshifts of absorption can be seen for the CS encapsulated Au NPs, probably due to the different levels of yolk-shell interactions. It is suggested that the altered absorption was not only caused by the yolk-shell interaction from SPR coupling, but also by the enhanced charge movement in the shell.<sup>259</sup> The distinctive optical properties of these Au nanomaterials encapsulated by  $\text{Cu}_{1.8}\text{S}$  are expected to play a crucial role on their photo-electric activity due to the enhanced light-absorption and surface-charge redistribution.

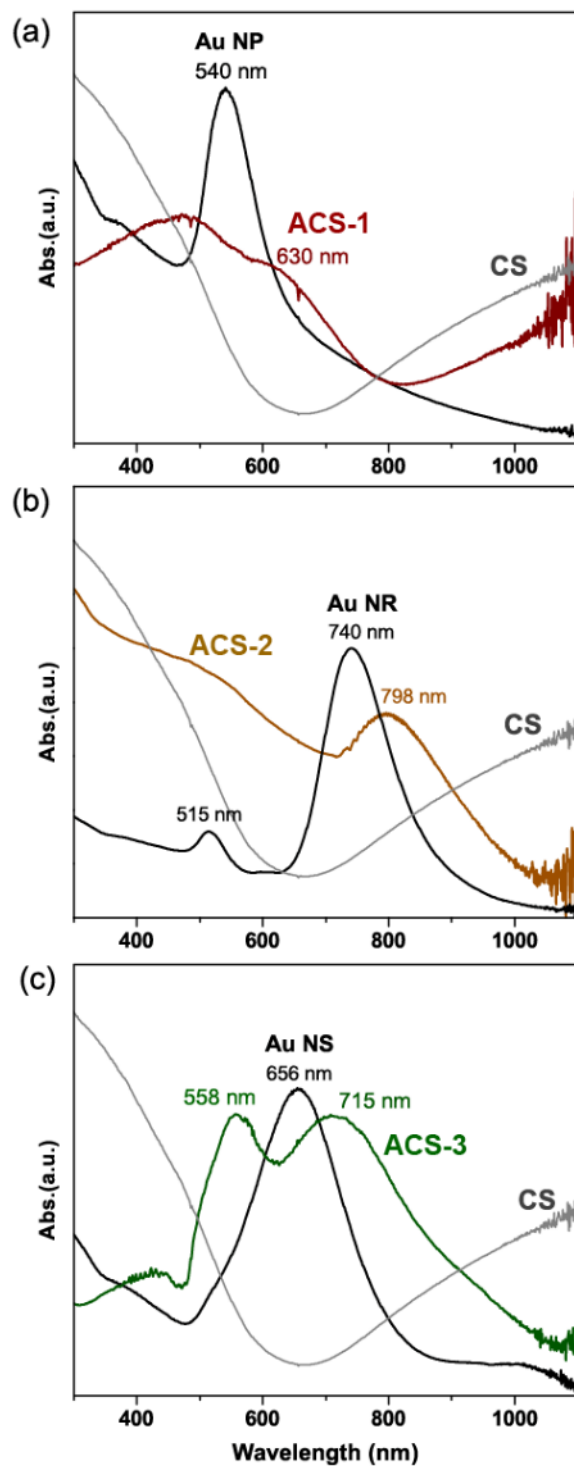


**Figure 5.9** UV-Vis spectra of the CS, different Au nanostructures and Au-Cu<sub>1.8</sub>S yolk-shell structures: (a) ACS-1, (b) ACS-2, and (c) ACS-3.

#### 5.2.3.4 Photocatalytic hydrogen evolution

With this metal-semiconductor hetero-nanostructure and improved light harvesting properties, it is of great interest to find out how these hetero-nanostructures affect the photocatalytic activity of the  $\text{Cu}_{1.8}\text{S}$ . The photocatalytic hydrogen evolution performance of hollow CS, ACS-1, ACS-2, and ACS-3 were evaluated under simulated sunlight (AM1.5) irradiation for 3 h, using three commonly-used sacrificial agents of 20 wt% methanol, 0.25 M  $\text{Na}_2\text{SO}_3$ , and 0.35 M  $\text{Na}_2\text{S} + 0.25$  M  $\text{Na}_2\text{SO}_3$  as hole scavengers. The  $\text{H}_2$  evolution rates of the catalysts were calculated by measuring the photogenerated hydrogen gas with gas chromatography (GC), and the results are shown in Figure 5.10. The pristine CS exhibited a higher photocatalytic activity for  $\text{H}_2$  generation ( $185.3 \mu\text{mol g}^{-1}\text{h}^{-1}$ ), for 0.35 M  $\text{Na}_2\text{S} + 0.25$  M  $\text{Na}_2\text{SO}_3$  than the other sacrificial agents. Significantly enhanced HER rates were achieved when plasmonic Au were embedded in the CS, generating  $\text{H}_2$  at the rates of 322.8, 381.3, and  $407.9 \mu\text{mol g}^{-1}\text{h}^{-1}$  for ACS-1, ACS-2, and ACS-3, respectively. These HER rates account for 174%, 205%, and 221% enhancement from the pristine CS, revealing a higher HER performance of ACS-3 among others. In a continuous 20 h reaction to test long term photo-stability of the ACS-3, no significant loss of activity was observed. Control work on HER was also carried out by bare Au nanomaterials and Au- $\text{Cu}_2\text{O}$  nanosystem, and neither of them were able to thermally generate  $\text{H}_2$  gas under the same conditions.

Photocatalytic HER by semiconductor materials is generally initiated by generating electron-hole pairs from excitation of semiconductors. However, the plasmon-enhanced HER by a plasmonic metal coupled with semiconductor is generally complicated. The mechanisms have been mainly explained by the Dexter energy transfer (DET), SPR induced local-field enhancement, and resonant energy transfer (RET) effects from the plasmonic core to the nearby semiconductor.<sup>138</sup> Herein, basic aspects are identified to explain the enhancement in the photocatalytic performance of the Au-Cu<sub>1.8</sub>S yolk-shell system. Firstly, light absorption can be enhanced by the SPR-induced field of Au, combined with the light multi-scattering in-between the yolk and shell and the multi-reflection in the void (shown in Scheme 5.2 (a)),<sup>209, 239</sup> promoting the generation of electron-hole pairs in the shell.<sup>257</sup> However, with only minimal metal-semiconductor contact, the transfer of hot electrons (or DET) from the excited Au core to the shell could be negligible for the reaction.<sup>260</sup> Thus, the RET mechanism which does not require direct contact may be in force to facilitate the photogeneration of charge carriers in the shell induced by the dipole transition of the Au core,<sup>138, 244, 261</sup> as shown in Scheme 5.2 (b). Furthermore, Au with different numbers of hot-spots, can lead to different levels of improvement in photocatalytic activity, because photon absorption is known to be proportional to the electric field squared ( $|E|^2$ ) from Au.<sup>262</sup> In addition, the thin shell (~5 nm) may work as an electron sink that retards the direct recombination of photogenerated charge carriers, thus improving the efficiency of photocatalytic reaction. On the

other hand, the holes react with the sacrificial agent polysulfide ( $S^{2-}+SO_3^{2-}$ ) to yield  $S_2O_3^{2-}$  thus complete the photocatalytic redox reaction.

Different cavity volume can affect the photocatalytic HER performance for yolk-shell photocatalysts, therefore the size range of the inner cavity and the Au core geometry should be discussed. The hollow voids are proven to benefit the photochemical reaction due to the enhanced light harvesting by multiple reflection and scattering. However, large cavity size can also increase the possibility of charge recombination because of the longer pathway for resonant energy transfer to semiconductor surface,<sup>263</sup> thus leading to a poorer photocatalytic activity. Thus, stronger SPR effects from Au cores with a larger size and multiple hot-spots are known to promote the photogeneration of electron-hole pairs in the nearby semiconductor, and is a crucial factor to enhance the photocatalytic activity.<sup>135</sup> Besides, semiconductors with a thin shell ( $\leq 10$  nm) are generally favorable to the reactive species diffusion compared with a thicker one,<sup>209</sup> which can effectively promote the efficiency of photocatalytic reaction. Thus, the geometry of Au-Cu<sub>1.8</sub>S yolk-shell system should be tailored to balance the different dimensions of cavity size, shell thickness and Au core geometries. ACS-3 which has a larger size (*ca.* 67 nm), multiple hot-spots and a smaller cavity volume (diameter *ca.* 118 nm), exhibits the highest photocatalytic activity among all the samples studied.

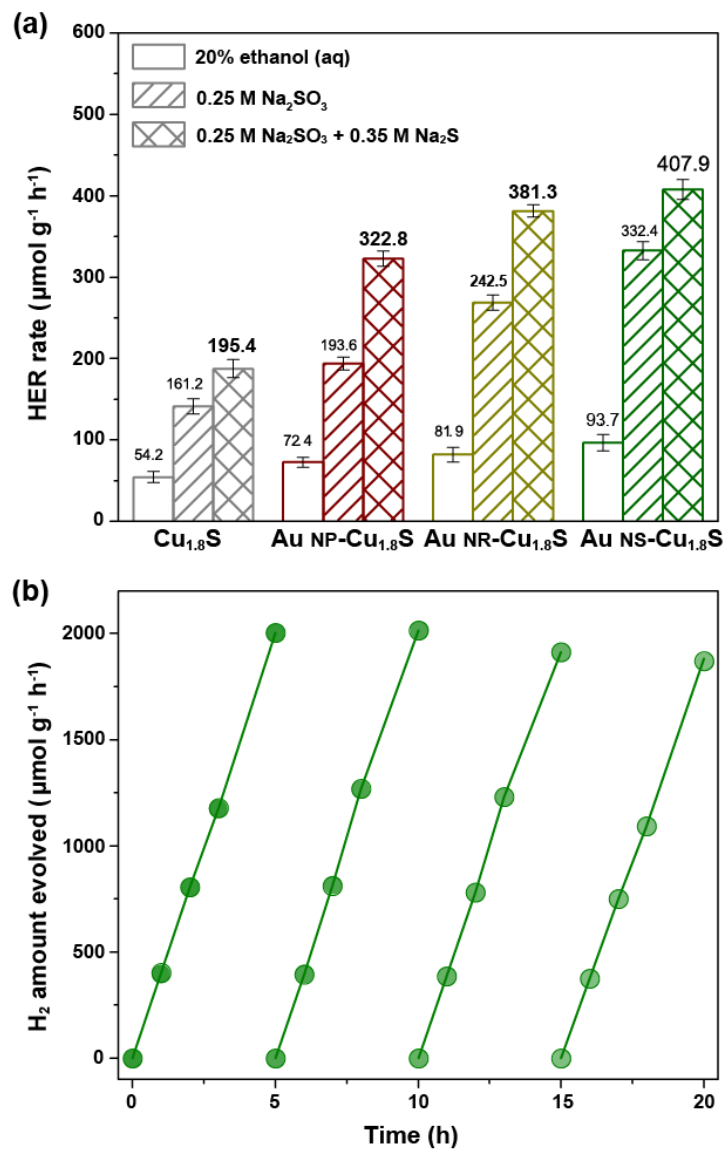
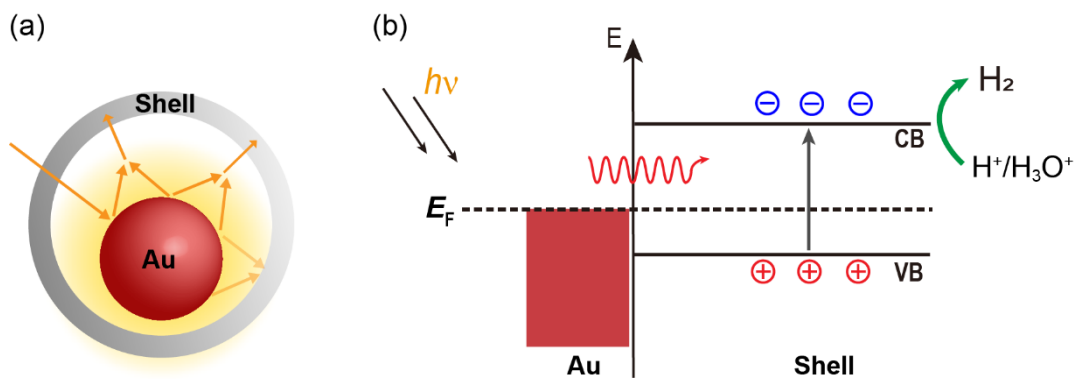


**Figure 5.10.** (a) A comparison of photocatalytic hydrogen evolution reaction rates among CS, ACS-1, ACS-2, and ACS-3 using different sacrificial agents. (b) Stability test for photocatalytic cycles of ACS-3 in the time course of 20 h. All measurements were carried out with a  $100 \text{ mW cm}^{-2}$  solar simulator.



**Scheme 5.2** (a) Multiple light scattering and reflections in the void of Au-copper sulfide yolk-shell nanostructure; (b) Enhanced photogeneration of charge carriers in the shell by the resonant energy transfer from the Au core.

### 5.3 Concluding remarks

Theoretically, photoexcited plasmonic metal can inject electrons to the conduction band (CB) of semiconductors, which can be utilized for proton reduction reactions. A yolk-shell hetero-nanostructure was constructed by embedding plasmonic Au nanomaterials into hollow  $\text{Cu}_{1.8}\text{S}$ . The resulted Au- $\text{Cu}_{1.8}\text{S}$  dual plasmonic nanosystem enables localized surface plasmonic resonance coupling between Au and  $\text{Cu}_{1.8}\text{S}$ , promoting photogeneration of charge carriers useful for photochemical reaction. However, without significant metal-semiconductor contact, the transfer of hot electrons from the excited Au core to the shell should have a minimal contribution to the photocatalytic reaction. Therefore, the resonance energy transfer process from the excited Au core by a dipole-dipole transition works to induce electron-hole pair generation in the  $\text{Cu}_{1.8}\text{S}$  shell. And the hetero-structured Au- $\text{Cu}_{1.8}\text{S}$  nanosystem demonstrated significant enhancement of photochemical activity in the photocatalytic hydrogen evolution from water. Noticeably, a random mixture of Au nanoparticles and the  $\text{Cu}_{1.8}\text{S}$  shows weak photo-conversion to hydrogen, arising from the weak plasmonic interaction between the two components. A synergistic effect from the localized surface plasmonic resonance coupling and resonant energy transfer process is investigated by a catalyzed hydrogen evolution reaction on the Au- $\text{Cu}_{1.8}\text{S}$  yolk-shell nanosystem.

## **Chapter 6**

### **Au Nanorod as Antenna on Copper Sulfide Nanocage for Plasmon-enhanced Photocatalytic Water Reduction to Hydrogen**

## 6.1 Introduction

Plasmonic nanostructures have become an important research topic in photocatalysis due to their intrinsic properties such as intense electromagnetic field, efficient light-to-energy conversion, and abundant hot electron generation.<sup>228, 264</sup> Among them, hot electrons produced by Landau damping of localized surface plasmon resonance (LSPR) from Au, Ag or Cu nanoparticles (NPs) have received wide attention for their potentials in promoting chemical transformations by light-to-energy conversion.<sup>265, 266</sup> To date, low efficiency of using hot electrons from plasmonic metallic nanomaterials has become one of the major concerns for further development of the plasmon-enhanced catalytic systems. The injection of hot electrons into reactants can be hindered by the chemically inert surface of plasmonic metal NPs, which would lower their engagement in catalytic activities.<sup>267</sup> Also, the generated hot electrons are cooled by ultrafast electron–phonon scattering before being transferred to the catalytically active sites<sup>268</sup>, resulting in undesired energy dissipation. To this end, attaching the plasmonic metal to semiconductors by constructing a supramolecular assembly with intimate interfaces is recognized as an effective approach to facilitate hot electron transfer and utilization.<sup>269</sup> The hetero-nanostructures obtained in such a way are reported to have unique and useful capabilities, such as surface plasmon-enhanced absorption, plasmon-induced resonance energy transfer (PIRET), and plasmon-excitation from enhanced local electric field.<sup>131</sup>

Generally, three approaches have been developed to construct the plasmonic metal-semiconductor hybrid photocatalysts. One is to decorate the plasmonic metal NPs on the semiconductor surface in which the plasmonic metal NPs work as the light-harvesting antenna and electron transfer promoter, thus improving their photocatalytic activity.<sup>270-272</sup> The second one is the plasmonic metal-semiconductor core-shell hetero-structured photocatalyst in which the interfacial charge transfer from metal to semiconductor can be much facilitated by largely extended contact area.<sup>35</sup> The third one is the construction of multiple interfaces between plasmonic metal NPs and semiconductor nanomaterials, thus facilitating photogenerated charges transport to the semiconductor surface for reaction.<sup>273, 274</sup> For better photocatalytic performances, efficient separation and transport of electron-hole pairs are often required on the hetero-structured photocatalysts, making the rational design of structures imperative and challenging.

Herein, we present a novel hetero-nanostructure of Au nanorod (NR) and hollow copper sulfide (CS) for plasmon-enhanced photocatalytic hydrogen evolution reaction (HER). Along the long axis of the plasmonic Au NRs, multiple CS hollow nanocages (HNGs) are attached to form heterojunctions at the metal/semiconductor interface. By such interfaces, concentration of charge carriers on the CS is enhanced by the excited Au, which works as a light antenna. Besides, the CS HNGs enable multiple reflections of the incident light within the hollow void, increase the light harvesting and promote the photogeneration of charge carriers. Electrons migrated out to the CS surface, on which molecular H<sub>2</sub>

is evolved by proton reduction reaction. This hetero-nanostructure makes a novel plasmon-enhanced photocatalytic supramolecular assembly for hydrogen generation from water.

## 6.2 Results and discussion

### 6.2.1 Powder X-ray diffraction

The Au-copper sulfide hetero-structured nanoparticle was prepared using a three-step approach. The details are presented in the section 2.2.4. of the chapter 2 and a schematic diagram of the synthetic procedure is shown in Scheme 6.1. Firstly, pre-prepared Au nanorods (NRs) were mixed with  $\text{Cu}^{2+}$  and hydroxylamine to form  $[\text{Cu}(\text{NH}_2\text{OH})]^{2+}$ , which was *in situ* initiated to form  $\text{Cu}_2\text{O}$  nuclei on-rod (ACO) by adding  $\text{OH}^-$  and quenched shortly, then Au- $\text{Cu}_2\text{O}$  (i-ACO) was obtained. Secondly, the i-ACO was cooled to 0 °C then treated by  $\text{S}^{2-}$  ions to convert the surface of  $\text{Cu}_2\text{O}$  into sulfide shell (ACOS). Finally, dilute HCl was used to etch the  $\text{Cu}_2\text{O}$  core until a dark brown product was yielded, which is labeled as i-ACS.

To investigate the crystalline structure and phase composition, powder X-ray diffraction (XRD) was employed and the patterns are shown in Figure 6.1. The XRD patterns of  $\text{Cu}_2\text{O}$  and copper sulfide (CS) are shown for comparison, both of which match well with cubic phase  $\text{Cu}_2\text{O}$  (No. 34-1354) and hexagonal phase  $\text{Cu}_{1.8}\text{S}$  (No. 47-1748), respectively. The as-prepared i-ACS shows two sets of

patterns featured by characteristic peaks from (111), (200), and (220) lattice planes of hexagonal  $\text{Cu}_{1.8}\text{S}$  and (111), (200), and (220) lattice planes of fcc Au, clearly indicating that the i-ACS is composed of Au and  $\text{Cu}_{1.8}\text{S}$ . The absence of  $\text{Cu}_2\text{O}$  peaks in the diffraction pattern of the i-ACS confirms that  $\text{Cu}_2\text{O}$  was completely removed. Also, the widened diffraction peaks in the i-ACS spectra suggest that the Au and  $\text{Cu}_{1.8}\text{S}$  crystallites are in nanocrystalline nature.<sup>254, 255</sup>



**Scheme 6.1** Schematic synthetic procedure of Au-Cu<sub>2</sub>O and Au-copper sulfide hetero-nanostructures.

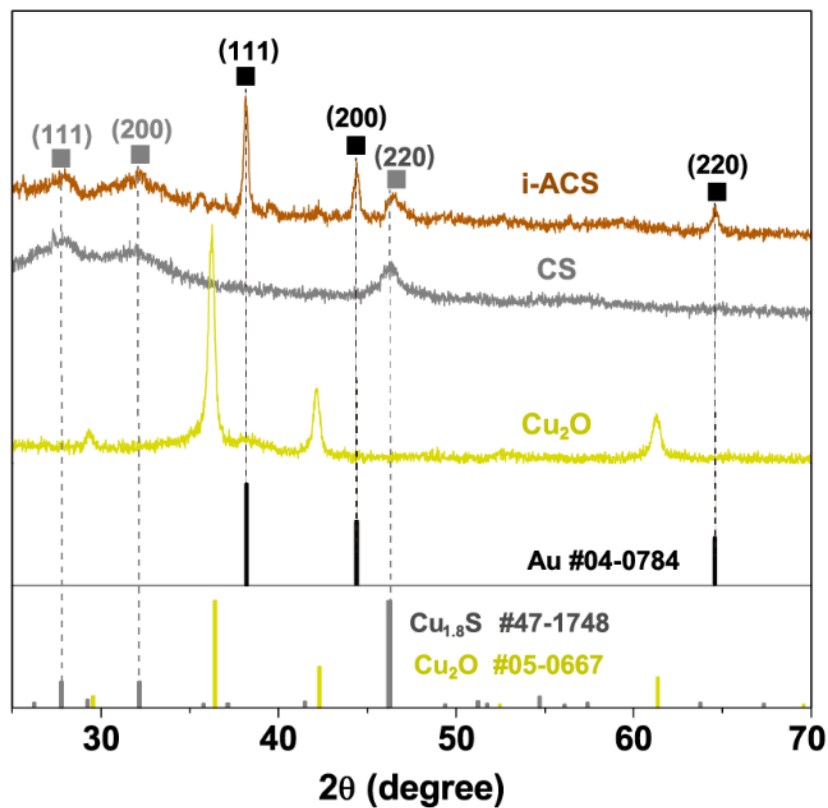


**Figure 6.1** The powder XRD patterns of i-ACS (brown), Cu<sub>2</sub>O (yellow), and CS (grey). The standard JCPDS XRD patterns for Au (No. 04-0784), Cu<sub>2</sub>O (No. 34-1354) and Cu<sub>1.8</sub>S (No. 47-1748) are shown at the bottom.

## 6.2.2 Transmission electron microscopy

The nanostructures of the as-obtained samples i-ACO, i-ACS are studied by transmission electron microscopy (TEM) and shown in Figure 6.2 and 6.3, respectively. From the low-resolution TEM images in Figure 6.2 (a) and (b), a hetero-nanostructure composed of Au NR and Cu<sub>2</sub>O nanocube (NC) can be clearly seen. The inner Au NRs have a regular shape with an average length of  $74 \pm 4.8$  nm and a diameter of  $32 \pm 2.7$  nm with an aspect ratio of *ca.* 2.3. The Au NRs are decorated by Cu<sub>2</sub>O NC that have an average side length of *ca.* 20 nm. Close-up views shown in Figure 6.2 (c) and (d) further reveal that two components form close interfacial contacts, which is associated with the nucleation of Cu<sub>2</sub>O on the surface of Au NR due to a small lattice mismatch (0.0189 nm) between Au (*a*=0.408 nm) and Cu<sub>2</sub>O (*a*=0.427 nm).<sup>252</sup> The characteristic *d*-spacing fringes of 0.20 nm can be assigned to the (200) plane of Au, whereas those of 0.30 and 0.25 nm are assigned to the (110) and (111) planes of Cu<sub>2</sub>O, respectively, confirming their crystalline nature. From the TEM images, the Cu<sub>2</sub>O NCs are much smaller than Au NRs, and multiple Cu<sub>2</sub>O NCs are decorated along the longer side of Au NRs. The decorated Cu<sub>2</sub>O NCs, however, are not completely covering the Au NR, exposing unmodified Au surface.

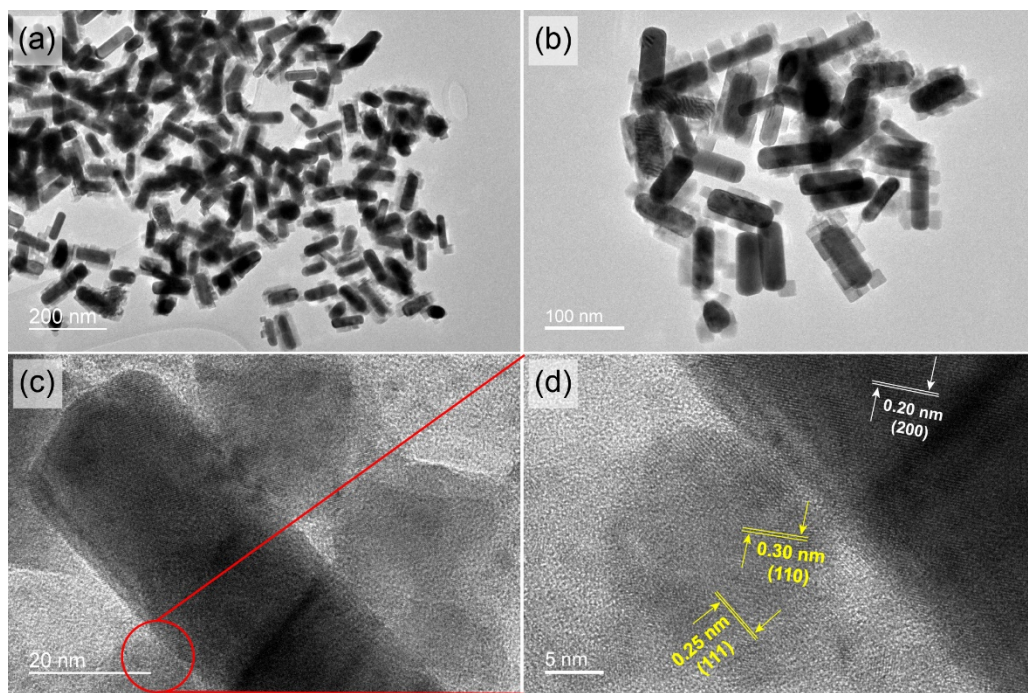


**Figure 6.2** (a) low- and (b) mid-resolution TEM images of i-ACO; (c) high-resolution TEM image of an individual i-ACO nanostructure (d) close-up image of the area in (c) indicated with a circle.

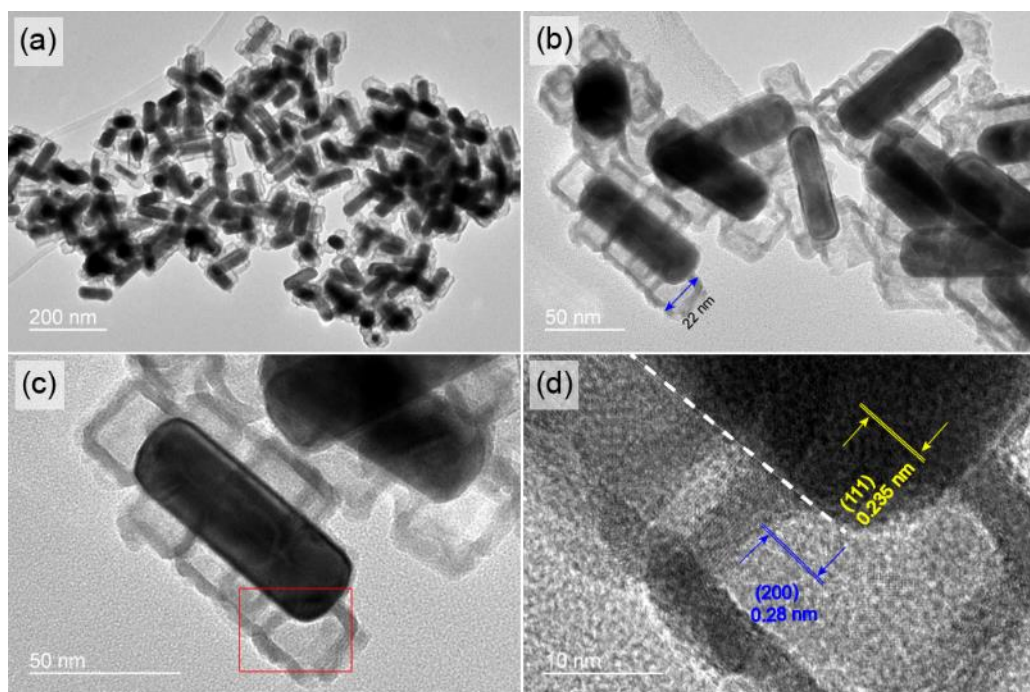


**Figure 6.3** (a) low- and (b) mid-resolution TEM images of i-ACS; (c) high-resolution TEM image of a single i-ACS nanostructure; (d) close-up image of the area in (c) indicated with a rectangle.

Surface sulfidation provides a direct way of constructing thin copper sulfide layer on the  $\text{Cu}_2\text{O}$  core. The thin sulfide layer can be easily obtained by removing  $\text{Cu}_2\text{O}$  core and the resulted hetero-nanostructure of i-ACS is revealed by TEM images in Figure 6.3 (a) and (b). Similar to the i-ACO nanoparticles, the Au NRs are decorated with multiple hollow nanocages (HNGs) (appear in lighter contrast), forming a unique and uniform hetero-nanostructure. After sulfidation, the dimensions of Au NR are maintained while the size of the HNG is slightly larger (*ca.* 22 nm) than  $\text{Cu}_2\text{O}$ . The increased size of CS HNG is related to the bigger radii of  $\text{S}^{2-}$  ion (184 pm) than  $\text{O}^{2-}$  ion (140 pm).<sup>275</sup> High-resolution TEM images shown in Figure 6.4 (c) and (d) further reveal the intimate interfacial contacts between CS HNG and Au NR, as well as among neighboring CS HNGs, indicating their multiple contacts. This hetero-nanostructure possesses a combination of Au-CS heterojunction and CS HNGs homojunction. Characteristic *d*-spacing fringes of 0.235 nm from the (111) plane of Au and 0.32 nm from the (111) plane of CS indicate their crystalline natures, which is in good agreement with their powder X-ray diffraction patterns.

### 6.2.3 Energy-dispersive X-ray spectroscopy

The nanostructures of i-ACO and i-ACS are also verified by high-angle annular dark-field scanning transmission electron microscopy (HAADF-STEM) measurement. As shown in Figure 6.4 (a) and (b), the HAADF-STEM image of the i-ACO shows a bright Au nanorod and a less bright  $\text{Cu}_2\text{O}$  NC. The contrast in brightness is related to different electrons scattering capability of component

elements.<sup>252</sup> The composition distribution was analyzed by energy-dispersive X-ray spectroscopy (EDX) and the elemental mapping images are shown in Figure 6.4 (c). The Au elements display as a rod core while distribution of Cu elements covers a wide area that overlaps with O elements, further confirming the hetero-nanostructure of multiple Cu<sub>2</sub>O NCs decoration on single Au NR.

However, the identification of CS phase in the hetero-structure is difficult, possibly due to the poor crystallinity of CS induced by a relatively low reaction temperature and the heavy metal effect of Au. To further confirm the composition and structure of the hetero-structure, HAADF-STEM was undertaken to investigate the elemental distributions in i-ACS, shown in Figure 6.5 (a) and (b). Localized distributions of Cu and S elements can be clearly seen from 6.5 (c), which do not overlap with those of Au, indicate that the CS is located around Au and do not encapsulate Au nanorod.

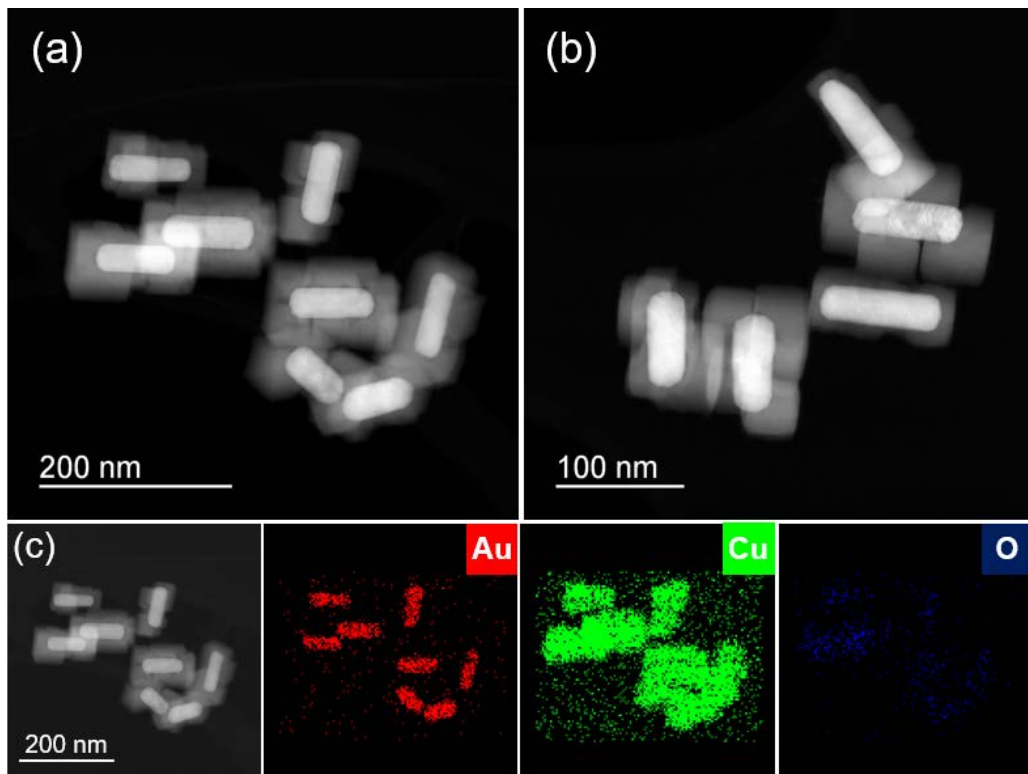


**Figure 6.4** (a) and (b) HAADF-STEM images of i-ACO viewed at different directions and (c) EDX elemental mapping of Au, Cu and O elements from the i-ACO hetero-nanostructure.

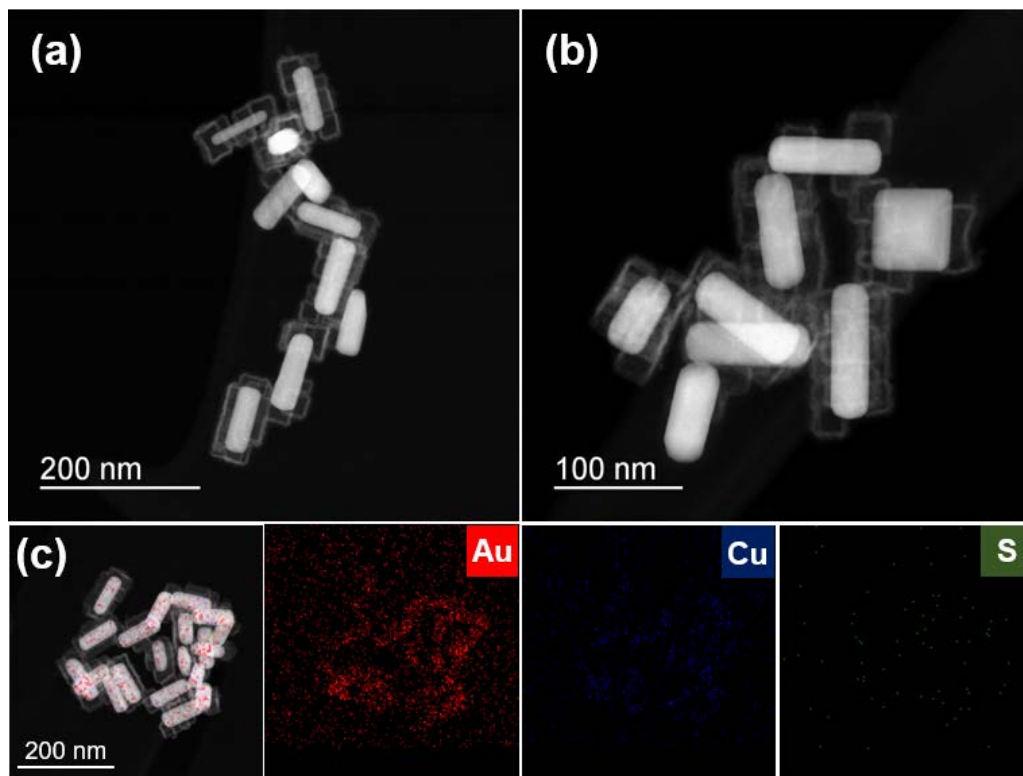


**Figure 6.5** (a) and (b) HAADF-STEM images of i-ACS viewed at different directions and (c) EDX elemental mapping of Au, Cu and S elements from the i-ACS hetero-nanostructure.

#### 6.2.4 Ultraviolet-visible absorption spectroscopy

The effects of Cu<sub>2</sub>O NCs and CS HNGs on the optical properties of Au NR were studied by UV–Vis absorption spectroscopy. Firstly, the optical properties of Cu<sub>2</sub>O NC and CS HNG are evaluated for reference and shown in Figure 6.6 (a). The Cu<sub>2</sub>O shows its characteristic absorption band at 470–480 nm and strong light scattering features in the range between 500 and 1,100 nm, while CS HNG displays an absorption cut-off at *ca.* 607 nm with a broad tailing from 680 to 1,100 nm. The tailing observed from CS HNG suggests the strong LSPR effect from the surface with high density of holes due to Cu vacancies.<sup>276</sup>

The Au NR shows its characteristic transverse and longitudinal SPR absorption peaks at 515 and 740 nm, respectively. Decoration of Au NR with Cu<sub>2</sub>O NCs and CS HNG induced significant changes on the optical properties of Au NR, as shown in Figure 6.6 (b). The Cu<sub>2</sub>O on-rod broadened both the transverse and longitudinal SPR bands of Au NR, which were red-shifted to 584 and 970 nm respectively, because of the increased refractive index ( $n = 2.7$  above 600 nm)<sup>247</sup> and dielectric constant ( $\epsilon = 7.2$ )<sup>277</sup> of Cu<sub>2</sub>O surrounding Au. The peak at *ca.* 470 nm indicates the presence of Cu<sub>2</sub>O from its scattering effect. On the other hand, the decorated CS HNG slightly redshifted the transverse absorption of Au NR to 545 nm and broadened the absorption spectrum to cover the near infrared (NIR) range. It is related to the refractive index change originated from LSPR surface attached to Au longitudinal sides.<sup>257, 258</sup> Furthermore, the broadened absorption to NIR can be arising from the collective oscillation of charge carriers by the

LSPR coupling of metal and semiconductor, suggesting the accumulated charges on the hetero-structured nanoparticle. The interplay in the Au–Cu<sub>1.8</sub>S provides a new means of engineering the light absorption by charge redistribution on the hetero-nanostructure.

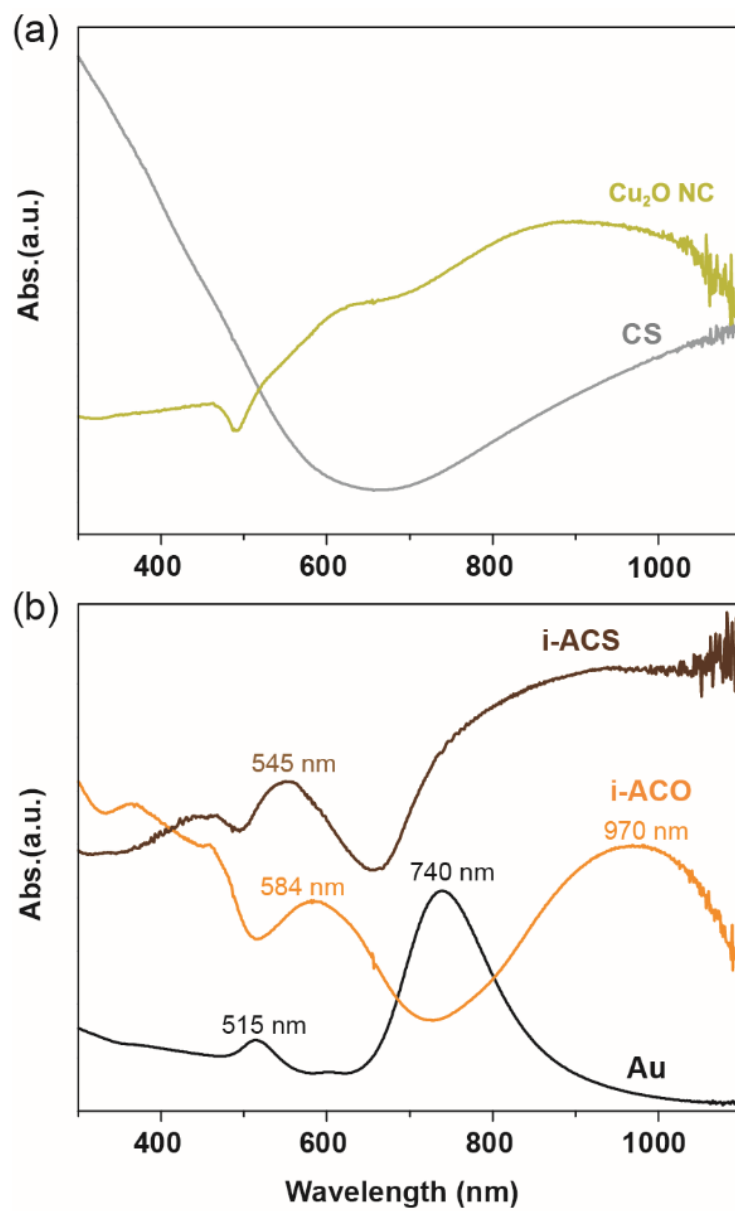


**Figure 6.6** UV-Vis-NIR spectra of (a)  $\text{Cu}_2\text{O}$  NC (yellow) and CS HNG (grey); (b) Au NR (black), i-ACO (orange) and the i-ACS hetero-nanostructure (brown).

### 6.2.5 Photocatalytic hydrogen evolution

With this unique metal-semiconductor arrangement and improved light harvesting properties, it is of much interest to see how this hetero-nanostructure affect the light-matter interaction by evaluating photocatalytic activity of the CS HNG. The photocatalytic HER was carried out under simulated solar illumination using 0.35M Na<sub>2</sub>S+0.25M Na<sub>2</sub>SO<sub>3</sub> solution as sacrificial agent and the results are summarized in Figure 6.7 (a). The CS HNG showed a photocatalytic HER rate of 185.3  $\mu\text{mol g}^{-1}\text{h}^{-1}$ , which is expected for its improved light absorption due to the hollow interior. Significantly enhanced HER rate was achieved when CS HNG were decorated on Au NR, generate H<sub>2</sub> at the rates of 281.9  $\mu\text{mol g}^{-1}\text{h}^{-1}$ , which account for 152% enhancement from single CS HNG. This can outperform most of the literature reported copper sulfide-based photocatalytic systems for HER under simulated sunlight (Table 6.1). In photocatalytic reaction for continuous 20 h, no significant loss of activity of the CS HNG and i-ACS was observed from Figure 6.7(b), which demonstrate their photo-stabilities.

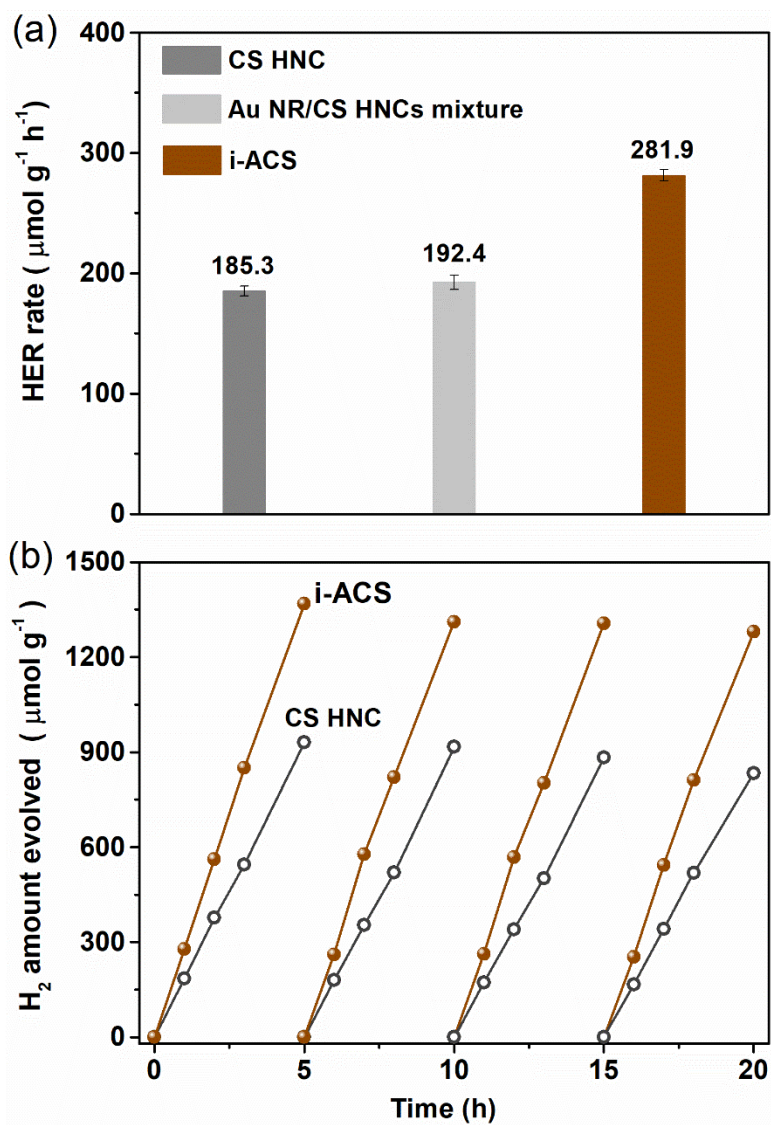


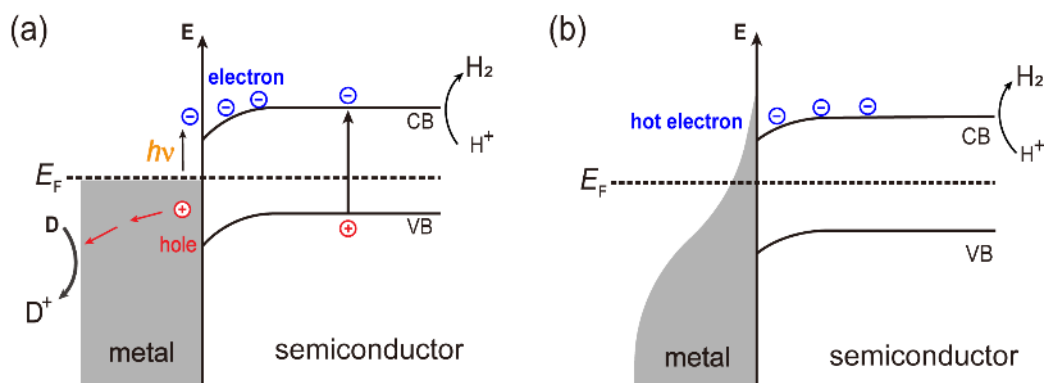
**Figure 6.7** (a) Photocatalytic hydrogen evolution rates of CS HNC, a mixture of Au NR and CS HNC, and i-ACS and (b) their stability test for photocatalytic 4 cycles. All measurements were carried out using a  $100 \text{ mW cm}^{-2}$  solar simulator.

**Table 6.1** A summary of copper sulfides photocatalysts for HER

Photocatalyst	HER rate ( $\mu\text{mol g}^{-1}\text{h}^{-1}$ )	Irradiation	Size	Hole scavenger	Ref.
Cu <sub>9</sub> S <sub>5</sub>	380	300 W	~500 nm		30
Cu <sub>7</sub> S <sub>4</sub>	128	100 mW cm <sup>-2</sup> ; simulated sunlight	~100 nm		29
Cu <sub>1.94</sub> S	11	300 W; visible light	200~300nm	Na <sub>2</sub> S/Na <sub>2</sub> SO <sub>3</sub>	202
Cu <sub>x</sub> S hollow cube	237.5	300 W	450±72 nm		278
Cu <sub>1.8</sub> S HNG	185.3	100 mW cm <sup>-2</sup> ; simulated sunlight	~100 nm		This
i-ACS	281.9		~100 nm		work

Photocatalytic HER of semiconductor generally involves two basic processes initiated by band gap excitation of semiconductor, which produces the excited electron-hole pairs. The electrons then migrate to the semiconductor surface for proton reduction reaction, whereas the holes diffuse out to react with electron donor to complete the redox reaction. Plasmon energy transfer from Au nanostructures to semiconductor is known to promote the photogeneration of charge carriers<sup>279</sup> in semiconductor and facilitate the charge carriers separation.<sup>273, 280</sup> The i-ACS hetero-nanostructure constructed by longitudinal decoration Au NRs with multiple CS HNGs, possess multiple metal/semiconductor heterojunctions,<sup>281</sup> that induce the downward bending energy band for *p*-type semiconductor<sup>282, 283</sup>, as shown in Scheme 6.2. Such close attachment and multiple interfacial contacts enable the plasmon excited hot electrons of Au to be easily injected on the semiconductor, enhancing the concentration of charge carriers on the CS HNG.<sup>131</sup> In addition, multiple light reflections within the hollow interior is known to improve light absorption<sup>30</sup> and localization of photogenerated charge carriers<sup>209</sup>. Such dual effect helps the charge localization at the interfaces, thereby facilitating charge separation and movement toward opposite directions.<sup>284</sup> Consequently, the electrons migrate out to the CS surface on which to react with adsorbed protons for molecular H<sub>2</sub> generation, while hole-diffusion is driven to the Au to achieve thermal equilibrium.<sup>283, 285</sup> The photogenerated holes trapped by the Au can react with incoming electron donors ( $S^{2-} + SO_3^{2-}$ ) on the exposed area,<sup>286</sup> further assisting the charge separation to complete the catalytic cycle. The attachment of hollow

semiconductor to plasmonic metal nanomaterial offers an effective approach to improve photocatalytic HER performance by synergistic interactions between both components.



**Scheme 6.2** Schematic illustration of the two mechanisms for plasmon-enhanced photocatalytic HER by the plasmonic metal-semiconductor hetero-nanostructure. (a) Plasmon excitation and (b) hot-electron effect. The CB and VB are the conduction band and valence band of the semiconductor, respectively.  $E_F$  refers to the Fermi energy level. D and  $D^+$  are electron donor and oxidized electron donor, respectively.

### 6.3 Concluding remarks

A novel hetero-nanostructure based on the Au nanorods (average length = *ca.* 78.7 nm, average width = *ca.* 35.2 nm) decorated with Cu<sub>1.8</sub>S nanocages (average size = *ca.* 20.3 nm) was synthesized using a precursor, the Cu<sub>2</sub>O nanocube decorated Au nanorods. The plasmonic properties of Au nanorods were enriched by the dielectric property of decorated semiconductor nanomaterials. Discontinuous gaps were formed between the Au and Cu<sub>1.8</sub>S, as verified by HAADF-STEM images and could be resulted from the uneven distribution of precursor Cu<sub>2</sub>O nanocubes on the Au nanorod surface. With the intimate contacts between Au and Cu<sub>1.8</sub>S and the multiple reflections and scatterings of incident light within the hollow interior of Cu<sub>1.8</sub>S nanocages, a significant enhancement (152%) on HER activity of the Cu<sub>1.8</sub>S was achieved under simulated sunlight. The highlight of this unique heterostructure is two-fold: the antenna effect of the Au nanorod improves the photogeneration of electrons for reduction reaction; and the exposed area on the Au nanorod facilitates the separation of photogenerated charge carriers. Our study provides a pathway to utilize the plasmonic effect of metal nanoparticles by decorating them with semiconductor nanomaterials into rationally designed nanoarchitectures. The results also put an insight into the plasmonic properties of metal–semiconductor hetero-nanostructures for potential applications in photocatalysis and solar-energy conversion.

## **Chapter 7**

### **Conclusions and Future Research Directions**

Interface engineering on semiconductor nanomaterials has shown its importance in optimizing the photocatalytic performances. The interface between two component nanomaterials can provide the facilitated charge separation and transfer in hybrid or heterogeneous nanostructures. Theoretically, the internal electric field established at the interface offers a driving force for directional separation of photogenerated electrons and holes for reduction and oxidation reactions on the surface, respectively. Besides, the surface compositions, crystal phases, lattice vacancies, and energy band alterations determine the catalytic activity and selectivity because the surface adsorption and activation of the reactants are dictated by the combination of these factors. In this thesis, interface engineering on two kinds of candidate metal sulfide photocatalysts were examined to understand the implication of interfaces for photocatalysis application.

ZnS was first studied as a photocatalyst for the hydrogen evolution reaction (HER). Multiple internal phase-junctions (MIPs) were constructed on ZnS nanocrystals (NCs) using a simple solvothermal method. The photocatalytic HER rate ( $6.9 \text{ mmol g}^{-1} \text{ h}^{-1}$ ) was dramatically enhanced under simulated sunlight, up to  $\sim 70$  times than that of normal ZnS. This HER rate was further boosted up to  $19.8 \text{ mmol h}^{-1} \text{ g}^{-1}$  by loading 0.3 wt% Pt nanoparticles as co-catalyst, with ca. 2.87 times enhancement. The zinc atoms at these parallel interfaces of alternating wurtzite and sphalerite phases have different electronic environments. Moreover, in the electrocatalytic investigations, substantially lowered overpotential for

electrocatalytic HER is measured from the MIP-rich ZnS NCs, probably arising from the synergistic effect of easier proton adsorption and enhanced molecular H<sub>2</sub> desorption on the active sites. Introducing homojunctions on ZnS NCs has been demonstrated as an effective strategy for enhancing the performance in energy conversion applications. In future work, MIP-rich n-type ternary metal sulfide will be fabricated to investigate visible light response photocatalyst for HER, using cost-effective and non-toxic transition metal elements such as indium (In), tin (Sn) or bismuth (Bi).

Similar but different type of homo-interfaces were introduced to a p-type semiconductor nanomaterial, Cu<sub>x</sub>S (where  $1 \leq x \leq 2$ ) to understand the impact of MIP to p-type semiconductor photocatalyst for HER. The solvothermal synthesis of four Cu<sub>x</sub>S nanocrystals with different level of Cu deficiencies (CuS, Cu<sub>1.75</sub>S, Cu<sub>1.8</sub>S and Cu<sub>2</sub>S) was performed. By fine-tuning the synthetic parameters, MIPs were successfully introduced in Cu<sub>x</sub>S system with Cu<sub>1.8</sub>S as dominant phase. The most MIPs-rich Cu<sub>1.8</sub>S nanocrystal exhibited the enhanced photocatalytic HER rate of 0.38 mmol g<sup>-1</sup> h<sup>-1</sup> which is *ca.* 2.3 times higher than that of monophase Cu<sub>1.8</sub>S under simulated sunlight. This enhancement is probably related to the synergistic effect of easier proton adsorption and enhanced molecular H<sub>2</sub> desorption on the active sites. However, the phase transformation induced by strong electron beam irradiation in TEM hindered the observation on the interfaces at the phase-junctions. The Cu<sub>1.8</sub>S nanocrystals were further investigated by transition metal elements doping, and showed doping element-

dependant features and altered photocatalytic activity for HER. Compared with the monophasic  $\text{Cu}_{1.8}\text{S}$ , the doping effect was not significant with the MIPs-rich  $\text{Cu}_{1.8}\text{S}$  NCs in boosting the HER performance. Also, it is worthwhile to investigate other MIP-rich  $\text{Cu}_x\text{S}$  system in future work by constructing homojunctions between two or more kinds of  $\text{Cu}_x\text{S}$ , achieving higher HER rate by establishing an enhanced internal electric field.

In another approach, a Schottky junction was established between Au nanostructures and  $\text{Cu}_{1.8}\text{S}$  to form the hetero-interfaces. By this heterojunction, plasmon from Au nanomaterials can be used to boost up the photocatalytic activity to the nearby  $\text{Cu}_{1.8}\text{S}$ . This plasmonic-semiconductor model is established to study possible mechanisms including light/photon trapping, plasmon-induced resonance energy transfer (PIRET), and hot electron injection. The Au nanostructures with different plasmon modes, such as nanosphere, nanorod, and nanostar, were first embedded into  $\text{Cu}_2\text{O}$  nanocube as a precursor, followed by the controlled surface sulfurization that yielded Au- $\text{Cu}_{1.8}\text{S}$  yolk-shell heterostructure. In addition to the multiple interfaces between Au nanostar and  $\text{Cu}_{1.8}\text{S}$ , the unique hollow nanocage structure (thickness = *ca.* 3 nm) allows multiple reflections and scatterings of incident light within the interior voids, thus results in the much highly enhanced photocatalytic activity for HER. The Au- $\text{Cu}_{1.8}\text{S}$  hetero-nanostructure offers an understanding in the mechanism of plasmonic energy transfer from plasmonic metal to semiconductor. Further work will be made on investigating the chemical composition, micro/nanostructure,

and electronic structure of plasmonic metals (such as Cu, Al, Bi) and semiconductor materials. By designing well-performed plasmonic photocatalyst with metal-semiconductor heterojunctions, the efficiency of plasmonic energy transfer can be improved.

Further attempt has been done to optimize plasmonic metal–semiconductor heterojunctions by separating photogenerated charge. A heterostructure was fabricated by decorating smaller  $\text{Cu}_{1.8}\text{S}$  nanocages (size = *ca.* 22 nm) on Au nanorod (length = *ca.* 78 nm, width = *ca.* 35 nm) surface. With more interfacial contacts and multiple reflections and scattering of incident light within the interior voids of  $\text{Cu}_{1.8}\text{S}$  nanocages, significant enhancement on HER activity of the  $\text{Cu}_{1.8}\text{S}$  was achieved under simulated sunlight. The highlight of this unique heterostructure is twofold: the antenna effect of the Au nanorod on the  $\text{Cu}_{1.8}\text{S}$  nanocage that improves the transfer of plasmonic electrons for reduction reaction; with the enlarged contact area on the Au nanorod, the separation of photogenerated charge carriers is facilitated. However, coupling Au with  $\text{Cu}_{1.8}\text{S}$  semiconductor shows limited plasmonic enhancement for HER performance compared with theoretical performance. In the future, more effort will be devoted to exploring new metal sulfide semiconductor materials for heterojunction construction.

For plasmonic-semiconductor heterojunction photocatalyst, Au will be replaced by other cost-effective plasmonic metals such as Cu, Bi, Al to upscale the

production of plasmonic photocatalysts for commercial use. Cu nanomaterial exhibit a localized surface plasmon resonance (LSPR) band in the visible-light region ( $> 570$  nm); the SPR band of Cu nanomaterial can be adjusted to the near-infrared region by fabricating periodic nano-array patterns. Also, the development of the stable plasmonic copper-semiconductor nanostructure with stronger SPR bands will be explored, in an effort to broaden the photochemical application of this material.

There is much room to improve the catalytic efficiency of copper sulfides as a promising photochemical system although it is still far from the photochemical conversion threshold ( $>10\%$ ) for commercial use. To date, limited work has been taken on copper sulfides for photocatalytic  $H_2$  gas evolution from water, due to some drawbacks including fast recombination of charge carriers and low efficiency in photochemical conversion. These issues drive us to design the structure of copper sulfides through strategies such as multiple phase-junctions, and use of plasmonic energy of Au, aiming to promote catalytic reactions. The multiple phase-junctions approach (Chapter 4) can offer multiple channels for effective separation and transport of charge carriers, yielding some enhancement on  $H_2$  gas evolution. Further improvement by reducing recombination sites is still needed in order to promote the catalytic efficiency.

Besides, given the theoretical limit of plasmonic energy on solar energy conversion, plasmonic metal-copper sulfide photocatalytic system such as yolk-

shell (Chapter 5) and on-rod hetero-nanostructure (Chapter 6) are realized in an aim to study mechanism for plasmonic energy-related photocatalysis. The understanding in the presented plasmonic Au-copper sulfides photocatalytic system can pave a way for future work to improve catalytic efficiency.

To sum up, there are numerous opportunities to reach the theoretical maximum efficiency of photocatalysis by homo/heterojunctions-rich semiconductor materials. Future work will be put on the development of photocatalysts to boost up solar-to-hydrogen efficiency with the hope of reaching the need of practical use.

## References

- 1 C.F. Goodeve, J.A. Kitchener, *Transactions of the Faraday Society* **1938**, *34*, 570.
- 2 S. Kato, F. Mashio, *Abtr. Book Annu. Meet. Chemical Society of Japan* **1956**, 223.
- 3 A. Fujishima, K. Honda, *Nature* **1972**, *238*, 37.
- 4 J. Jia, L.C. Seitz, J.D. Benck, Y. Huo, Y. Chen, J.W.D. Ng, T. Bilir, J.S. Harris, T.F. Jaramillo, *Nature Communications* **2016**, *7*, 13237.
- 5 A. Heller, *Science* **1984**, *223*, 1141.
- 6 S.W. Boettcher, E.L. Warren, M.C. Putnam, E.A. Santori, D. Turner-Evans, M.D. Kelzenberg, M.G. Walter, J.R. McKone, B.S. Brunschwig, H.A. Atwater, N.S. Lewis, *Journal of the American Chemical Society* **2011**, *133*, 1216.
- 7 H. Liu, J. Yuan, W. Shangguan, *Energy & Fuels* **2006**, *20*, 2289.
- 8 K. Li, M. Han, R. Chen, S.-L. Li, S.-L. Xie, C. Mao, X. Bu, X.-L. Cao, L.-Z. Dong, P. Feng, Y.-Q. Lan, *Advanced Materials* **2016**, *28*, 8906.
- 9 S. Sun, W. Wang, D. Li, L. Zhang, D. Jiang, *ACS Catalysis* **2014**, *4*, 3498.
- 10 J. Su, L. Guo, N. Bao, C.A. Grimes, *Nano Letters* **2011**, *11*, 1928.
- 11 H. Kato, K. Asakura, A. Kudo, *Journal of the American Chemical Society* **2003**, *125*, 3082.
- 12 T. Ohno, L. Bai, T. Hisatomi, K. Maeda, K. Domen, *Journal of the American Chemical Society* **2012**, *134*, 8254.
- 13 Q. Jia, A. Iwase, A. Kudo, *Chemical Science* **2014**, *5*, 1513.

- 14 X. Wu, J. Zhao, L. Wang, M. Han, M. Zhang, H. Wang, H. Huang, Y. Liu, Z. Kang, *Applied Catalysis B: Environmental* **2017**, *206*, 501.
- 15 I. Tsuji, H. Kato, A. Kudo, *Chemistry of Materials* **2006**, *18*, 1969.
- 16 E. Ha, W. Liu, L. Wang, H.-W. Man, L. Hu, S.C.E. Tsang, C.T.-L. Chan, W.-M. Kwok, L.Y.S. Lee, K.-Y. Wong, *Scientific Reports* **2017**, *7*, 39411.
- 17 Q. Wang, T. Hisatomi, Q. Jia, H. Tokudome, M. Zhong, C. Wang, Z. Pan, T. Takata, M. Nakabayashi, N. Shibata, Y. Li, I.D. Sharp, A. Kudo, T. Yamada, K. Domen, *Nature Materials* **2016**, *15*, 611.
- 18 S. Chen, T. Takata, K. Domen, *Nature Reviews Materials* **2017**, *2*, 17050.
- 19 J. Li, N. Wu, *Catalysis Science & Technology* **2015**, *5*, 1360.
- 20 R.T. Shuey, *Semiconducting Ore Minerals*, Elsevier, Amsterdam 1975.
- 21 T. An, H. Zhao, P.K. Wong, *Advances in photocatalytic disinfection*, Berlin, Germany : Springer, Berlin, Germany 2017.
- 22 Y. Xu, M.A.A. Schoonen, *American Mineralogist* **2000**, *85*, 543.
- 23 Q. Xu, Y. Ma, J. Zhang, X. Wang, Z. Feng, C. Li, *Journal of Catalysis* **2011**, *278*, 329.
- 24 G. Liu, N. Hoivik, K. Wang, H. Jakobsen, *Solar Energy Materials and Solar Cells* **2012**, *105*, 53.
- 25 S.-D. Mo, W.Y. Ching, *Physical Review B* **1995**, *51*, 13023.
- 26 M.R. Hoffmann, S.T. Martin, W. Choi, D.W. Bahnemann, *Chemical Reviews* **1995**, *95*, 69.
- 27 L. Kavan, M. Grätzel, S.E. Gilbert, C. Klemenz, H.J. Scheel, *Journal of the American Chemical Society* **1996**, *118*, 6716.

- 28 T. Kawai, T. Sakata, *Nature* **1980**, 286, 474.
- 29 Q. Yuan, D. Liu, N. Zhang, W. Ye, H. Ju, L. Shi, R. Long, J. Zhu, Y. Xiong, *Angewandte Chemie* **2017**, 129, 4270.
- 30 M. Xu, M. Wang, T. Ye, N. Liang, L. Jin, J. Zai, X. Qian, *Chemistry – A European Journal* **2014**, 20, 13576.
- 31 K. Kobayakawa, A. Teranishi, T. Tsurumaki, Y. Sato, A. Fujishima, *Electrochimica Acta* **1992**, 37, 465.
- 32 M. Tabata, K. Maeda, T. Ishihara, T. Minegishi, T. Takata, K. Domen, *The Journal of Physical Chemistry C* **2010**, 114, 11215.
- 33 T.A. Kandiel, D.H. Anjum, K. Takanabe, *ChemSusChem* **2014**, 7, 3112.
- 34 E. Ha, L.Y.S. Lee, H.-W. Man, S.C.E. Tsang, K.-Y. Wong, *ACS Applied Materials & Interfaces* **2015**, 7, 9072.
- 35 E. Ha, L.Y.S. Lee, J. Wang, F. Li, K.-Y. Wong, S.C.E. Tsang, *Advanced Materials* **2014**, 26, 3496.
- 36 D. Pan, D. Weng, X. Wang, Q. Xiao, W. Chen, C. Xu, Z. Yang, Y. Lu, *Chemical Communications* **2009**, 4221.
- 37 Y.P. Xie, Z.B. Yu, G. Liu, X.L. Ma, H.-M. Cheng, *Energy & Environmental Science* **2014**, 7, 1895.
- 38 G. Mondal, M. Acharjya, A. Santra, P. Bera, S. Jana, N.C. Pramanik, A. Mondal, P. Bera, *New Journal of Chemistry* **2015**, 39, 9487.
- 39 X. Zhong, Y. Feng, W. Knoll, M. Han, *Journal of the American Chemical Society* **2003**, 125, 13559.

- 40 N. Kakuta, K.H. Park, M.F. Finlayson, A. Ueno, A.J. Bard, A. Campion, M.A. Fox, S.E. Webber, J.M. White, *The Journal of Physical Chemistry* **1985**, *89*, 732.
- 41 K. Zhang, D. Jing, C. Xing, L. Guo, *International Journal of Hydrogen Energy* **2007**, *32*, 4685.
- 42 I. Tsuji, H. Kato, H. Kobayashi, A. Kudo, *Journal of the American Chemical Society* **2004**, *126*, 13406.
- 43 I. Tsuji, H. Kato, H. Kobayashi, A. Kudo, *The Journal of Physical Chemistry B* **2005**, *109*, 7323.
- 44 I. Tsuji, H. Kato, A. Kudo, *Angewandte Chemie* **2005**, *117*, 3631.
- 45 S. Anderson, E.C. Constable, M.P. Dare-Edwards, J.B. Goodenough, A. Hamnett, K.R. Seddon, R.D. Wright, *Nature* **1979**, *280*, 571.
- 46 B. O'Regan, M. Grätzel, *Nature* **1991**, *353*, 737.
- 47 K. Maeda, M. Eguchi, W.J. Youngblood, T.E. Mallouk, *Chemistry of Materials* **2008**, *20*, 6770.
- 48 V.H. Houlding, M. Gratzel, *Journal of the American Chemical Society* **1983**, *105*, 5695.
- 49 K. Hirano, E. Suzuki, A. Ishikawa, T. Moroi, H. Shiroishi, M. Kaneko, *Journal of Photochemistry and Photobiology A: Chemistry* **2000**, *136*, 157.
- 50 Z. Jin, X. Zhang, G. Lu, S. Li, *Journal of Molecular Catalysis A: Chemical* **2006**, *259*, 275.
- 51 Q. Li, G. Lu, *Journal of Molecular Catalysis A: Chemical* **2007**, *266*, 75.

- 52 Y. Li, M. Guo, S. Peng, G. Lu, S. Li, *International Journal of Hydrogen Energy* **2009**, *34*, 5629.
- 53 Q. Li, L. Chen, G. Lu, *The Journal of Physical Chemistry C* **2007**, *111*, 11494.
- 54 X. Zhang, Z. Jin, Y. Li, S. Li, G. Lu, *Journal of Power Sources* **2007**, *166*, 74.
- 55 R. Sasikala, A. Shirole, V. Sudarsan, T. Sakuntala, C. Sudakar, R. Naik, S.R. Bharadwaj, *International Journal of Hydrogen Energy* **2009**, *34*, 3621.
- 56 Y. Liu, L. Guo, W. Yan, H. Liu, *Journal of Power Sources* **2006**, *159*, 1300.
- 57 X. Zhou, J. Wu, Q. Li, T. Zeng, Z. Ji, P. He, W. Pan, X. Qi, C. Wang, P. Liang, *Journal of Catalysis* **2017**, *355*, 26.
- 58 Q. Fengdong, L. Honghong, G. Rohiverth, J. Yutong, Y. Minghui, *Nanotechnology* **2016**, *27*, 385501.
- 59 T. de Boer, M.F. Bekheet, A. Gurlo, R. Riedel, A. Moewes, *Physical Review B* **2016**, *93*, 155205.
- 60 J. Lv, T. Kako, Z. Li, Z. Zou, J. Ye, *The Journal of Physical Chemistry C* **2010**, *114*, 6157.
- 61 Y. Ou, J. Lin, S. Fang, D. Liao, *Chemical Physics Letters* **2006**, *429*, 199.
- 62 J. Zhang, J. Yu, Y. Zhang, Q. Li, J.R. Gong, *Nano Letters* **2011**, *11*, 4774.
- 63 L.J. Zhang, T.F. Xie, D.J. Wang, S. Li, L.L. Wang, L.P. Chen, Y.C. Lu, *International Journal of Hydrogen Energy* **2013**, *38*, 11811.
- 64 D.V. Markovskaya, S.V. Cherepanova, A.A. Saraev, E.Y. Gerasimov, E.A. Kozlova, *Chemical Engineering Journal* **2015**, *262*, 146.

- 65 E. Hong, D. Kim, J.H. Kim, *Journal of Industrial and Engineering Chemistry* **2014**, *20*, 3869.
- 66 J. Zhang, W. Li, Y. Li, L. Zhong, C. Xu, *Applied Catalysis B: Environmental* **2017**, *217*, 30.
- 67 K.-i. Shimizu, H. Murayama, A. Nagai, A. Shimada, T. Hatamachi, T. Kodama, Y. Kitayama, *Applied Catalysis B: Environmental* **2005**, *55*, 141.
- 68 S. Liu, J.-H. Yang, J.-H. Choy, *Journal of Photochemistry and Photobiology A: Chemistry* **2006**, *179*, 75.
- 69 W. Shanguan, K. Inoue, *Chemical Communications* **1998**, 779.
- 70 H. Hata, Y. Kobayashi, V. Bojan, W.J. Youngblood, T.E. Mallouk, *Nano Letters* **2008**, *8*, 794.
- 71 R. Ma, Y. Kobayashi, W.J. Youngblood, T.E. Mallouk, *Journal of Materials Chemistry* **2008**, *18*, 5982.
- 72 J. Wu, S. Uchida, Y. Fujishiro, S. Yin, T. Sato, *Journal of Photochemistry and Photobiology A: Chemistry* **1999**, *128*, 129.
- 73 J. Wu, Y. Cheng, J. Lin, Y. Huang, M. Huang, S. Hao, *The Journal of Physical Chemistry C* **2007**, *111*, 3624.
- 74 D. Jing, L. Guo, *The Journal of Physical Chemistry C* **2007**, *111*, 13437.
- 75 Y. Miseki, K. Sayama, *Advanced Energy Materials* **2018**, *0*, 1801294.
- 76 Y. Wang, H. Suzuki, J. Xie, O. Tomita, D.J. Martin, M. Higashi, D. Kong, R. Abe, J. Tang, *Chemical Reviews* **2018**, *118*, 5201.
- 77 A. Iwase, Y.H. Ng, Y. Ishiguro, A. Kudo, R. Amal, *Journal of the American Chemical Society* **2011**, *133*, 11054.

- 78 E. Borgarello, J. Kiwi, M. Graetzel, E. Pelizzetti, M. Visca, *Journal of the American Chemical Society* **1982**, *104*, 2996.
- 79 S. Klosek, D. Raftery, *The Journal of Physical Chemistry B* **2001**, *105*, 2815.
- 80 Y. Cao, W. Yang, W. Zhang, G. Liu, P. Yue, *New Journal of Chemistry* **2004**, *28*, 218.
- 81 D. Jing, Y. Zhang, L. Guo, *Chemical Physics Letters* **2005**, *415*, 74.
- 82 L.G. Devi, S.G. Kumar, B.N. Murthy, N. Kottam, *Catalysis Communications* **2009**, *10*, 794.
- 83 V. Štengl, S. Bakardjieva, N. Murafa, *Materials Chemistry and Physics* **2009**, *114*, 217.
- 84 W. Mu, J.-M. Herrmann, P. Pichat, *Catalysis Letters* **1989**, *3*, 73.
- 85 H. Khan, D. Berk, *Applied Catalysis A: General* **2015**, *505*, 285.
- 86 J.C. Yu, W. Ho, J. Yu, H. Yip, P.K. Wong, J. Zhao, *Environmental Science & Technology* **2005**, *39*, 1175.
- 87 C. Xu, Y.A. Shaban, W.B. Ingler, S.U.M. Khan, *Solar Energy Materials and Solar Cells* **2007**, *91*, 938.
- 88 X. Li, N. Kikugawa, J. Ye, *Advanced Materials* **2008**, *20*, 3816.
- 89 Y. Huang, W. Ho, Z. Ai, X. Song, L. Zhang, S. Lee, *Applied Catalysis B: Environmental* **2009**, *89*, 398.
- 90 A. Zaleska, E. Grabowska, J.W. Sobczak, M. Gazda, J. Hupka, *Applied Catalysis B: Environmental* **2009**, *89*, 469.

- 91 R. Asahi, T. Morikawa, T. Ohwaki, K. Aoki, Y. Taga, *Science* **2001**, 293, 269.
- 92 X. Chen, C. Burda, *Journal of the American Chemical Society* **2008**, 130, 5018.
- 93 M. Batzill, E.H. Morales, U. Diebold, *Physical Review Letters* **2006**, 96, 026103.
- 94 S.L. Suib, *New and Future Developments in Catalysis: Catalysis by Nanoparticles*, Elsevier Science, 2013.
- 95 K. Lv, H. Zuo, J. Sun, K. Deng, S. Liu, X. Li, D. Wang, *Journal of Hazardous Materials* **2009**, 161, 396.
- 96 Z. He, X. Xu, S. Song, L. Xie, J. Tu, J. Chen, B. Yan, *The Journal of Physical Chemistry C* **2008**, 112, 16431.
- 97 Y. Gai, J. Li, S.-S. Li, J.-B. Xia, S.-H. Wei, *Physical Review Letters* **2009**, 102, 036402.
- 98 Y. Wang, Y. Wang, Y. Meng, H. Ding, Y. Shan, X. Zhao, X. Tang, *The Journal of Physical Chemistry C* **2008**, 112, 6620.
- 99 I. Tsuji, A. Kudo, *Journal of Photochemistry and Photobiology A: Chemistry* **2003**, 156, 249.
- 100 Z. Lei, G. Ma, M. Liu, W. You, H. Yan, G. Wu, T. Takata, M. Hara, K. Domen, C. Li, *Journal of Catalysis* **2006**, 237, 322.
- 101 J. Yang, D. Wang, H. Han, C. Li, *Accounts of Chemical Research* **2013**, 46, 1900.

- 102 G.L. Chiarello, E. Selli, L. Forni, *Applied Catalysis B: Environmental* **2008**, *84*, 332.
- 103 T. Sreethawong, S. Yoshikawa, *Catalysis Communications* **2005**, *6*, 661.
- 104 W. Lu, S. Gao, J. Wang, *The Journal of Physical Chemistry C* **2008**, *112*, 16792.
- 105 A. Iwase, H. Kato, A. Kudo, *Catalysis Letters* **2006**, *108*, 7.
- 106 M. Hara, J. Nunoshige, T. Takata, J.N. Kondo, K. Domen, *Chemical Communications* **2003**, 3000.
- 107 G. Wu, T. Chen, G. Zhou, X. Zong, C. Li, *Science in China Series B: Chemistry* **2008**, *51*, 97.
- 108 K. Gurunathan, *International Journal of Hydrogen Energy* **2004**, *29*, 933.
- 109 M. Liu, W. You, Z. Lei, G. Zhou, J. Yang, G. Wu, G. Ma, G. Luan, T. Takata, M. Hara, K. Domen, C. Li, *Chemical Communications* **2004**, 2192.
- 110 T.K. Townsend, N.D. Browning, F.E. Osterloh, *Energy & Environmental Science* **2012**, *5*, 9543.
- 111 Y. Takahara, J.N. Kondo, T. Takata, D. Lu, K. Domen, *Chemistry of Materials* **2001**, *13*, 1194.
- 112 Y.-H. Pai, S.-Y. Fang, *Journal of Power Sources* **2013**, *230*, 321.
- 113 K. Akihiko, N. Seira, K. Hideki, *Chemistry Letters* **1999**, *28*, 1197.
- 114 J. Sato, N. Saito, Y. Yamada, K. Maeda, T. Takata, J.N. Kondo, M. Hara, H. Kobayashi, K. Domen, Y. Inoue, *Journal of the American Chemical Society* **2005**, *127*, 4150.

- 115 K. Maeda, N. Saito, D. Lu, Y. Inoue, K. Domen, *The Journal of Physical Chemistry C* **2007**, *111*, 4749.
- 116 K. Maeda, X. Wang, Y. Nishihara, D. Lu, M. Antonietti, K. Domen, *The Journal of Physical Chemistry C* **2009**, *113*, 4940.
- 117 D. Duonghong, E. Borgarello, M. Graetzel, *Journal of the American Chemical Society* **1981**, *103*, 4685.
- 118 B. Cao, G. Li, H. Li, *Applied Catalysis B: Environmental* **2016**, *194*, 42.
- 119 K. Teramura, K. Maeda, T. Saito, T. Takata, N. Saito, Y. Inoue, K. Domen, *The Journal of Physical Chemistry B* **2005**, *109*, 21915.
- 120 X. Zong, H. Yan, G. Wu, G. Ma, F. Wen, L. Wang, C. Li, *Journal of the American Chemical Society* **2008**, *130*, 7176.
- 121 F.A. Frame, F.E. Osterloh, *The Journal of Physical Chemistry C* **2010**, *114*, 10628.
- 122 J. Yang, H. Yan, X. Wang, F. Wen, Z. Wang, D. Fan, J. Shi, C. Li, *Journal of Catalysis* **2012**, *290*, 151.
- 123 Y. Shi, B. Zhang, *Chemical Society Reviews* **2016**, *45*, 1529.
- 124 J.F. Callejas, J.M. McEnaney, C.G. Read, J.C. Crompton, A.J. Biacchi, E.J. Popczun, T.R. Gordon, N.S. Lewis, R.E. Schaak, *ACS Nano* **2014**, *8*, 11101.
- 125 S. Cao, Y. Chen, C.-C. Hou, X.-J. Lv, W.-F. Fu, *Journal of Materials Chemistry A* **2015**, *3*, 6096.
- 126 T. Wu, S. Chen, D. Zhang, J. Hou, *Journal of Materials Chemistry A* **2015**, *3*, 10360.
- 127 X. Chen, L. Liu, P.Y. Yu, S.S. Mao, *Science* **2011**, *331*, 746.

- 128 X. Wang, Q. Xu, M. Li, S. Shen, X. Wang, Y. Wang, Z. Feng, J. Shi, H. Han, C. Li, *Angewandte Chemie* **2012**, *124*, 13266.
- 129 W. Liu, E. Ha, L. Wang, L. Hu, L.Y.S. Lee, K.-Y. Wong, *Advanced Materials Interfaces* **2018**, *5*, 1800611.
- 130 A. Boltasseva, H.A. Atwater, *Science* **2011**, *331*, 290.
- 131 R. Jiang, B. Li, C. Fang, J. Wang, *Advanced Materials* **2014**, *26*, 5274.
- 132 S. Link, M.A. El-Sayed, *The Journal of Physical Chemistry B* **1999**, *103*, 4212.
- 133 V. Giannini, A.I. Fernández-Domínguez, S.C. Heck, S.A. Maier, *Chemical Reviews* **2011**, *111*, 3888.
- 134 N.J. Halas, S. Lal, W.-S. Chang, S. Link, P. Nordlander, *Chemical Reviews* **2011**, *111*, 3913.
- 135 T.K. Sau, A.L. Rogach, F. Jäckel, T.A. Klar, J. Feldmann, *Advanced Materials* **2010**, *22*, 1805.
- 136 Z.W. Seh, S. Liu, M. Low, S.-Y. Zhang, Z. Liu, A. Mlayah, M.-Y. Han, *Advanced Materials* **2012**, *24*, 2310.
- 137 J. Li, S.K. Cushing, F. Meng, T.R. Senty, A.D. Bristow, N. Wu, *Nature Photonics* **2015**, *9*, 601.
- 138 N. Wu, *Nanoscale* **2018**, *10*, 2679.
- 139 S.K. Cushing, J. Li, J. Bright, B.T. Yost, P. Zheng, A.D. Bristow, N. Wu, *The Journal of Physical Chemistry C* **2015**, *119*, 16239.
- 140 J. Zhang, Y. Wang, J. Zhang, Z. Lin, F. Huang, J. Yu, *ACS Applied Materials & Interfaces* **2013**, *5*, 1031.

- 141 T. Baran, S. Wojtyła, A. Dibenedetto, M. Aresta, W. Macyk, *Applied Catalysis B: Environmental* **2015**, *178*, 170.
- 142 X. Meng, Q. Yu, G. Liu, L. Shi, G. Zhao, H. Liu, P. Li, K. Chang, T. Kako, J. Ye, *Nano Energy* **2017**, *34*, 524.
- 143 B. Liu, X. Hu, X. Li, Y. Li, C. Chen, K.-h. Lam, *Scientific Reports* **2017**, *7*, 16396.
- 144 A. Kudo, M. Sekizawa, *Catalysis Letters* **1999**, *58*, 241.
- 145 A. Kudo, M. Sekizawa, *Chemical Communications* **2000**, 1371.
- 146 G. Wang, B. Huang, Z. Li, Z. Lou, Z. Wang, Y. Dai, M.-H. Whangbo, *Scientific Reports* **2015**, *5*, 8544.
- 147 S.R. Chalana, V. Ganesan, V.P.M. Pillai, *AIP Advances* **2015**, *5*, 107207.
- 148 Y. Hong, J. Zhang, F. Huang, J. Zhang, X. Wang, Z. Wu, Z. Lin, J. Yu, *Journal of Materials Chemistry A* **2015**, *3*, 13913.
- 149 J. Zhang, J. Yu, Y. Zhang, Q. Li, J.R. Gong, *Nano Letters* **2011**, *11*, 4774.
- 150 X. Wang, Q. Xu, M. Li, S. Shen, X. Wang, Y. Wang, Z. Feng, J. Shi, H. Han, C. Li, *Angewandte Chemie International Edition* **2012**, *51*, 13089.
- 151 Z. Fang, S. Weng, X. Ye, W. Feng, Z. Zheng, M. Lu, S. Lin, X. Fu, P. Liu, *ACS Applied Materials & Interfaces* **2015**, *7*, 13915.
- 152 M. Liu, D. Jing, Z. Zhou, L. Guo, *Nature Communications* **2013**, *4*, 2278.
- 153 T.-T. Zhuang, Y. Liu, Y. Li, Y. Zhao, L. Wu, J. Jiang, S.-H. Yu, *Angewandte Chemie* **2016**, *128*, 6506.
- 154 R.E. Algra, M.A. Verheijen, M.T. Borgstrom, L.-F. Feiner, G. Immink, W.J.P. van Enckevort, E. Vlieg, E.P.A.M. Bakkers, *Nature* **2008**, *456*, 369.

- 155 K. Pemasiri, M. Montazeri, R. Gass, L.M. Smith, H.E. Jackson, J. Yarrison-Rice, S. Paiman, Q. Gao, H.H. Tan, C. Jagadish, X. Zhang, J. Zou, *Nano Letters* **2009**, *9*, 648.
- 156 M. Liu, Y. Chen, J. Su, J. Shi, X. Wang, L. Guo, *Nature Energy* **2016**, *1*, 16151.
- 157 W.E. Spicer, I. Lindau, P. Skeath, C.Y. Su, P. Chye, *Physical Review Letters* **1980**, *44*, 420.
- 158 C.R.M. Grovenor, *Journal of Physics C: Solid State Physics* **1985**, *18*, 4079.
- 159 S.-H. Yu, M. Yoshimura, *Advanced Materials* **2002**, *14*, 296.
- 160 X. Ouyang, T.-Y. Tsai, D.-H. Chen, Q.-J. Huang, W.-H. Cheng, A. Clearfield, *Chemical Communications* **2003**, 886.
- 161 W. Feng, Z. Fang, B. Wang, L. Zhang, Y. Zhang, Y. Yang, M. Huang, S. Weng, P. Liu, *Journal of Materials Chemistry A* **2017**, *5*, 1387.
- 162 Z.-X. Deng, C. Wang, X.-M. Sun, Y.-D. Li, *Inorganic Chemistry* **2002**, *41*, 869.
- 163 M. Uehara, Y. Nakamura, S. Sasaki, H. Nakamura, H. Maeda, *CrystEngComm* **2011**, *13*, 5998.
- 164 Z. Wu, X. Sun, H. Xu, H. Konishi, Y. Wang, Y. Lu, K. Cao, C. Wang, H. Zhou, *Ore Geology Reviews* **2018**, *92*, 318.
- 165 X. Wang, J. Shi, Z. Feng, M. Li, C. Li, *Physical Chemistry Chemical Physics* **2011**, *13*, 4715.
- 166 Z. Wang, L.L. Daemen, Y. Zhao, C.S. Zha, R.T. Downs, X. Wang, Z.L. Wang, R.J. Hemley, *Nature Materials* **2005**, *4*, 922.

- 167 Y. Cuizhuo, L. Yanguo, S. Hongyu, G. Defeng, L. Xiaohong, L. Wei, L. Baoting, Z. Xiangyi, *Nanotechnology* **2008**, *19*, 095704.
- 168 X. Wu, K. Li, H. Wang, *Journal of Alloys and Compounds* **2009**, *487*, 537.
- 169 D.J. Chadi, *Physical Review Letters* **1979**, *43*, 43.
- 170 G.-T. Zhou, X. Wang, J.C. Yu, *Crystal Growth & Design* **2005**, *5*, 1761.
- 171 F. Huang, J.F. Banfield, *Journal of the American Chemical Society* **2005**, *127*, 4523.
- 172 S.A. Acharya, N. Maheshwari, L. Tatikondewar, A. Kshirsagar, S.K. Kulkarni, *Crystal Growth & Design* **2013**, *13*, 1369.
- 173 O. Brafman, S.S. Mitra, *Physical Review* **1968**, *171*, 931.
- 174 Y.C. Cheng, C.Q. Jin, F. Gao, X.L. Wu, W. Zhong, S.H. Li, P.K. Chu, *Journal of Applied Physics* **2009**, *106*, 123505.
- 175 H.-B. Kim, D.-J. Jang, *Nanoscale* **2016**, *8*, 403.
- 176 W. Vogel, P.H. Borse, N. Deshmukh, S.K. Kulkarni, *Langmuir* **2000**, *16*, 2032.
- 177 A. Malakar, B. Das, S. Islam, C. Meneghini, G. De Giudici, M. Merlini, Y.V. Kolen'ko, A. Iadecola, G. Aquilanti, S. Acharya, S. Ray, *Scientific Reports* **2016**, *6*, 26031.
- 178 X. Yang, H. Xue, J. Xu, X. Huang, J. Zhang, Y.B. Tang, T.W. Ng, H.L. Kwong, X.M. Meng, C.S. Lee, *ACS Appl Mater Interfaces* **2014**, *6*, 9078.
- 179 F.A. La Porta, J. Andres, M.S. Li, J.R. Sambrano, J.A. Varela, E. Longo, *Physical Chemistry Chemical Physics* **2014**, *16*, 20127.

- 180 H. Yaghoubi, Z. Li, Y. Chen, H.T. Ngo, V.R. Bhethanabotla, B. Joseph, S. Ma, R. Schlaf, A. Takshi, *ACS Catalysis* **2015**, *5*, 327.
- 181 X. Chen, S. Shen, L. Guo, S.S. Mao, *Chemical Reviews* **2010**, *110*, 6503.
- 182 M. Liu, L. Wang, G. Lu, X. Yao, L. Guo, *Energy & Environmental Science* **2011**, *4*, 1372.
- 183 P.T. Landsberg, M.S. Abrahams, *Journal of Applied Physics* **1984**, *55*, 4284.
- 184 Y. Hou, A.B. Laursen, J. Zhang, G. Zhang, Y. Zhu, X. Wang, S. Dahl, I. Chorkendorff, *Angewandte Chemie International Edition* **2013**, *52*, 3621.
- 185 S. Liu, Z. Zhang, J. Bao, Y. Lan, W. Tu, M. Han, Z. Dai, *The Journal of Physical Chemistry C* **2013**, *117*, 15164.
- 186 D.R. Cummins, U. Martinez, A. Sherehiy, R. Koppera, A. Martinez-Garcia, R.K. Schulze, J. Jasinski, J. Zhang, R.K. Gupta, J. Lou, M. Chhowalla, G. Sumanasekera, A.D. Mohite, M.K. Sunkara, G. Gupta, *Nature Communications* **2016**, *7*, 11857.
- 187 E. Skulason, G.S. Karlberg, J. Rossmeisl, T. Bligaard, J. Greeley, H. Jonsson, J.K. Nørskov, *Physical Chemistry Chemical Physics* **2007**, *9*, 3241.
- 188 K.J. Vetter, *Electrochemical Kinetics: Theoretical and Experimental Aspects*, Academic Press, New York 1967.
- 189 L. Lu, Y. Shen, X. Chen, L. Qian, K. Lu, *Science* **2004**, *304*, 422.
- 190 B.E. Conway, B.V. Tilak, *Electrochimica Acta* **2002**, *47*, 3571.

- 191 D.J. Chakrabarti, D.E. Laughlin, *Bulletin of Alloy Phase Diagrams* **1983**, 4, 254.
- 192 C. Coughlan, M. Ibáñez, O. Dobrozhan, A. Singh, A. Cabot, K.M. Ryan, *Chemical Reviews* **2017**, 117, 5865.
- 193 L. Isac, A. Duta, A. Kriza, S. Manolache, M. Nanu, *Thin Solid Films* **2007**, 515, 5755.
- 194 P. Roy, S.K. Srivastava, *CrystEngComm* **2015**, 17, 7801.
- 195 A. Morales-García, A.L. Soares, E.C. Dos Santos, H.A. de Abreu, H.A. Duarte, *The Journal of Physical Chemistry A* **2014**, 118, 5823.
- 196 Q. Xu, B. Huang, Y. Zhao, Y. Yan, R. Noufi, S.-H. Wei, *Applied Physics Letters* **2012**, 100, 061906.
- 197 Q. Tian, F. Jiang, R. Zou, Q. Liu, Z. Chen, M. Zhu, S. Yang, J. Wang, J. Wang, J. Hu, *ACS Nano* **2011**, 5, 9761.
- 198 Y. Wu, C. Wadia, W. Ma, B. Sadler, A.P. Alivisatos, *Nano Letters* **2008**, 8, 2551.
- 199 W. Jiang, F. Wu, Y. Jiang, M. Sun, K. Zhang, Y. Xia, D. Wang, A. Xie, *Nanoscale* **2017**, 9, 10961.
- 200 Y. Chen, C. Davoisne, J.-M. Tarascon, C. Guéry, *Journal of Materials Chemistry* **2012**, 22, 5295.
- 201 C.-H. Lai, K.-W. Huang, J.-H. Cheng, C.-Y. Lee, B.-J. Hwang, L.-J. Chen, *Journal of Materials Chemistry* **2010**, 20, 6638.

- 202 Y. Chen, S. Zhao, X. Wang, Q. Peng, R. Lin, Y. Wang, R. Shen, X. Cao, L. Zhang, G. Zhou, J. Li, A. Xia, Y. Li, *Journal of the American Chemical Society* **2016**, *138*, 4286.
- 203 M. Wang, A. Tang, D. Zhu, C. Yang, F. Teng, *CrystEngComm* **2015**, *17*, 6598.
- 204 C.B. Murray, D.J. Norris, M.G. Bawendi, *Journal of the American Chemical Society* **1993**, *115*, 8706.
- 205 S. Gorai, D. Ganguli, S. Chaudhuri, *Crystal Growth & Design* **2005**, *5*, 875.
- 206 H.M.A. Hassan, V. Abdelsayed, A.E.R.S. Khder, K.M. AbouZeid, J. Turner, M.S. El-Shall, S.I. Al-Resayes, A.A. El-Azhary, *Journal of Materials Chemistry* **2009**, *19*, 3832.
- 207 D. Jia, L. Cao, D. Wang, X. Guo, H. Liang, F. Zhao, Y. Gu, D. Wang, *Chemical Communications* **2014**, *50*, 11488.
- 208 Y. Li, H. Liao, Y. Ding, Y. Fan, Y. Zhang, Y. Qian, *Inorganic Chemistry* **1999**, *38*, 1382.
- 209 M. Xiao, Z. Wang, M. Lyu, B. Luo, S. Wang, G. Liu, H.-M. Cheng, L. Wang, *Advanced Materials* **2018**, *0*, 1801369.
- 210 P. Lukashev, W.R.L. Lambrecht, T. Kotani, M. van Schilfgaarde, *Physical Review B* **2007**, *76*, 195202.
- 211 Y. Zhao, H. Pan, Y. Lou, X. Qiu, J. Zhu, C. Burda, *Journal of the American Chemical Society* **2009**, *131*, 4253.
- 212 L. Wang, W. Wang, S. Sun, *Journal of Materials Chemistry* **2012**, *22*, 6553.

- 213 I.B. Rufus, V. Ramakrishnan, B. Viswanathan, J.C. Kuriacose, *Langmuir* **1990**, *6*, 565.
- 214 K. Chang, W. Chen, *ACS Nano* **2011**, *5*, 4720.
- 215 E. Hirahara, *J. Phys. Soc. Jpn.* **1951**, *6*, 422.
- 216 J. Tao, J. Chen, J. Li, L. Mathurin, J.-C. Zheng, Y. Li, D. Lu, Y. Cao, L. Wu, R.J. Cava, Y. Zhu, *Proceedings of the National Academy of Sciences* **2017**, *114*, 9832.
- 217 L. Sun, L. Xiang, X. Zhao, C.-J. Jia, J. Yang, Z. Jin, X. Cheng, W. Fan, *ACS Catalysis* **2015**, *5*, 3540.
- 218 H. Van Swygenhoven, P.M. Derlet, A.G. Frøseth, *Nature Materials* **2004**, *3*, 399.
- 219 M.I.B. Utama, M. de la Mata, C. Magen, J. Arbiol, Q. Xiong, *Advanced Functional Materials* **2013**, *23*, 1636.
- 220 M. de la Mata, C. Magén, P. Caroff, J. Arbiol, *Nano Letters* **2014**, *14*, 6614.
- 221 J. Hou, C. Yang, Z. Wang, W. Zhou, S. Jiao, H. Zhu, *Applied Catalysis B: Environmental* **2013**, *142-143*, 504.
- 222 P. Kar, S. Farsinezhad, X. Zhang, K. Shankar, *Nanoscale* **2014**, *6*, 14305.
- 223 Y.-Y. Hsu, N.-T. Suen, C.-C. Chang, S.-F. Hung, C.-L. Chen, T.-S. Chan, C.-L. Dong, C.-C. Chan, S.-Y. Chen, H.M. Chen, *ACS Applied Materials & Interfaces* **2015**, *7*, 22558.
- 224 J. Zhang, Q. Xu, Z. Feng, M. Li, C. Li, *Angewandte Chemie* **2008**, *120*, 1790.

- 225 J. Song, H. Zhao, R. Sun, X. Li, D. Sun, *Energy & Environmental Science* **2017**, *10*, 225.
- 226 B. Li, T. Gu, T. Ming, J. Wang, P. Wang, J. Wang, J.C. Yu, *ACS Nano* **2014**, *8*, 8152.
- 227 S. Chang, Q. Li, X. Xiao, K.Y. Wong, T. Chen, *Energy & Environmental Science* **2012**, *5*, 9444.
- 228 S. Linic, P. Christopher, D.B. Ingram, *Nature Materials* **2011**, *10*, 911.
- 229 S. Xiao, P. Liu, W. Zhu, G. Li, D. Zhang, H. Li, *Nano Letters* **2015**, *15*, 4853.
- 230 Y. Choi, H.-i. Kim, G.-h. Moon, S. Jo, W. Choi, *ACS Catalysis* **2016**, *6*, 821.
- 231 S. Kumar, K. Ojha, A.K. Ganguli, *Advanced Materials Interfaces* **2017**, *4*, 1600981.
- 232 X. Ma, K. Zhao, H. Tang, Y. Chen, C. Lu, W. Liu, Y. Gao, H. Zhao, Z. Tang, *Small* **2014**, *10*, 4664.
- 233 X. Yu, A. Shavel, X. An, Z. Luo, M. Ibáñez, A. Cabot, *Journal of the American Chemical Society* **2014**, *136*, 9236.
- 234 Y.J. Lee, J.B. Joo, Y. Yin, F. Zaera, *ACS Energy Letters* **2016**, *1*, 52.
- 235 S.-U. Lee, H. Jung, D.H. Wi, J.W. Hong, J. Sung, S.-I. Choi, S.W. Han, *Journal of Materials Chemistry A* **2018**, *6*, 4068.
- 236 J. Feng, J. Liu, X. Cheng, J. Liu, M. Xu, J. Zhang, *Advanced Science* **2018**, *5*, 1700376.

- 237 R. Shi, Y. Cao, Y. Bao, Y. Zhao, G.I.N. Waterhouse, Z. Fang, L.-Z. Wu, C.-H. Tung, Y. Yin, T. Zhang, *Advanced Materials* **2017**, *29*, 1700803.
- 238 J. Liu, S.Z. Qiao, J.S. Chen, X.W. Lou, X. Xing, G.Q. Lu, *Chemical Communications* **2011**, *47*, 12578.
- 239 X. Shi, Z. Lou, P. Zhang, M. Fujitsuka, T. Majima, *ACS Applied Materials & Interfaces* **2016**, *8*, 31738.
- 240 A. Cuevas, R. Romero, D. Leinen, E.A. Dalchiele, J.R. Ramos-Barrado, F. Martin, *Solar Energy Materials and Solar Cells* **2015**, *134*, 199.
- 241 T. Teranishi, M. Sakamoto, *The Journal of Physical Chemistry Letters* **2013**, *4*, 2867.
- 242 X. Liu, M.T. Swihart, *Chemical Society Reviews* **2014**, *43*, 3908.
- 243 P.V. Quintana-Ramirez, M.C. Arenas-Arrocena, J. Santos-Cruz, M. Vega-González, O. Martínez-Alvarez, V.M. Castaño-Meneses, L.S. Acosta-Torres, J. de la Fuente-Hernández, *Beilstein Journal of Nanotechnology* **2014**, *5*, 1542.
- 244 Y. Chang, Y. Cheng, Y. Feng, H. Jian, L. Wang, X. Ma, X. Li, H. Zhang, *Nano Letters* **2018**, *18*, 886.
- 245 S. Link, M.B. Mohamed, M.A. El-Sayed, *The Journal of Physical Chemistry B* **1999**, *103*, 3073.
- 246 S. Tanwar, K.K. Haldar, T. Sen, *Journal of the American Chemical Society* **2017**, *139*, 17639.
- 247 Y.-C. Yang, H.-J. Wang, J. Whang, J.-S. Huang, L.-M. Lyu, P.-H. Lin, S. Gwo, M.H. Huang, *Nanoscale* **2014**, *6*, 4316.

- 248 L. Zhang, D.A. Blom, H. Wang, *Chemistry of Materials* **2011**, *23*, 4587.
- 249 K.M. Mayer, J.H. Hafner, *Chemical Reviews* **2011**, *111*, 3828.
- 250 K. Aslan, M. Wu, J.R. Lakowicz, C.D. Geddes, *Journal of the American Chemical Society* **2007**, *129*, 1524.
- 251 Y. Lu, Y. Yin, Z.-Y. Li, Y. Xia, *Nano Letters* **2002**, *2*, 785.
- 252 S. Zhang, R. Jiang, Y. Guo, B. Yang, X.-L. Chen, J. Wang, Y. Zhao, *Small* **2016**, *12*, 4264.
- 253 L. Zhang, H. Wang, *ACS Nano* **2011**, *5*, 3257.
- 254 P. Roy, K. Mondal, S.K. Srivastava, *Crystal Growth & Design* **2008**, *8*, 1530.
- 255 S.L. Smitha, D. Philip, K.G. Gopchandran, *Spectrochimica Acta Part A: Molecular and Biomolecular Spectroscopy* **2009**, *74*, 735.
- 256 C.S. Kim, S.H. Choi, J.H. Bang, *ACS Applied Materials & Interfaces* **2014**, *6*, 22078.
- 257 X. Ding, C.H. Liow, M. Zhang, R. Huang, C. Li, H. Shen, M. Liu, Y. Zou, N. Gao, Z. Zhang, Y. Li, Q. Wang, S. Li, J. Jiang, *Journal of the American Chemical Society* **2014**, *136*, 15684.
- 258 J. Cui, Y. Li, L. Liu, L. Chen, J. Xu, J. Ma, G. Fang, E. Zhu, H. Wu, L. Zhao, L. Wang, Y. Huang, *Nano Letters* **2015**, *15*, 6295.
- 259 X. Yu, J. Bi, G. Yang, H. Tao, S. Yang, *The Journal of Physical Chemistry C* **2016**, *120*, 24533.
- 260 Y. Tian, T. Tatsuma, *Journal of the American Chemical Society* **2005**, *127*, 7632.

- 261 S.K. Cushing, J. Li, F. Meng, T.R. Senty, S. Suri, M. Zhi, M. Li, A.D. Bristow, N. Wu, *Journal of the American Chemical Society* **2012**, *134*, 15033.
- 262 W. Hou, S.B. Cronin, *Advanced Functional Materials* **2013**, *23*, 1612.
- 263 H. Sun, Q. He, S. Zeng, P. She, X. Zhang, J. Li, Z. Liu, *New Journal of Chemistry* **2017**, *41*, 7244.
- 264 S. Linic, U. Aslam, C. Boerigter, M. Morabito, *Nature Materials* **2015**, *14*, 567.
- 265 U. Aslam, S. Chavez, S. Linic, *Nature Nanotechnology* **2017**, *12*, 1000.
- 266 P. Christopher, H. Xin, A. Marimuthu, S. Linic, *Nature Materials* **2012**, *11*, 1044.
- 267 M.J. Kale, T. Avanesian, H. Xin, J. Yan, P. Christopher, *Nano Letters* **2014**, *14*, 5405.
- 268 S. Link, C. Burda, M.B. Mohamed, B. Nikoobakht, M.A. El-Sayed, *Physical Review B* **2000**, *61*, 6086.
- 269 K. Wu, J. Chen, J.R. McBride, T. Lian, *Science* **2015**, *349*, 632.
- 270 L. Wang, J. Ge, A. Wang, M. Deng, X. Wang, S. Bai, R. Li, J. Jiang, Q. Zhang, Y. Luo, Y. Xiong, *Angewandte Chemie* **2014**, *126*, 5207.
- 271 Y. Pan, S. Deng, L. Polavarapu, N. Gao, P. Yuan, C.H. Sow, Q.-H. Xu, *Langmuir* **2012**, *28*, 12304.
- 272 X. Yu, F. Liu, J. Bi, B. Wang, S. Yang, *Nano Energy* **2017**, *33*, 469.
- 273 J.W. Hong, D.H. Wi, S.-U. Lee, S.W. Han, *Journal of the American Chemical Society* **2016**, *138*, 15766.

- 274 B. Wu, D. Liu, S. Mubeen, T.T. Chuong, M. Moskovits, G.D. Stucky, *Journal of the American Chemical Society* **2016**, *138*, 1114.
- 275 A.F. Wells, *Structural inorganic chemistry*, Oxford : Clarendon Press, Oxford 1975.
- 276 J.M. Luther, P.K. Jain, T. Ewers, A.P. Alivisatos, *Nature Materials* **2011**, *10*, 361.
- 277 R. Bardhan, N.K. Grady, T. Ali, N.J. Halas, *ACS Nano* **2010**, *4*, 6169.
- 278 C.Y. Toe, Z. Zheng, H. Wu, J. Scott, R. Amal, Y.H. Ng, *The Journal of Physical Chemistry C* **2018**, *122*, 14072.
- 279 X.-C. Ma, Y. Dai, L. Yu, B.-B. Huang, *Light: Science & Applications* **2016**, *5*, e16017.
- 280 Y. Zhang, S. He, W. Guo, Y. Hu, J. Huang, J.R. Mulcahy, W.D. Wei, *Chemical Reviews* **2018**, *118*, 2927.
- 281 B.K. Patra, A. Shit, A.K. Guria, S. Sarkar, G. Prusty, N. Pradhan, *Chemistry of Materials* **2015**, *27*, 650.
- 282 S.M. Kim, D. Park, Y. Yuk, S.H. Kim, J.Y. Park, *Faraday Discussions* **2013**, *162*, 355.
- 283 X. Liu, C. Lee, W.-C. Law, D. Zhu, M. Liu, M. Jeon, J. Kim, P.N. Prasad, C. Kim, M.T. Swihart, *Nano Letters* **2013**, *13*, 4333.
- 284 X. Zhang, Y.L. Chen, R.-S. Liu, D.P. Tsai, *Reports on Progress in Physics* **2013**, *76*, 046401.
- 285 J. Cui, R. Jiang, W. Lu, S. Xu, L. Wang, *Small* **2017**, *13*, 1602235.

286 N. Gogurla, A.K. Sinha, S. Santra, S. Manna, S.K. Ray, *Scientific Reports*  
**2014**, 4, 6483.